Investigation of Factors Affecting the Hydraulic Conductivity of a Fractured Sandstone

A Thesis

Submitted to the College of Graduate Studies and Research

In Partial Fulfillment of the Requirements

for the

Degree of Master of Science

in the

Department of Civil and Geological Engineering

University of Saskatchewan

Saskatoon

by

Jarret D. Thomson

PERMISSION TO USE

The author has agreed that the library, University of Saskatchewan, may make this thesis freely available for inspection. Moreover, the author has agreed that permission for extensive copying of this thesis for scholarly purposes may be granted by the professors who supervised the thesis work recorded herein or, in their absence, by the head of the Department or the Dean of the College in which the thesis work was done. It is understood that due recognition will be given to the author of thesis and to the University of Saskatchewan in any use of the material in this thesis. Copying or publication or any other use of the thesis for financial gain without approval by the University of Saskatchewan and the author's written permission is prohibited.

Requests for permission to copy or to make any other use of material in this thesis is whole or part should be addressed to:

Head of Department of Civil and Geological Engineering

University of Saskatchewan

Engineering Building

57 Campus Drive

Saskatoon, Saskatchewan

Canada S7N 5A9

ABSTRACT

An understanding of groundwater flow is essential in many aspects of mining. This is especially true for the sandstones of the Manitou Falls Formation, which overlie uranium deposits in the Athabasca Basin of northern Saskatchewan. Experience has shown that the hydraulic conductivities of these sandstones can be relatively high, especially in zones containing natural fractures, thus leading to potentially problematic groundwater inflow rates. This thesis presents the results of a study of hydraulic conductivity of the Manitou Falls Formation, in which detailed core logging and laboratory testing were undertaken for samples from two boreholes at the McArthur River mine site. Results from the logging and laboratory testing were interpreted in context provided by multiple packer tests conducted in these boreholes. Through core logging, indicators of conductive zones were identified. These indicators include fracture orientation (sub-vertical fractures were found to have more of an impact on conductivity than horizontal fractures), infilling, and staining. The laboratory testing program involved the measurement of hydraulic conductivities of fractured core samples across a span of effective confining pressures representative of in-situ conditions. Changes in fracture aperture were simultaneously recorded at each confining pressure level. It was found that theoretical relationships between aperture change and fracture conductivity represent the observed behavior of the samples reasonably well when fracture roughness is accounted for. The laboratory testing also confirmed the effects of fracture staining and infilling on hydraulic conductivity inferred from core logging and packer testing results.

The results provide insights into the mechanisms underlying flow in fractured intervals of the Manitou Falls Formation, and provide guidance for selecting intervals to investigate during future packer testing in this formation.

ACKNOWLEDGMENTS

First and foremost I'd like to thank Chris Hawkes for his hard work and patience with this thesis; and Doug Milne, and Rashid Bashir for their guidance in establishing my project.

I would like to thank my father, Gordon Thomson. He'll forever be in our hearts. Without him I wouldn't have found my way into this field and so many other things. My sister Carol, for the support, proofreading and formatting help. My mom, Marge Thomson, who has always been there for me, I wouldn't be the person I am today without her.

Finally I'd like to thank my wife Brenna, for all of the encouragement to get me through the slow progressing times.

TABLE OF CONTENTS

LIST OF FIGURES

LIST OF TABLES

LIST OF SYMBOLS

A = cross sectional area

a_h = hydraulic aperture

a_m = mechanical aperture

fc = fracture count

i = hydraulic head gradient

JCS = Joint Compressive Stress

JRC = Joint Roughness Coefficient

K = hydraulic conductivity

K = hydraulic conductivity

K_{eq} = equivalent hydraulic conductivity from lab testing

$K_{eq\text{-}field}$ = equivalent hydraulic conductivity of a rock mass at the field scale

L = Length

n = porosity

P_c' = effective confining pressure

q = darcian velocity

Q = flow rate

r_a = micro roughness

r_h = hydraulic radius (commonly denoted as b in fracture flow)

RMR = Rock Mass Rating

RQD = Rock Quality Designation

S = fracture spacing

TRC = Total Core Recovery

V = seepage velocity

w = Width

α^o = Angle of friction

ϕ_r = Residual Friction Angle

μ = kinematic viscosity

v = dynamic viscosity

σ_{no} = Normal Stress

CHAPTER 1 INTRODUCTION

1.1 BACKGROUND

The Athabasca basin is located in northern Saskatchewan, Canada (Figure 1.1). It is currently a major source of the world's uranium. The uranium deposits are found at or below an unconformity where sandstones of the Manitou Falls Formation are underlain by crystalline basement rocks. The Manitou Falls Formation is extensive across the Athabasca Basin, and is a hydrogeologically complex set of units that offers many challenges during mine development such as shaft sinking. Predicting and mitigating groundwater inflow is a major priority during the process of shaft sinking through the sandstone. The research presented in this thesis was undertaken to explore the author's hypothesis that general trends in hydraulic conductivity in the Manitou Falls Formation can be obtained from core logging; more specifically, that focusing core logging efforts on natural fractures and indicators of flow can help to identify zones where more detailed analyses such as packer testing should be undertaken in order to characterize inflow potential.

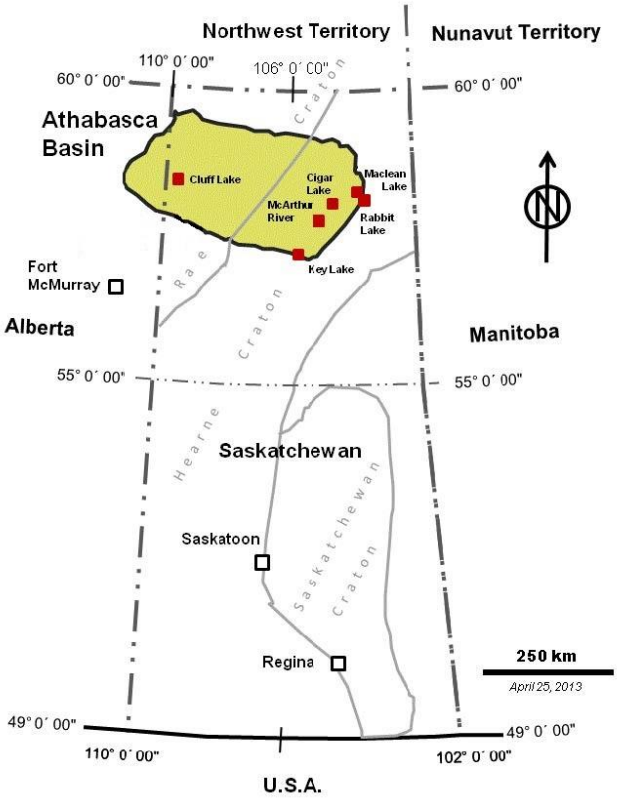

Figure 1.1 - Map of the Athabasca Basin (after Aldrin Resources, 2014)

1.2 OBJECTIVES

The primary goal of this research was to assess the hydraulic conductivity of the sandstones of the Manitou Falls Formation. Given that this sandstone was thought to be fracture dominated, secondary objectives were to assess the relative contributions of matrix and fractures to flow, and to characterize the fracture network using core from shaft pilot holes, interpreted in the context provided by packer testing.

1.3 SCOPE

The scope of this research includes two main components: field data investigation, and lab testing of core samples. In the field data investigation, the objective was to use previously conducted packer testing information and compare it to core logging results (some previously conducted by consultants, and some – for selected intervals – logged in greater detail by the author of this thesis). This was conducted on two shaft pilot holes from the McArthur River Mine site: MC-316 and SP-002. The lab testing was undertaken to assess samples for hydraulic conductivity while mimicking in-situ conditions as closely as possible. This provided the opportunity to explore the relationships between stress, hydraulic conductivity, fracture aperture, and other fracture attributes.

The study area for this research comprises the Athabasca Basin in northern Saskatchewan, Canada. More specifically, this research focused on the hydraulic properties of Manitou Falls Formation, using data obtained from Cameco Corporation's McArthur River Mine site.

1.4 STRUCTURE

The main body of this thesis is divided into four sections; literature review, field work, lab testing, and a discussion which focuses on the effects of scale of investigation on hydraulic conductivity.

Chapter 2 (literature review) introduces the background and theory that will be discussed throughout this thesis.

Chapter 3 (field work) presents data from two shaft pilot holes and analyses the relationships between core logging observations and hydraulic conductivities measured through packer testing.

Chapter 4 (lab testing) presents the methodologies and results for lab testing that was conducted on core samples from one of the pilot holes; tests that were designed based on the analysis of field data in Chapter 3.

Results from Chapters 3 and 4 are related to practical applications in Chapter 5. The effect of scale for different types of testing are compared to assess the effectiveness and practicality of core logging, packer testing and lab testing. The relationship between stress (hence depth) and hydraulic conductivity are also investigated.

CHAPTER 2 LITERATURE REVIEW

2.1 GEOLOGICAL SETTING OF THE STUDY AREA

The Manitou Falls Formation is a sandstone-dominated stratigraphic unit that encompasses or overlies the majority of all known Uranium deposits in the Athabasca Basin. There is a major unconformity below the Manitou Falls Formation, with underlying basement rocks that are crystalline (Ramaekers et al., 2001). The age of the basin is poorly understood. Based on the weathering of the crystalline rocks, the sandstone is thought to be much younger than the 1.75 Ga age of the metamorphic rocks it is derived from.(Yeo et al., 2002). Figure 2.1 displays a simplified cross section of geology of the Athabasca Basin with some features that lead to uranium mineralization. The McArthur River deposit is depicted in the centre of the figure. The Manitou Falls Formation (MF) can be further subdivided into four members. The thicknesses of these layers vary from site to site, and may be truncated depending on their location in the Athabasca Basin.

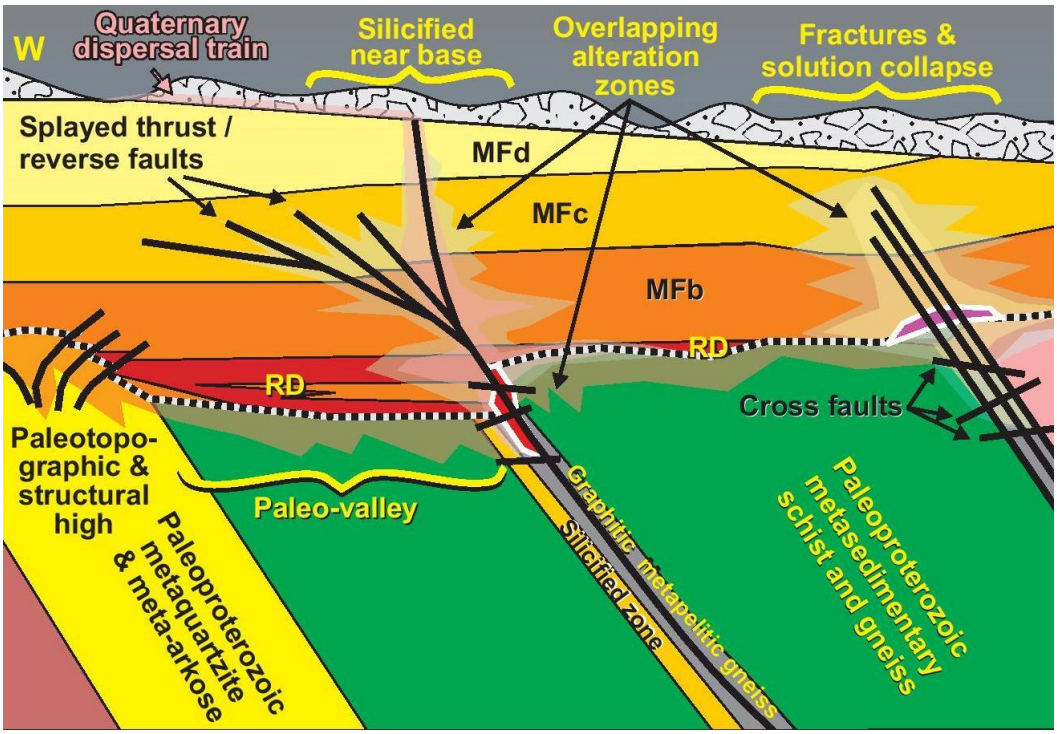

Figure 2.1 - Geology of uranium deposits. MFa is not shown here, but it is present beneath MFb is some regions (after Jefferson et al, 2007)

The MFa member is the oldest and most variable member in the Manitou Falls Formation. It can be identified by interbedded sandstone and conglomerate with the presence of 2% or greater clast-supported conglomerates (Ramaekers, 1990). The MFb member is thought to have originated in a humid climate; with deposition occurring as an alluvial braid plain characterized by broad channels (Jefferson et al., 2003). It predominantly consists of sandstone between two conglomerate-bearing intervals (Ramaekers, 1990). The MFc member can be characterized by a conglomerate-free medium to very coarse-grained sandstone (Ramaekers, 1990). Thin granular layers are common with a thickness of less than 2 cm. The MFd member appears to be very similar to the MFc member (Ramaekers, 1990; Jefferson et al., 2003). All of the MF members contain interstitial clay which is rich at the base and thins upward (Yeo et al., 2002).

2.2 SHAFT SINKING HISTORY IN THE STUDY AREA

As of 2015, Cameco Corporation (Cameco) had sunk five shafts in the Athabasca Basin. The high hydraulic conductivity and recharge rates present a challenging environment for shaft sinking. Traditionally, cover grouting has been used to minimise inflow potential. Cover grouting is a step-wise process by which grout is injected into boreholes fanning out radially from the shaft at selected depth intervals during shaft sinking, in order to create a grout curtain that surrounds the shaft along its full length. Four probe holes are initially drilled in each quadrant to assess the inflow potential. If the probe holes indicate high flow potential, a grout cover is then constructed. The four holes are utilized in the grout cover with another 12 holes added to complete a 16 hole grout curtain. Figure 2.2 shows a hole producing a flow of approximately 50 m^3/hr. The potential for large inflows from probe holes can create a risk of flooding. Two probe holes in the sinking of Shaft 3 at McArthur River encountered inflows of approximately 125 m^3/hr, causing substantial delays (Beattie, 2007). Ground freezing may be utilized in upcoming projects to mitigate the risks associated with the installation of a grout curtain. A detailed understanding of the distribution of hydraulic conductivity is essential to planning any mining activities in an environment like the Athabasca Basin.

Figure 2.2 - Flow from a grout cover hole, Shaft #2 at McArthur River (Beattie, 2007)

Substantial data sets are collected during exploration and preparation for shafts. Core logging, packer testing, and down hole geophysics are the primary sources of information. The process of sinking a shaft also yields many useful observations that can aid in synthesizing the borehole data. These observations are a starting point for further research on key factors that control flow potential through a rock mass.

Packer testing is used to measure the bulk hydraulic conductivity of selected intervals which are isolated by inflating packers in the borehole. A pressure (head) perturbation is induced in the rock mass by injecting or removing water. The response of the hydraulic pressure is recorded and in turn used to calculate the hydraulic conductivity.

The Manitou Falls Formation has proven to be the source of all major inflows encountered during the sinking of shafts in the Athabasca Basin (Golder Associates, 2002). Packer testing conducted by Golder Associates (1998) shows the hydraulic conductivity of the Manitou Falls formation is, on average, an order of magnitude higher than that of the basement rocks.

Based on a report by Golder Associates (1999), there are three main fracture sets that have been encountered in the exploration holes in the Manitou Falls Formation. The fracture sets appear to be consistent in all holes from site to site. The main fracture set coincides with the horizontal bedding planes. Spacing of the bedding planes range from several centimetres to several meters. The second and third fracture sets are vertical to sub-vertical and are perpendicular to one another. The sub vertical fracture sets are thought to be the largest contributors to hydraulic conductivity (Golder Associates, 2002). Grouting records during shaft sinking have indicated that fractures generally become tighter and less continuous with depth.

The conditions of all fractures in the study area vary considerably. The majority of surfaces are fresh with little infilling; however, in some areas significant infilling is present (Golder Associates, 2002). Golder Associates' core logs have noted that there is limonite staining present on a portion of the fractures observed. Limonite is a term generally used in the Athabasca basin for any iron oxide-hydroxide which cannot be defined compositionally or mineralogically. The oxidization is yellowish brown when loose or can be found as a blackish stain when more intact (Mahoney, 2009). Limonization is thought to be associated with meteoric waters, and can be useful in identifying large structures that may extend near surface. Limonization can alter all aspects of the sandstone to the point where previous minerals and fabric may not be identifiable. Due to limonization being associated with migrating waters, the greatest degree of alteration occurs in fractures.

Golder Associates (1998) suggest that groundwater inflow occurred upward via sub-vertical fractures through the shaft floor during shaft sinking, rather than through horizontal fractures seen in shaft walls. This was later supported in a report by Golder Associates (2002). During the sinking of shaft number one at Cigar Lake, sub-vertical fractures ranged from five to eight meters apart, and could be seen for several tens of meters on the shaft walls. The majority of the flow into the shaft was through these sub-vertical fractures. Flow was also observed through horizontal fractures; however, they typically appeared to be in connection with sub-vertical fractures.

2.3 DISCONTINUITIES IN A ROCK MASS

Multiple types of discontinuities can exist in a rock mass, including fractures, Joints, faults, cracks, fissures, bedding planes, and shear zones. Each type of discontinuity has unique origins and characteristics. Faults and shears are failure surfaces that have experienced lateral movement, and are generally differentiated based on the scale of movement (i.e., large-scale faults; small-scale shears). Joints occur through changes in stresses in the rock and results in failure surfaces that have separated, often in sub-parallel sets, with no lateral offset between opposing faces (Lee and Farmer, 1993). Fissures are cracks that are small in aperture and of limited length. To accurately deduce what type of discontinuity is present, a large amount of information needs to be collected. In many cases it is not feasible to collect this information. The majority of the discontinuities described in this thesis are joints. The common term used for the study of flow through rock mass discontinuities is fracture flow. For this reason all discontinues are referred to as fractures for this thesis.

Fractures are usually the primary conduits for fluid and control fluid flow through the majority of rock masses. The bulk hydraulic conductivity of a rock mass therefore is primarily dependent on these fractures. Flow in fractured media is a complex process that is dependent on a wide range of characteristics. Brown outlines these characteristics in 1981 ISRM report (Brown); *Suggested Methods for Quantitative*

Description of Discontinuities in Rock Masses. Selected parameters from the report that pertain to rock mass flow are described below

- **Orientation**: describes a fracture's orientation in 3-dimensional space. Generally reported using the strike and dip, or dip and dip direction, of the fracture.
- **Spacing**: the measure of the perpendicular distance measured from one fracture to the next. For practical purposes an average is most often given to represent an interval of fractures.
- **Persistence**: the length of the fracture that can be seen day-lighting on exposed surfaces (e.g., shaft walls). It indicates a lower bound for the fracture length. Very little information on persistence can be derived from diamond drilling, so it will not be used much in this research.
- **Roughness**: the surface roughness and waviness relative to the mean plane of the fracture. Roughness contributes to head loss during fluid flow within a fracture, and influences shear strength.
- **Aperture**: the perpendicular distance between fracture surfaces. It can be expressed as the distance from the mean of asperities on one side of the fracture to the other.
- **Filling**: material in a fracture that separates the wall rock. Filling materials may include sand, silt, clay, and gouge. Healed fractures occur when minerals grow within the fracture and fill the fracture void; the most common materials are quartz and calcite. Staining in the form of mineral coating such as limonite on wall surfaces is also a form of infilling.
- **Number of sets**: The number of fracture sets that make up the fracture network.
- **Contact area**: the contact area between opposing faces of a fracture reduces flow by limiting flow paths.

It is difficult to characterize the majority of these parameters because they cannot be directly measured; most can only be estimated empirically or analytically (Lee and Farmer, 1993). A further difficulty is the fact that these parameters can be quite variable within a given study area.

2.3.1 *Fracture Characterization and Orientation Bias Effects*

Characteristics of natural fractures can be obtained from fracture traces that daylight on mapped surfaces or are intersected by diamond drill cores. Mapped faces offer the most complete picture of rockmass fractures , though it must be noted that mapping on an exposed face results in a bias towards the fracture set(s) that are oriented normal to the face. This bias should be taken into consideration when calculating fracture spacing and length. Diamond drilling is the most direct way to map subsurface rock without mining through it. Through core analysis, an understanding of fracture orientations and conditions can be obtained. However, diamond drill cores have a similar bias towards fracture set(s) normal to the core axis. Further, fracture lengths cannot accurately be determined due to the small diameter of the core. Fractures along the core axis seldom appear in the core, even if they are closely spaced.

2.3.2 *Fracture Roughness*

Fracture roughness is a challenging parameter to define and measure. The difficulty in determining roughness mainly occurs in the question of scale. Micro roughness refers to small scale roughness, which is traditionally measured as the largest amplitude over a given interval. Louis (1969) defines it as height from the lowest valley to the highest peak in a given interval length. Figures 2.3 and 2.4 are examples of roughness measurement by Louis (1969). The first is over a scale of several millimetres and the second is over a scale of tens of microns. It is up to the individual conducting measurement to determine the proper scale of measurement.

Larger-scale roughness, over tens of centimetres, may be better suited as a measure of tortuosity. Both the name and definition of larger-scale roughness varies; some examples are macro roughness (Louis, 1969), waviness (Goodman, 1973), and angularity (Sharp, 1970). A considerable amount of ambiguity exists in literature as to what is the ideal scale to measure small scale and large-scale roughness. Roughness

can measured as the total amplitude or the change in angle of the fracture surface (from one location to the next), or a combination of the two.

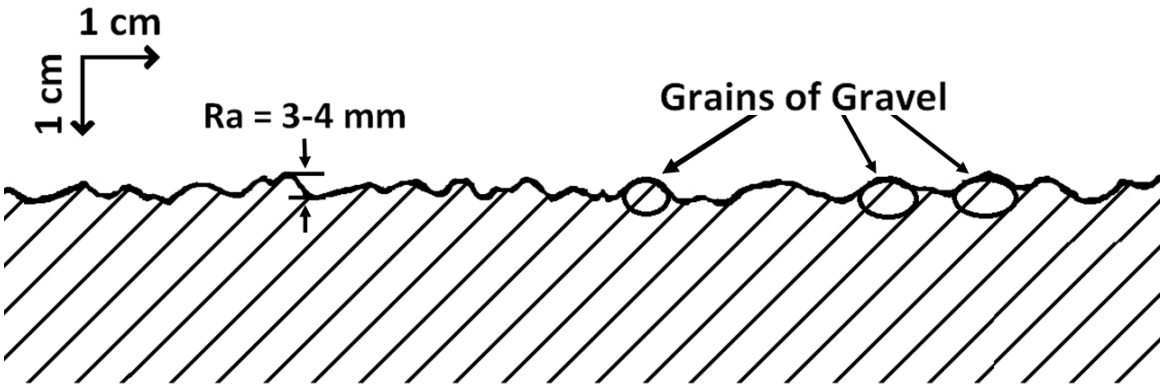

Figure 2.3 - Measurement of roughness on the scale of several millimeters (after Louis, 1969)

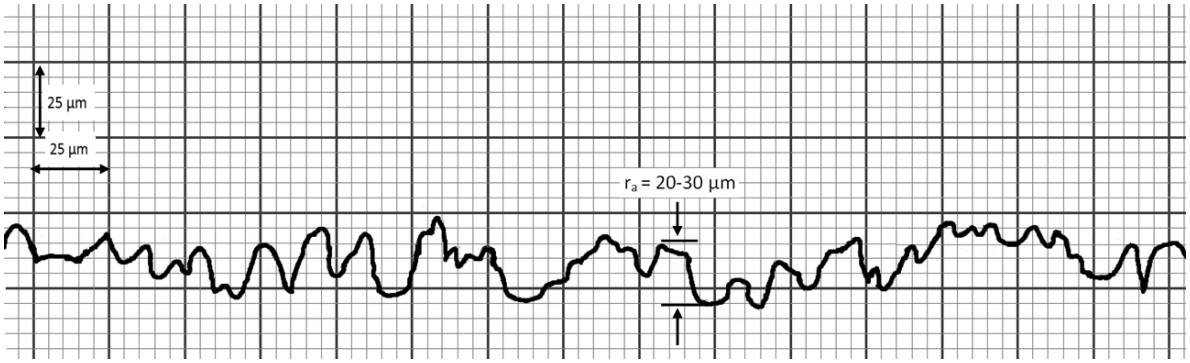

Figure 2.4 - Measurement of micro roughness k on the scale of tens of microns (after Louis, 1969)

The Joint Roughness Coefficient, also known as JRC, was developed by Barton and Choubey (1977). The system has a rating that is based on a series of 10 cm long fracture traces, rated from 0 (least rough) to 20 (most rough). The 10 traces that comprise the scale are shown in Figure 2.5. Three methods are given to assess the JRC value. The first is by drawing traces of a joint surface and then visually comparing them to the standard traces in Figure 2.5. An advantage of this method is that the traces take

into account the height of the asperities, their regularity and directional trend (Lee and Farmer, 1993). It is a simple and quantitative assessment that can be obtained in the field with limited effort. However, this method of visually determining JRC induces a degree of subjectivity. A second measurement method, which avoids this subjectivity, involves a tilt test of a fracture sample. The sample is tilted until the fracture slides. The angle at which movement occurs can be used to calculate JRC using the following equation:

$$JRC = \frac{\alpha^o - \phi_r}{\log(\frac{JCS}{\sigma_{no}})} \quad [2.1]$$

Where α^o is the angle at which the sample slides in degrees, ϕ_r is the residual fraction angle in degrees, JCS is the joint compressive strength in MPa, and σ_{no} is the normal stress which is assumed to be 0.001MPa for a slide test. Since the calculation requires residual friction angle and joint compressive strength, it is impractical for most applications. Using the third method, developed by Barton and Bandis (1982), the maximum amplitude of a joint over a given length is measured to compute JRC using the following equation:

$$JRC = 400\frac{a}{L} \quad [2.2]$$

Where *a* is the maximum amplitude of the profile and *L* is the length of the profile. Figure 2.6 shows a profile with an example of amplitude measurement.

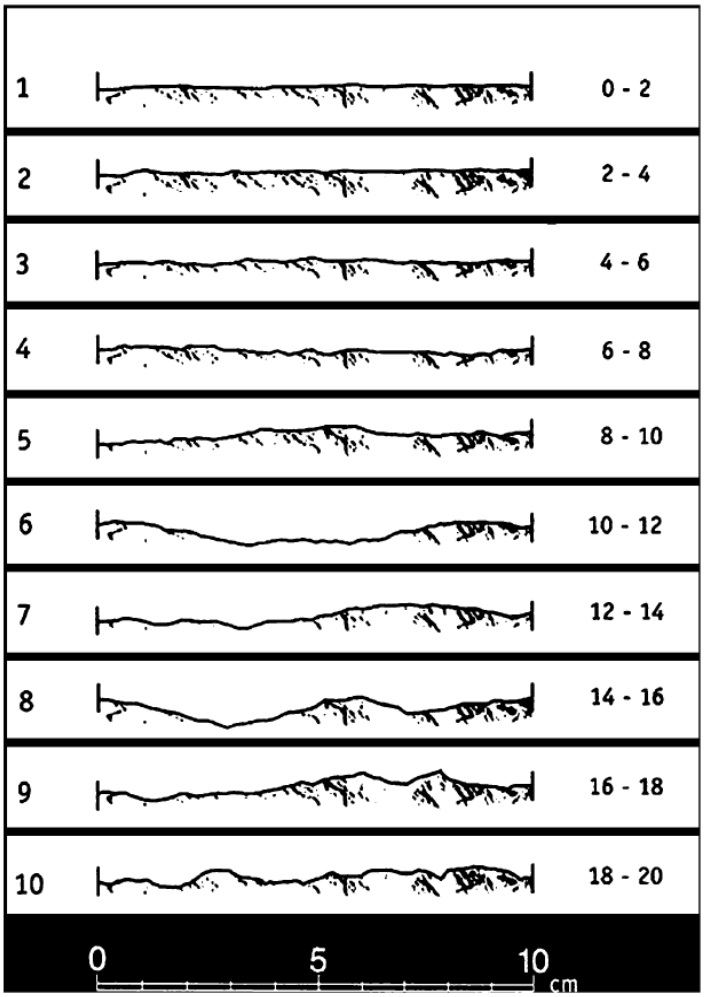

Figure 2.5 - JRC roughness profiles (Barton and Choubey, 1977)

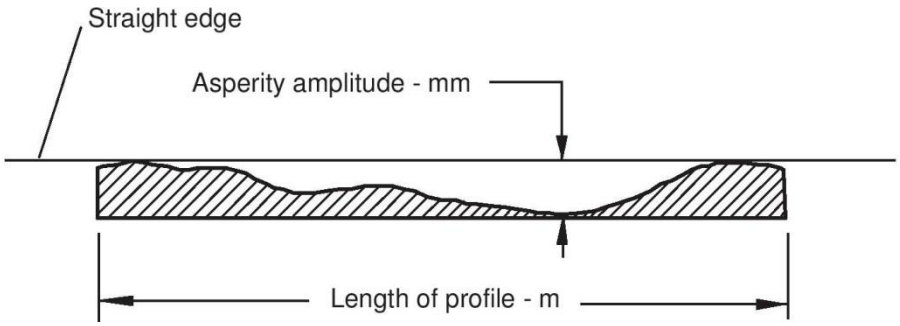

Figure 2.6 - Measuring JRC using the amplitude and a straight edge (Barton and Bandis, 1982)

Fracture surface traces can be digitized using a Laser Roughness Profilometer (LPR), and the digital dataset used to calculate various roughness parameters. For example, JRC can be calculated using equation 2.2. A portable LPR was designed and built at the University of Saskatchewan by Milne et al. (2009). The LRP scans and records joint surface coordinates along a 15 cm profile.

2.3.3 *Fracture Aperture*

Fracture aperture (or fracture width) refers to the distance separating two fracture faces. Aperture can be quite variable over the extent of a fracture, and is challenging to characterize in practical engineering problems. The physical distance between two fracture faces is termed mechanical aperture, a_m. Six classes of mechanical aperture are shown in Table 2.1. True aperture, or mechanical aperture a_m, is rarely used for groundwater engineering. Hydraulic aperture, a_h, is a measurable equivalent aperture based on hydraulic properties. In fracture flow analysis, hydraulic aperture, a_h, is commonly used. This describes the effective aperture of the flow path through the fracture. To visualise fracture flow, the analogy of two flat planes with flow occurring in the space between them is often used (Snow, 1969). However in reality fractures are not flat, smooth, or continuous. Micro roughness adds resistance, apertures are erratic, and the planes are undulating.

Measurement of fracture aperture under in-situ conditions generally cannot be done. It is commonly measured as seen in a day lighting fracture, but there is no way of easily measuring properties of a closed aperture in-situ.

Table 2.1 – Classification of mechanical aperture sizes (Lee and Farmer, 1993)

Mechanical Aperture (mm)	**Class**
<0.1	Very tight
0.10 - 0.25	Tight
0.25 – 0.50	Partially open
0.50 – 2.50	Open
2.50 – 10.0	Moderately wide
<10	Wide

Many methods have been attempted to determine the mechanical aperture of a fracture. Hakami and Larson (1996) injected a florescent resin into a fracture. The fracture was pressurized while the resin set in order to mimic in-situ conditions. Thin sections of the fracture were taken and imaged to obtain aperture measurements.

Sophisticated imaging techniques can be used such as an ultrasound (Jensen et al., 2005), x-ray (Johns et al., 1993), or synchrotron x-ray microtomography (Robb et al., 2007) to get highly detailed images of fractures. These fracture images can be analysed to estimate mechanical aperture. Sharp et al. (2014) utilized high resolution X-ray tomography with promising results. No methods have been developed to efficiently and economically obtain mechanical aperture. Correlations of mechanical aperture to hydraulic aperture have been successfully used as a practical method of obtaining mechanical aperture.

The relationship between mechanical and hydraulic apertures has been investigated by several researchers. Voegele (1981) combined the results on one graph, which is shown in Figure 2.7. Barton (1985) Combined JRC with the data to compile a relationship between aperture and JRC. This relationship can be used to determine a mechanical aperture value from a calculated hydraulic aperture. Figure 2.8 displays this relationship. The following is the relationship developed by Barton

$$a_h = \frac{JRC^{2.5}}{\left({}^{a_m}/_{a_h}\right)^2} (\mu m) \qquad [2.3]$$

Where a_h represents hydraulic (smooth-walled) fracture aperture in µm.

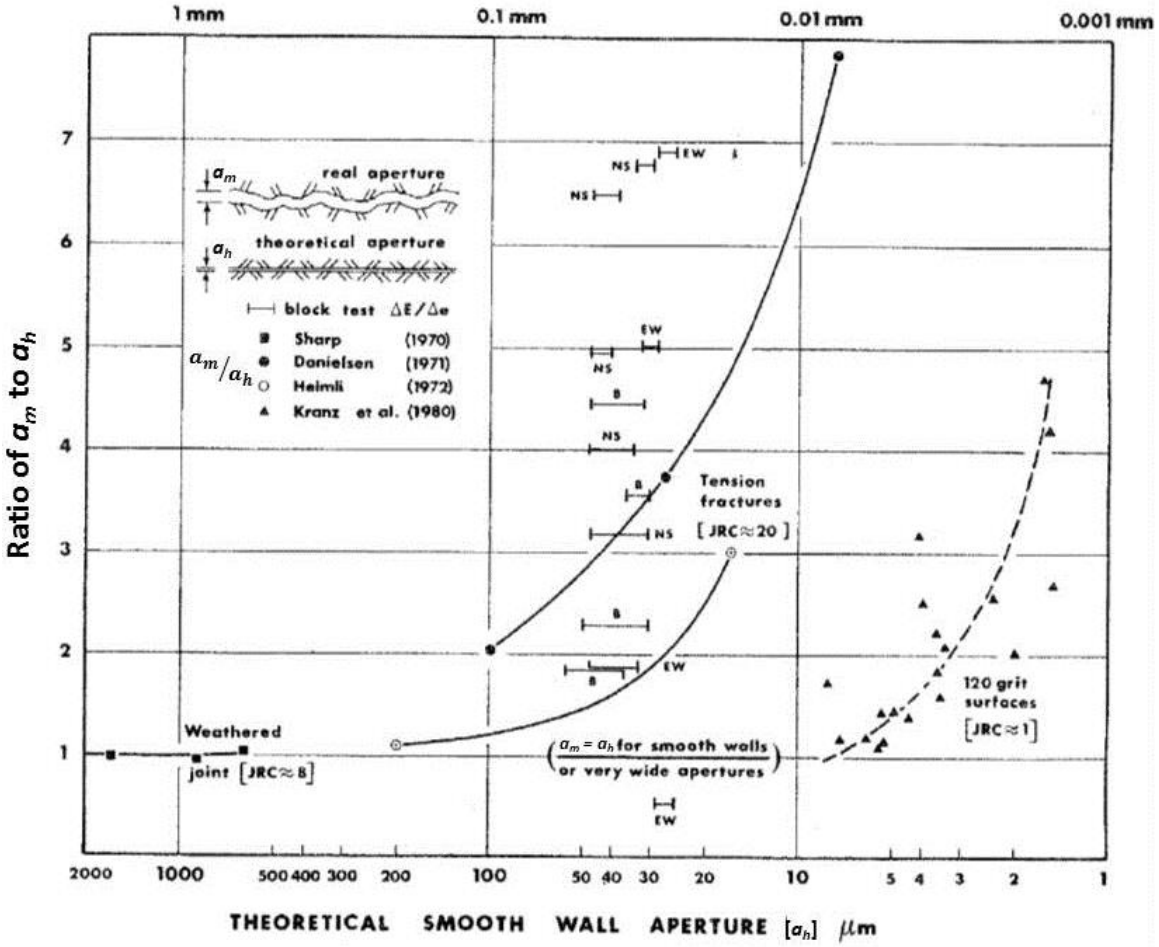

Figure 2.7 - Relationship of hydraulic and mechanical aperture (after Voegele, 1981)

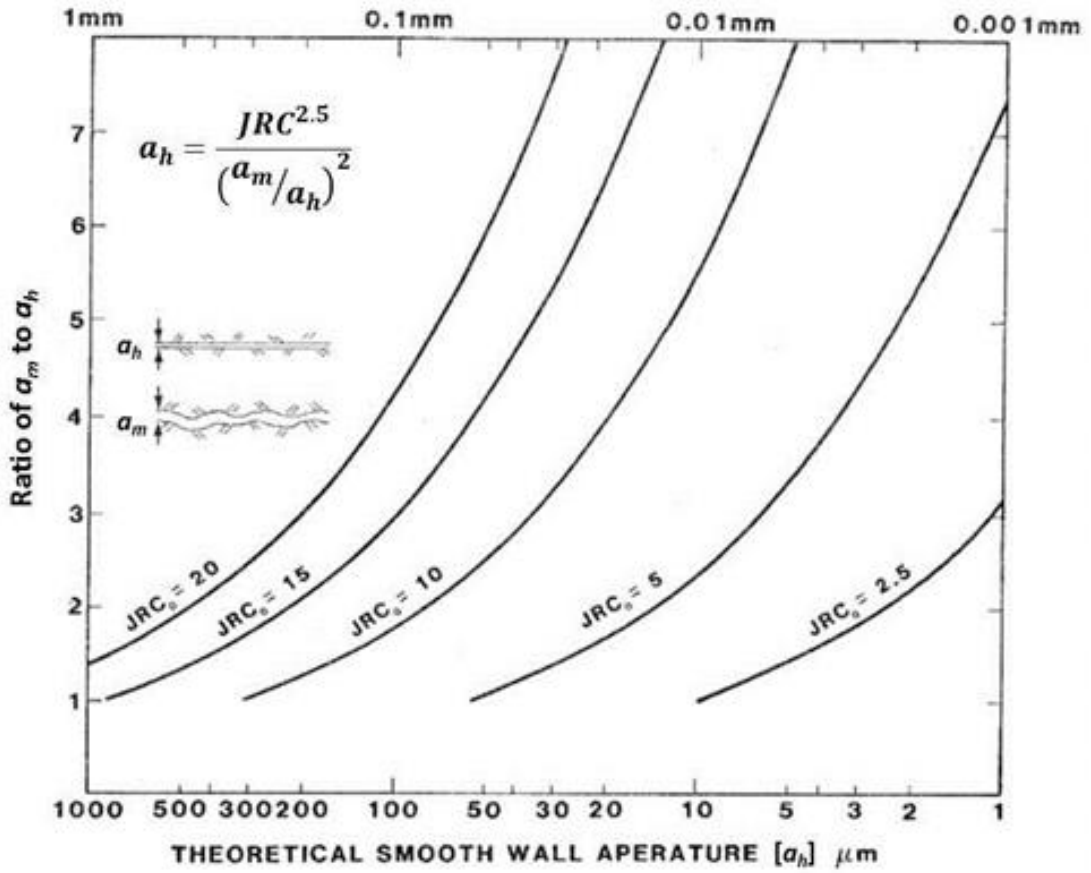

Figure 2.8 - Hydraulic and mechanical aperture in relation to JRC (after Barton, 1985)

2.3.4 *Contact Area*

Contact area is important in determining the amount of open fracture area that is able to conduct flow. Field measurement of contact area is effectively impossible due to the fact that the fracture must be opened to be analysed, thus destroying the in-situ characteristics of the sample.

A more sophisticated method of analysing contact area is scanning opposing faces of a fracture in three dimensional space and matching the two faces with modeling software, as illustrated in Figure 2.9. The change of contact area with stress can be estimated with poroelastic modeling. Sophisticated imaging techniques used to determine aperture require highly detailed images of fractures. These images can be processed to determine

contact area.

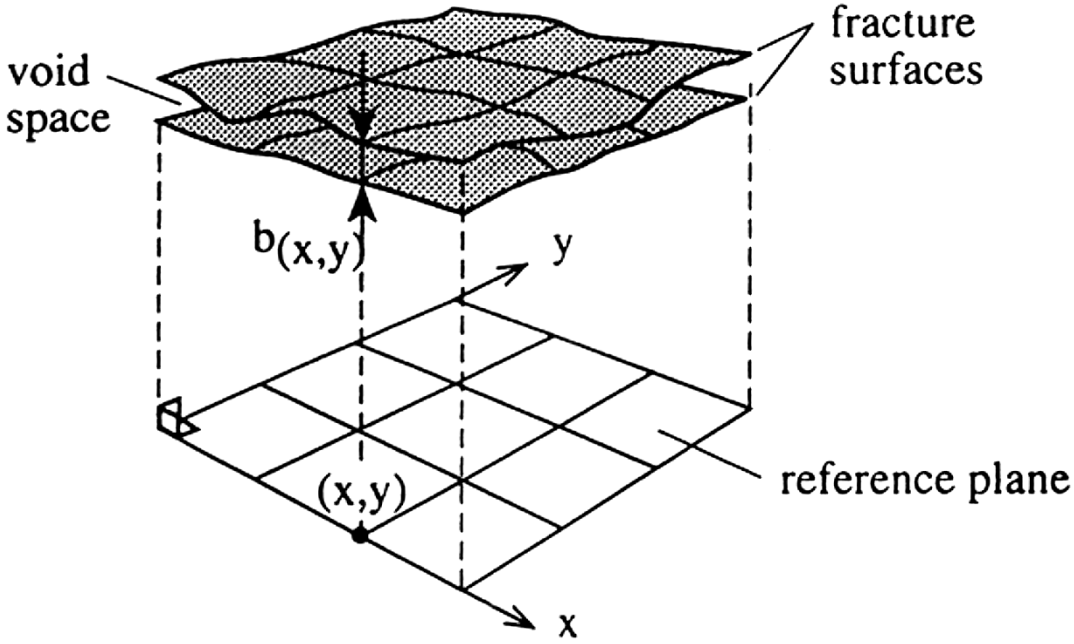

Figure 2.9 - Matched fracture image scans (Hakami and Larson, 1996)

2.3.5 *Joint Stiffness*

Joint stiffness is a parameter that characterizes the change in fracture aperture resulting from a change in normal stress (i.e., load acting normal to the fracture plane, divided by total fracture surface area). Fracture closure occurs by elastic compression of asperities or/or permanent deformation. In general, joint stiffness decreases as normal load increases. As a fracture closes with increasing normal load, an increasing number asperities come in contact with one another, thus distributing load across a larger surface area and increasing the resistance to closure. A typical joint stiffness response can be seen in Figure 2.10, in which Goodman (1989) illustrates fracture closure (Δa) vs normal stress (σ). This figures shows that joint stiffness decreases with increasing normal stress, and at sufficiently high stresses may approach a condition in which normal load is fully distributed across the fracture and no more closure will take place unless shearing occurs.

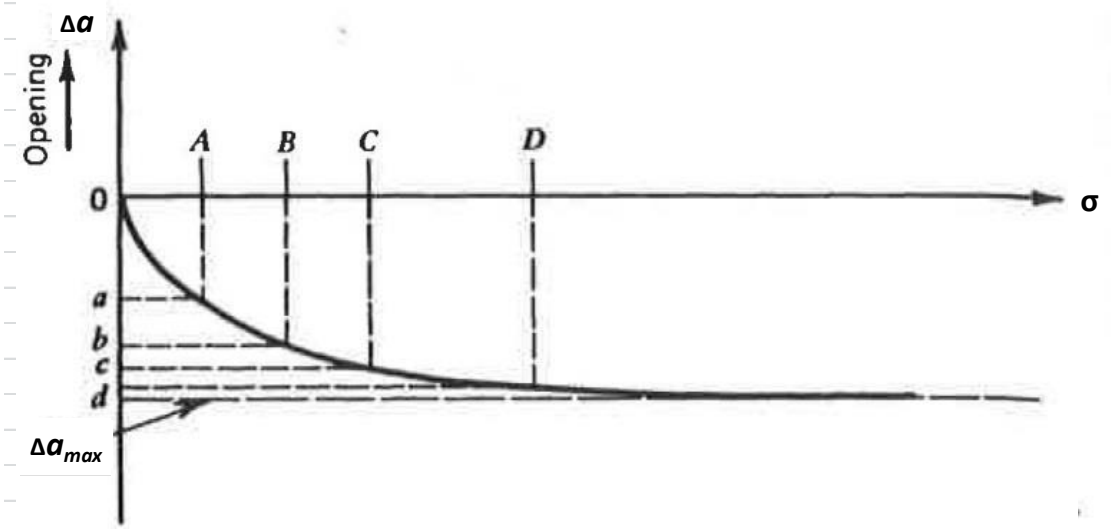

Figure 2.10 – Change in aperture vs normal stress (after Goodman, 1989)

2.4 FLUID FLOW IN ROCK MASSES

A rock mass is comprised of two components: 1) intact rock (matrix), and 2) fractures. Fluid flow through a rock mass depends on the properties of the matrix, fractures and the interaction between the two. Matrix flow results from the flow through interconnected pores within the rock. If pores are not directly connected, flow still may occur along mirco-discontinuities, intra-crystalline defects and fissures at crystal interfaces (Lee and Farmer, 1993). The hydraulic conductivity of the rock matrix can vary significantly and depends on the aperture of the pores and their interconnectivity. As discussed, racture flow also occurs (often predominantly) through the fractures in a rock mass. Fractures act as conducts to flow and can be large sources of inflow.

The interaction between these two processes can be very complex. Figure 2.11 illustrates five simplified scenarios of flow through a rock mass. In Figure 2.11(a) a homogeneous environment is shown in which simple isotropic flow can be expected from matrix alone. The heterogeneous environment shown in Figure 2.11(b), results in

matrix flow that has a preferential flow direction. Figure 2.11(c) illustrates a fracture in a conductive porous medium. This is one on the most complex flow situations in which the fractures and porous medium can both significantly contribute to the overall flow potential. Figure 2.11(d) displays a fracture in a tight porous medium. In this situation, the flow is fracture dominated; however, there is minor influence from the matrix. Figure 2.11(e) illustrates fracture through an impermeable medium. In this situation flow is completely fracture dominated as the matrix is incapable of conducting fluid.

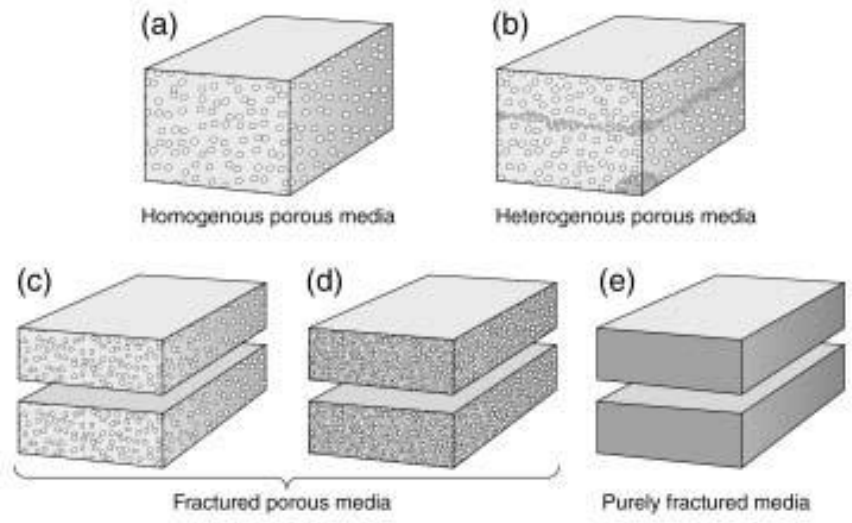

Figure 2.11 - Flow scenarios through a rock mass (Cook, 2003)

Analysis of flow through a rock mass depends primarily on the relationship between matrix and fracture flow. Two main approaches are used when studying flow through a rock mass. The traditional and simpler approach is called the continuum method, in which the rock mass is treated as a porous medium and the effects of individual fractures are ignored.

The alternative approach is to assess the fractures individually and study the flow on a much smaller scale. The contribution of the matrix can be added into the analysis. The fracture analysis method requires a significant amount of data to conduct a proper analysis.

2.4.1 *Continuum Method*

For the continuum method, the rock mass is treated as a continuous porous medium which has constant transport properties over the representative volume (REV) of the rock mass. The effects of fractures and the matrix are averaged over the extent of the REV to obtain representative properties of the rock mass. This approach works well when inflow is being determined on a large scale. In rock masses that are highly fractured, the effects of individual fractures are less significant on a large scale, so the continuum method is well suited. Limitations arise when a small number fractures control the behaviour of the representative volume, in which case, assumptions of constant properties over the length of such a rock mass may not be tolerable.

The process of fluid transport through a porous medium is characterized by Darcy's law, as follows:

$$Q = KiA \qquad [2.4]$$

Where Q is flow in m^3/s, K is the hydraulic conductivity of the medium in m/s, i is the hydraulic head gradient at the point of measurement (dimensionless; m of head per unit length, in m), and A is the cross-sectional area of the medium in which flow is occurring (m^2). This equation can be simplified to solve for Darcian Velocity or specific discharge by removing area from the equation, as follows:

$$q = Ki \qquad [2.5]$$

The Darcian Velocity assumes flow occurs through the entire cross-sectional area. In reality, flow occurs only through the pore space. The true velocity, or seepage velocity, is the velocity of the pore fluid as it travels through the pores in a rock mass. Only a fraction of the bulk volume is available for flow, and the flow path is generally tortuous,

so a larger velocity results. To calculate seepage velocity the Darcian Velocity is divided by the porosity of the sample as shown.

$$V = \frac{Ki}{n} \qquad [2.6]$$

Where V is the seepage velocity, K is the hydraulic conductivity (m/s), i is the pressure gradient (m of water) and n is the porosity of the sample.

The continuum approach assumes laminar flow through a saturated isotropic homogeneous medium. Further, many applications of the continuum method assume that steady state conditions exist, because this simplifies analysis. Collectively, these assumptions limit its applicability.

2.4.2 *Discrete Fracture Flow Method*

The alternative to the equivalent porous medium approach is the discrete network model, in which each fracture is modeled individually in a rock mass. In some situations, a single equivalent fracture can replace several related fractures (Lee and Farmer, 1993). However, in most cases the effect of the matrix is assumed to be negligible. In more sophisticated models, fracture-matrix interactions are included as well. Selection between the models usually depends on the information available and the heterogeneity of the rock mass (Lee and Farmer, 1993)

To more accurately assess flow through a rock mass, the role of the fractures in the rock mass must be properly understood. Fractures often control the behaviour of a rock mass. The ability to predict the flow behaviour in fractures leads to a better ability to predict the flow behaviour through a rock mass.

Fractures can be simulated in a variety of methods. For example, early methods were developed by comparing joint flow to pipe flow. Poiseuille's law is the most basic

equation used; it was developed for a circular conduit. Current fracture flow equations evolved from Poiseuille's equations. Poiseuille conducted experiments of controlled flow through glassware in the early 1800's (Sutera and Skalak, 1993). His test consisted of precise observations of fluid through a narrow tube with control over pressure and temperature.

Romm (1966) demonstrated how the Poiseuille law could be adapted to represent laminar flow through a set of smooth parallel plates with a constant hydraulic aperture a_h (Romm, 1966), which is referred to as the parallel plate law, equation [2.7].

$$K = \frac{\rho g}{12\mu}(a_h)^2 \qquad [2.7]$$

Where K is the hydraulic conductivity, measured in m/s, g is the acceleration due to gravity at 9.81 m/s^2, μ is the dynamic viscosity which has a value of 1.0 (Pa·s), ρ is the density of water, 1000 kg/m^3 under standard temperatures and pressure, and a_h, is the aperture in meters.

When equation [2.7] is solved for flow rate the result is dependent on the cube of the aperture; this form of the equation is commonly referred to as the cubic law (Lee and Farmer, 1993).

Smooth parallel plate flow has been studied in depth by Snow (1969), Romm (1966), Louis (1969), Baker (1955) and many more. The topic has been studied under a wide range of conditions demonstrating that the equation is usually accurate, but loses accuracy in tight rough fractures where the flow path is more difficult to define.

2.4.3 *Non Ideal Fracture Flow Behavior*

Natural fractures are rough with variable apertures. Small scale roughness can cause eddies and velocity changes in flow that result in head loss and a reduction in flow. Large scale roughness or waviness increases the length and tortuosity of the flow path, which results in extra energy loss. These effects may cause flow to become turbulent which results in further energy loss.

The parallel plate law has several conditions that are not met under many natural circumstances. Laminar flow is one of these assumptions. Both laminar and turbulent flows can exist in a fracture. The form of flow occurring throughout a fracture is a function of the roughness, the aperture of the fracture and the velocity of water through it. The Reynolds number, *Re*, is a ratio that is used to assess if a flow is laminar or turbulent. The Reynolds number itself is the ratio of the inertial forces to the viscous forces in a flow system (Iwai, 1976).The Reynolds equation for fracture flow is derived from that of a long and wide channel with a rectangular cross section (Sarkar et al., 2004) and can stated as follows:

$$Re = \frac{V \rho a_h}{\mu} \qquad [2.9]$$

Where a_h is the hydraulic aperture in metres, V is the flow velocity in m/s, μ is the dynamic viscosity and ρ is the density of water. In pipe flow a Reynolds number of 2300 or greater usually indicates turbulent flow, and less than 2300 is laminar. In non-ideal pipe flow, roughness and aperture both affect this boundary value of 2300. Fracture roughness affects flow by causing increased friction along the fracture wall and increasing the tortuosity of the flow path, both of which lead to turbulent flow. The surface roughness index, *S*, is a commonly used method for quantifying fracture roughness.

$$S = \frac{r_m}{a_h} \qquad [2.10]$$

Where r_m is the micro roughness, and a_h is the hydraulic aperture. The surface roughness index is the primary method used in determining if flow is parallel or non-parallel. Parallel flow being considered two straight edges of the fracture, whereas non parallel indicates a more tortuous flow path. Non parallel flow occurs when $S > 0.333$. Figure 2.12 shows the manner in which *S* and *Re* determine if a flow is laminar or turbulent.

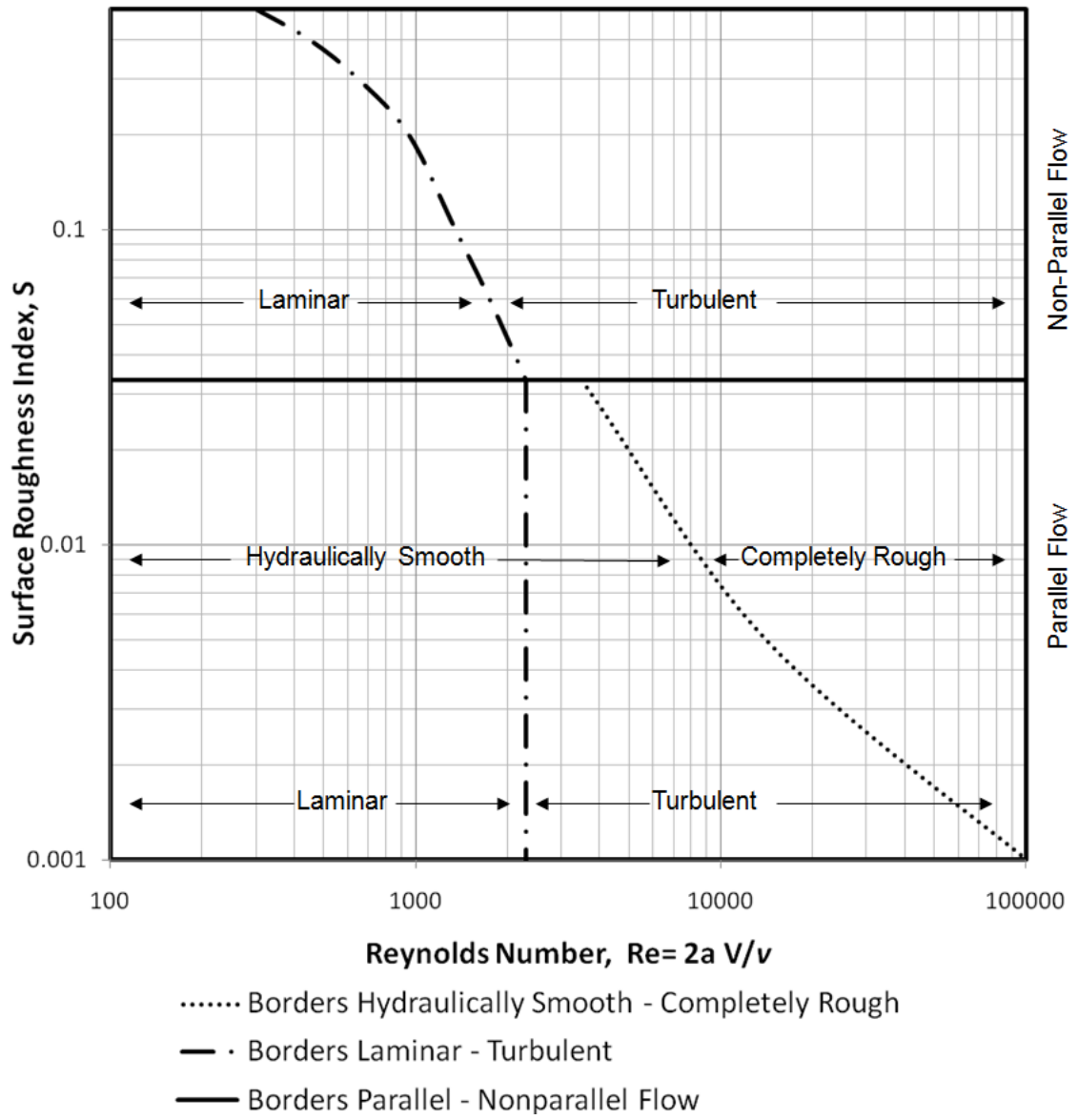

Figure 2.12 - Flow regimes as a function of surface roughness and Reynold's number (after Louis, 1969)

2.4.4 *Analysis of Non-Ideal Fracture Flow*

Limize conducted the first systematic analysis of controlled flow through simulated fractures in 1955 (from Louis, 1969). He tested a range of 20 cm joint models, as shown in Figure 2.13, to assess the influence of the position of the joints, width of the joints,

roughness, shape and structure of the joint walls. Tests were run on eight different idealised fracture shapes at varying apertures.

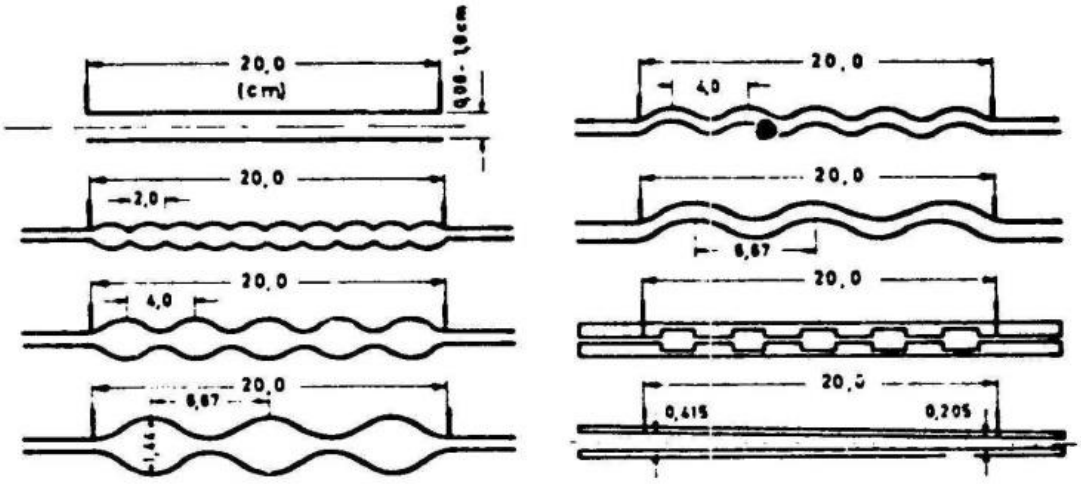

Figure 2.13 - Shapes of joint walls used in experiments by Limize, flow directing being left to right (after Louis, 1969)

Louis (1969) conducted research several years after Limize; however he was initially unaware of Limize's work. Both researchers came to similar conclusions through their independent tests. Louis ran laboratory tests on fractures similar to Limize's; however he simulated real fractures with varying shapes and roughness, unlike Limize's idealised fracture shapes. Louis's goal was to conduct tests in smooth, rough, and open joints. He also studied the effects of infilling may have on a fracture. Both Limize and Louis developed semi-empirical equations that described non-parallel fracture flow under laminar and turbulent conditions. Louis' equation for laminar non-parallel fracture flow is displayed as follows:

$$K = \frac{\rho g}{12\mu\left[1+8.8\left(r_a/a_h\right)^{1.5}\right]}\left(a_h\right)^2 \qquad [2.11]$$

Where ρ = density, g = acceleration due to gravity, μ = kinematic viscosity, r_a = micro roughness, and a_h = hydraulic aperture.

Using equations 2.3 and 2.12 Scesi and Gattinoni (2005) derived an equation for laminar non-parallel flow based on JRC as follows:

$$K = \frac{g}{12\nu\left[1+8.8\left(0.5-\frac{a_h}{(JRC)^{2.5}}\right)^{1.5}\right]}(a_h)^2 \qquad [2.12]$$

Where ν = dynamic viscosity, and JRC = Joint Roughness Coefficient. Since JRC is a dimensionless parameter, the units of the equation do not work out. This is because an empirical relationship was used to derive the equation. The effects of this will be explored later in Chapter 4.

CHAPTER 3 FIELD INVESTIGATIONS

3.1 BACKGROUND

Cameco collected a substantial data set during investigations for eight shaft locations in the Athabasca Basin. Data was retrieved from boreholes that were drilled in preparation for shaft sinking. Of the eight shafts, five were completed at the time of this study including McArthur River shafts 1, 2, and 3 and Cigar Lake shafts 1 and 2. The three shafts that were still in the planning stage included shafts 1 and 2 at the potential Millennium mine, and shaft 4 at McArthur River. Approximately two years into this research project, an additional two holes (SP-001 and SP-002) were drilled to further prepare for shaft 4 at McArthur River. Data collection and analysis for those holes was conducted by SRK Consulting (SRK).

A range of tests had been conducted on each borehole to investigate the conditions that were to be encountered during shaft sinking. Core logging had also been conducted on all boreholes. The nature of the data obtained from the core logs was reasonably consistent. The strength, color, composition, and condition of the core and fractures had been logged by the aforementioned contractors. Drilling-induced fractures had been differentiated from natural fractures and were left out of the logs. Fracture properties that were noted included orientation, colour, staining, infilling, frequency, roughness and RQD (Rock Quality Designation). From the core logging details, the core was usually classified into the empirical descriptive relationships of RMR (Rock Mass Rating) and Q (Quality Designation). Figure 3.1 shows an example of data collected by Golder for one of the McArthur River Shaft 4 pilot boreholes; borehole MC-316.

Down hole geophysical surveys were conducted following the drilling of each borehole. The selection of surveys varied from borehole to borehole. Methods used included caliper, natural gamma-ray, gamma-gamma (density), neutron, fluid temperature, resistivity, spontaneous potential, acoustic borehole imaging, optical borehole imaging, and sonic logs. Figure 3.2 displays an example of logs provided by Golder (2009).

Packer testing is a primary method of hydrogeological assessment. It is used to measure the bulk hydraulic conductivity of a selected interval, which is isolated by inflating packers in the borehole. The rock mass is stimulated by injecting or withdrawing water. The response of the hydraulic pressure is recorded and in turn used to calculate the hydraulic conductivity. Packer test intervals ranged from 3 m to 70 m.

Relating packer testing to core logging, yields insight on the distribution of conductive features over a test interval. In most cases hydraulic conductivities are controlled by the presence of one or two features. Klimczak et al (2010) demonstrated that discontinuities that have a large hydraulic conductivity are the result of a large aperture, and due to the mechanisms of formation, larger apertures coincide with larger discontinuity lengths. Packer tests highlight intervals with a high bulk hydraulic conductivity number, which require in depth analysis to help qualify where the highest flow potential within the interval occurs.

Testing methods that were used on each borehole varied significantly, which made a comparison of results between boreholes difficult. A detailed investigation of pilot borehole MC 316 was selected for a focused study due to the comprehensive nature of the available data set. A review and analysis of the MC-316 dataset is given in the following section, followed by a review and analysis of data for borehole SP-001.

Three main fracture sets have been consistently encountered from exploration holes in the Manitou Falls Sandstone (Golder Associates, 1999). The dominant fracture set occurs along horizontal bedding planes and has a spacing of several centimeters to several meters. The second and third fracture sets are vertical to sub-vertical and are perpendicular to one another. The two sub-vertical fracture sets have spacings between several centimeters to tens of meters. It should be noted that the observed spacing of the sub-vertical sets have been made from vertical boreholes which are near parallel to the fracture sets. True fracture spacing is almost certainly much closer than observed.

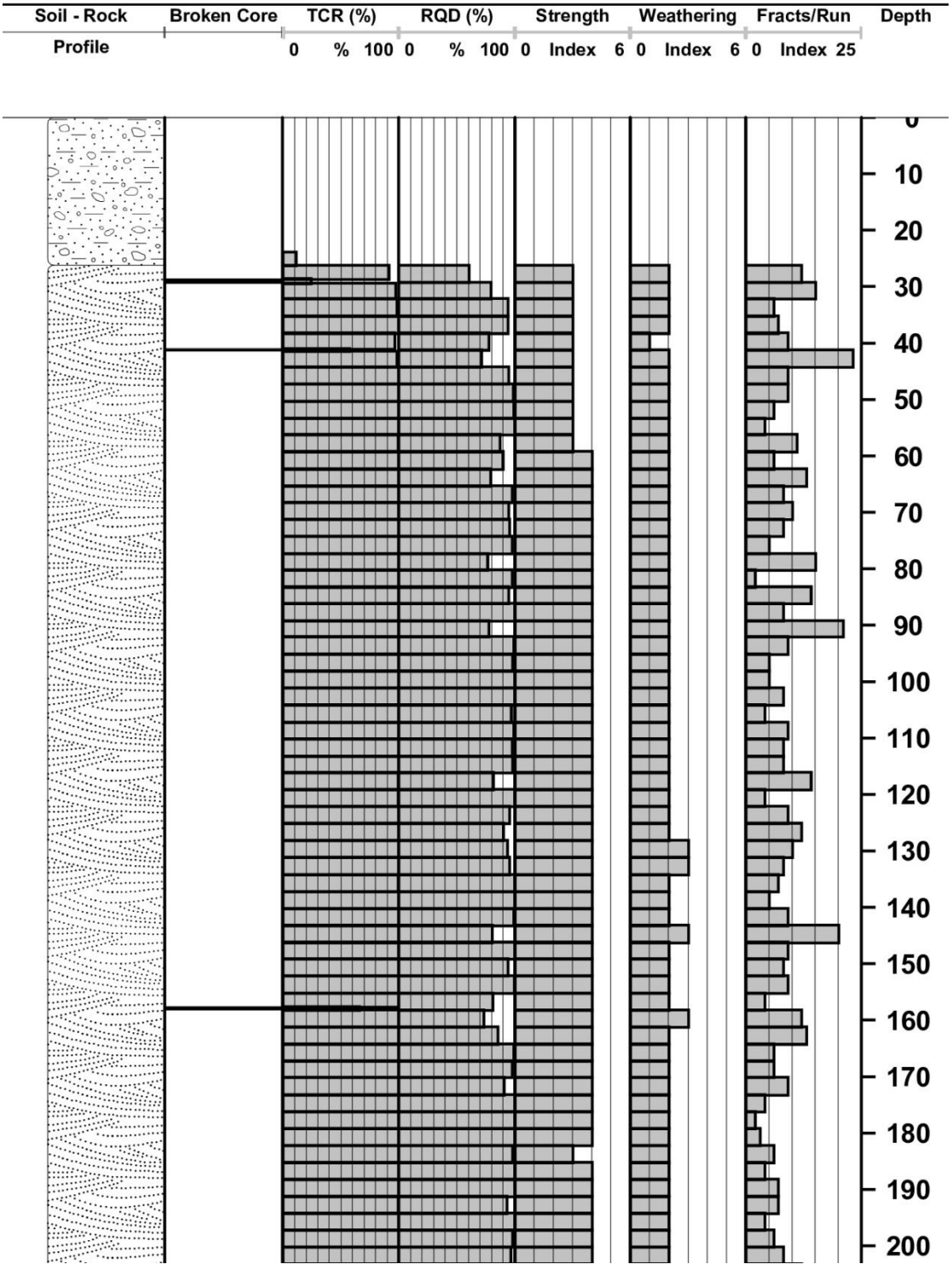

Figure 3.1 - Sample of core logging data for borehole MC-316 (Golder Associates, 2009). Where, TCR is Total Core Recovery, RQD is Rock Quality Designation, and fracts/run, is the number of fractures encountered per run.

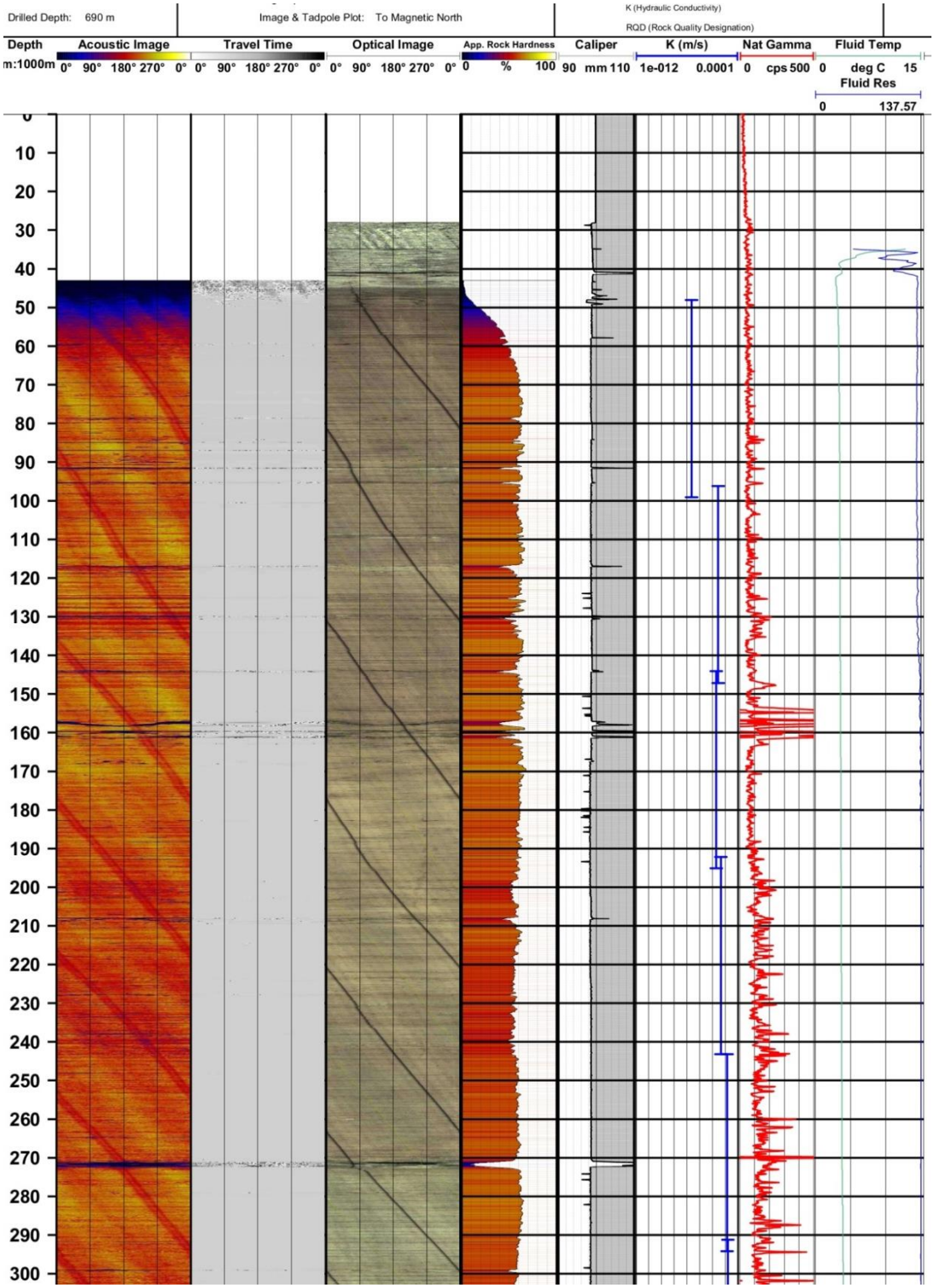

Figure 3.2 - Sample of geophysical logging for borehole MC-316 (provided by Golder Associates, 2009)

3.2 FOCUSED STUDY OF BOREHOLE MC-316

3.2.1 *Packer Testing Results*

Packer testing is likely the most common method used for assessing rock mass hydraulic conductivity, though there are several challenges associated with this test. Hydraulic conductivity (*K*) values can range over approximately eight orders of magnitude, with depth-wise *K* variations often occurring on length scales smaller than the packer interval. As such, packer test results can be very sensitive to packer placement. Common sources of error in packer testing include: flow short-cutting, non Darcian flow, and misinterpretation of initial equilibrium conditions. There can also be a significant error in the curve fitting used to interpret the results, as test datasets often don't match the idealize curves used in the fitting process.

With these error sources and sensitivities in mind, it should be recognized that the hydraulic conductivity values from packer tests are best regarded as order-of-magnitude estimates. Nevertheless, these are believed to represent the best practically-available estimates of in-situ hydraulic conductivity, and are useful for identifying zones of relatively high and low hydraulic conductivity.

MC-316 had a comprehensive packer testing program. For rock masses possessing fractures which dominate flow, the interpreted hydraulic conductivities from packer testing represents equivalent continuum values. Figure 3.3 shows hydraulic conductivities for various intervals versus depth. The hydraulic conductivities displayed are the average of values determined through falling head tests and constant rate injection tests. The results are quite variable and there are no obvious trends with K and depth.

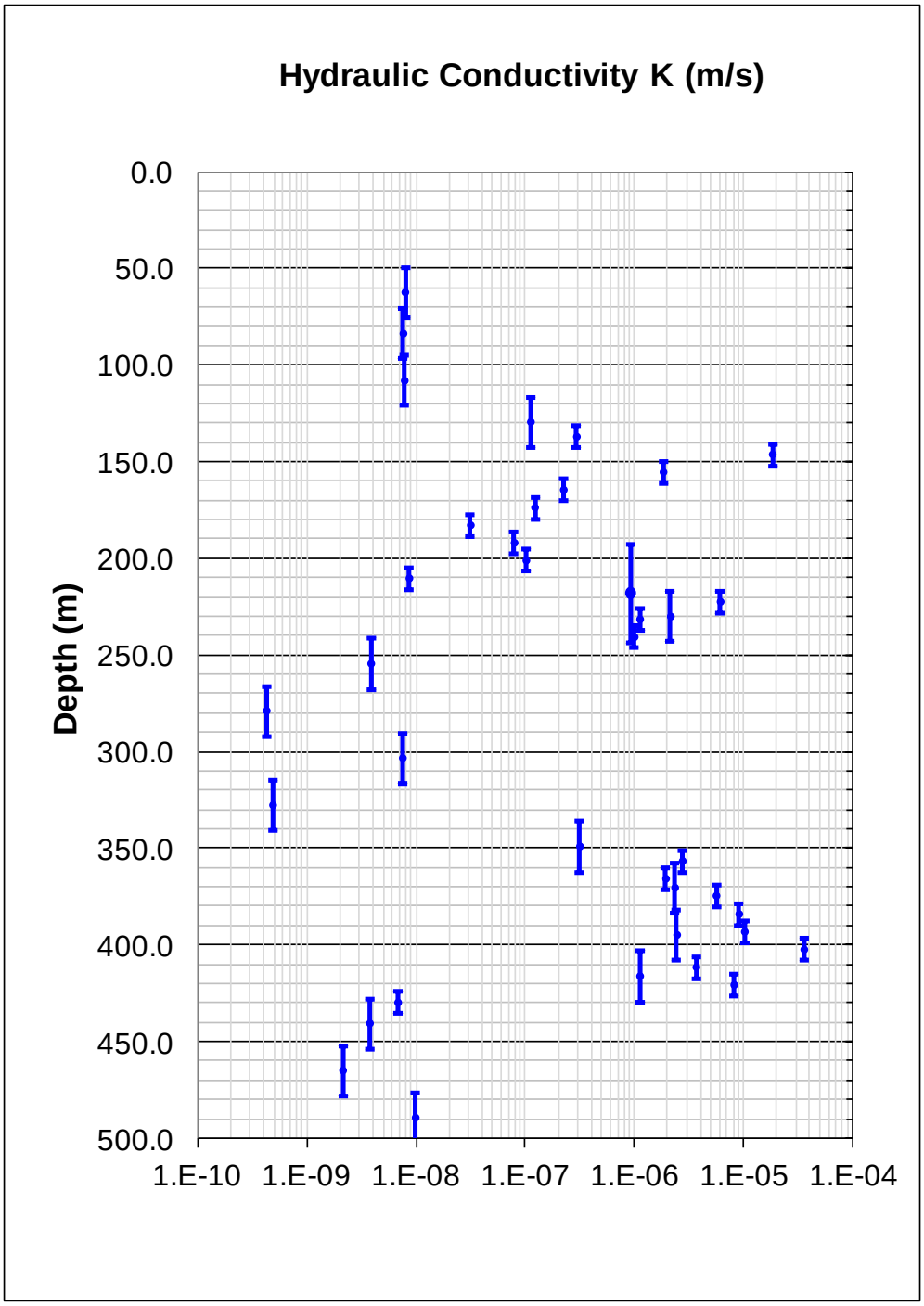

Figure 3.3 - Hydraulic conductivity versus depth for pilot borehole MC 316

3.2.2 *Fracture Orientation for MC-316*

As noted in section 2.2, previous investigations have stated that three fracture sets are present in the Manitou Falls Formation at the McArthur River Mine; one horizontal, and two sub-vertical (Golder, 1997, 1998, 2002, Beattie, 2007). Figure 3.4 displays a stereonet generated from fracture data for the Manitou Falls Formation, extracted from an optical borehole image log run by Golder (2009) for borehole MC-316. The figure shows the poles for all of the interpreted fracture planes, and contours of fracture density as determined using the Terzaghi correction to estimate the true distribution. This figure shows two clear fracture sets; one sub-horizontal, and one sub-vertical (striking east-west). Though sub-vertical fractures with other strike directions are present, they do not form a well-defined fracture set. No image data was available for SP-001, which is discussed later, so it was not possible to assess the fracture sets in that borehole. For simplicity, in this work it is assumed that the previously reported scenario (i.e., one horizontal fracture sets plus two sub vertical fracture sets) is broadly representative (though further investigation of this matter is recommended).

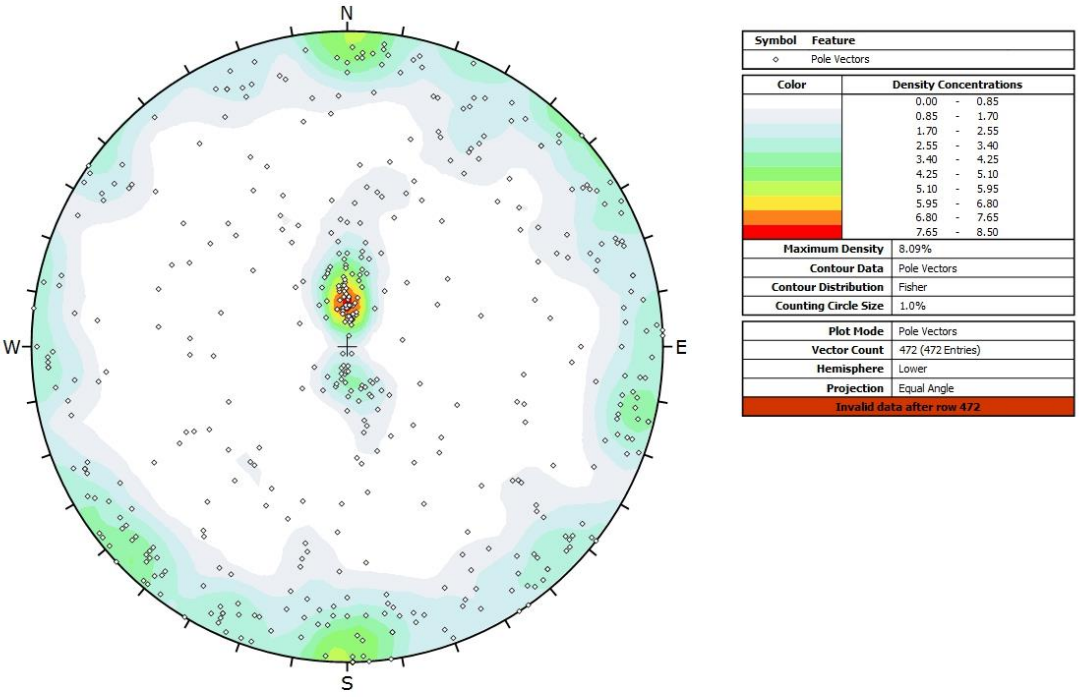

Figure 3.4 - Stereo net of fracture data from McArthur River shaft pilot hole MC-316. Black dots show poles to fracture planes, in a lower-hemisphere equal angle projection, and contours show Terzaghi-corrected fracture densities.

3.2.3 *Fracture Characterization*

Original core logging was not focused specifically on a hydrogeological assessment. To gain a further understanding of the properties of the Manitou Falls Formation, two site visits were conducted; Nov 10, 2009 and June 11, 2010. The core of shaft pilot borehole MC-316 was re-logged focusing on whether fractures were healed, discontinuous, and contained staining, infilling or gouge. The hole was logged from surface to a depth of 460 m, where basement rocks were encountered. The basement rocks below the sandstone are much tighter and have a lower hydraulic conductivity. Fracture properties relating to flow would not be consistent over the two units so analysis focused solely on the Manitou Falls Formation. Core for the interval ranging from 270.57 m to 285.52 m was missing. From core photos it was determined that there are two sub-vertical fractures in this interval, and estimates of their attributes were made for use in this analysis.

Packer test records were used as a reference during the core logging conducted during this site visits. Generally, it was observed that zones with iron staining coincided with intervals of elevated hydraulic conductivity. Sub-vertical fractures seemed to be most prominent in higher hydraulic conductivity zones, and these fractures contained a large degree of staining. Nine core samples were obtained from site and brought back to the rock mechanics laboratory at the University of Saskatchewan for further investigation. Figure 3.5 and 3.6 shows a highly altered piece of core taken from a depth within the interval of highest measured hydraulic conductivity.

Several interesting trends were observed in the core. Iron staining, identified as limonite by Cameco, was most concentrated on fracture surfaces in the intervals of high hydraulic conductivity. To further investigate the staining on the fractures several samples were sent to GR Pertrology Consultants for X-Ray Diffraction (XRD) and X-ray Energy Dispersive Spectrometry (EDS) analyses. An example of the results is shown in Figure 3.5.

Scanning Electron Microscopy (SEM) analyses were also conducted. The weathered surfaces were found to be iron and manganese rich compared to the matrix, and with minor amounts of calcium and titanium. No manganese, calcium and titanium were found in the matrix. The matrix was primarily composed of quartz. Kaolinite, illite, siderite and pyrite were found also found on the stained surfaces. Full results from the reports from GR Petrology Consultants can be seen in appendix 1.

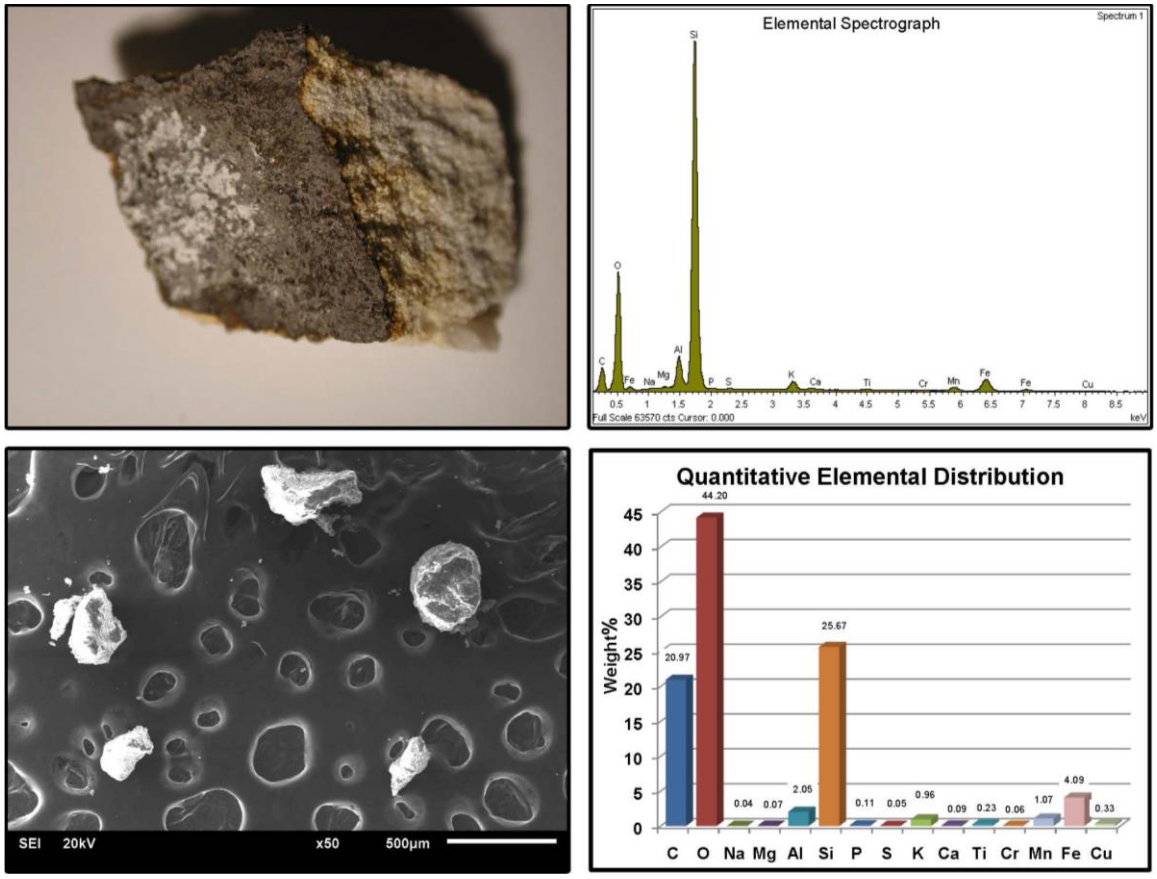

Figure 3.5 - Results from GR Petrology Consultants. Top left is a picture of the sample; top right is EDS; bottom left is SEM; and bottom right is EDS analysis.

Sub–vertical fractures (fractures with an angle less than 25° to the core axis) showed more signs of flow than the horizontal fractures in the higher hydraulic conductivity zones. There were also areas where all fractures, regardless of orientation, showed no signs of flow. Figures 3.6 through 3.9 show several fractures with signs of flow

alteration. The feature in Figure 3.9 was in the interval of greatest measured hydraulic conductivity, yet the fracture shown was the only one in that interval that showed signs of flow. The large crystals and prevalent alteration may be another indicator of flow. The quartz crystals observed were 3 to 8 mm in height, which would require a large apertures; in locations where apertures of this magnitude are not entirely filled with crystals, it seems reasonable to expect that hydraulic conductivities would be extremely high.

Figure 3.6 - Stained fracture with infilling, 301.77 m depth, MC-316

Figure 3.7 - Fracture with moderate-heavy limonite staining, 306.6 m depth, MC-316


Figure 3.8 - Fractured core that has two vertical joint sets and shows signs of flow, 214 m depth, MC-316

Figure 3.9 - Large crystal growth found in core, 214 m depth, MC-316

3.2.4 *Analysis of Fracturing – Hydraulic Conductivity Relationships*

As noted in section 2.3, flow through a rock mass can occur through the fractures and the matrix. Based on prior experience and observations made on site, it was deemed likely that flow in the Manitou Falls Formation is fracture dominated. This belief was later confirmed through laboratory testing which is presented Chapter 4, but it was also supported based a comparison of packer test data to observed fracture attributes.

With flow occurring predominantly through fractures, it can be expected that hydraulic conductivity would correlate strongly to fracture frequency. Figure 3.10 displays fracture frequency and hydraulic conductivity with depth. Fracture frequency corresponds well to two of the high potential flow intervals but fails to give an indication of the interval from 213 m to 245 m. Another method of describing the

fracture frequency is Rock Quality Designation (RQD). RQD is described as the percentage of core, in a core run, that is comprised of intact segments10 cm or greater in length. RQD and hydraulic conductivity versus depth can be seen in Figure 3.11. The results are similar to Figure 3.10, and offer little additional insight. As seen in Figures 3.10 and 3.11, a higher hydraulic conductivity can be expected if fractures are closely spaced. Inversely, it is shown that a low number of fractures does not necessarily indicate a low hydraulic conductivity, which is why the interval from 213 m to 245 m depth was not highlighted in Figures 3.10 and 3.11. If fractures control flow, but the total number of fractures is not necessarily indicative of a high hydraulic conductivity, other properties of the facture must play a prominent role as well.

To further compare the relationship between fractures and hydraulic conductivity, the hydraulic conductivity was graphed against the fractures per meter that were observed in the hydraulic conductivity interval (Figure 3.12). To account for varying lengths of packer intervals, the fracture count was normalized per 5 meters. An exponential trend line was fitted, with an R^2 value of 0.281, which is statistically significant at the P = 0.05 level. A P-value of less 0.05 was chosen to signify that the relationship is statistically meaningful and rejects the null hypothesis (DeCoursey, 2003).

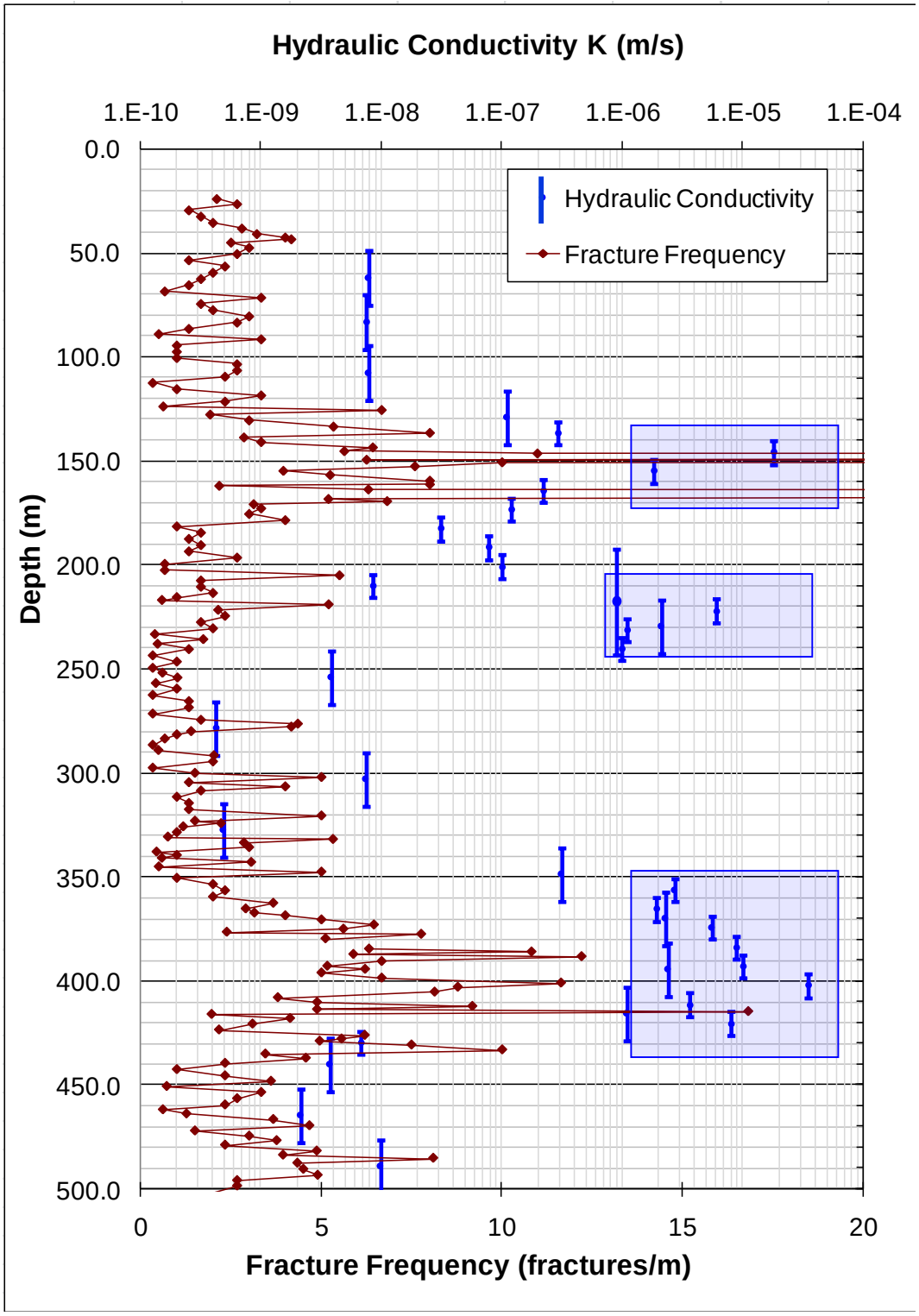

Figure 3.10 - Hydraulic conductivity versus fracture frequency, MC-316. Shaded regions highlight zones of high hydraulic conductivity.

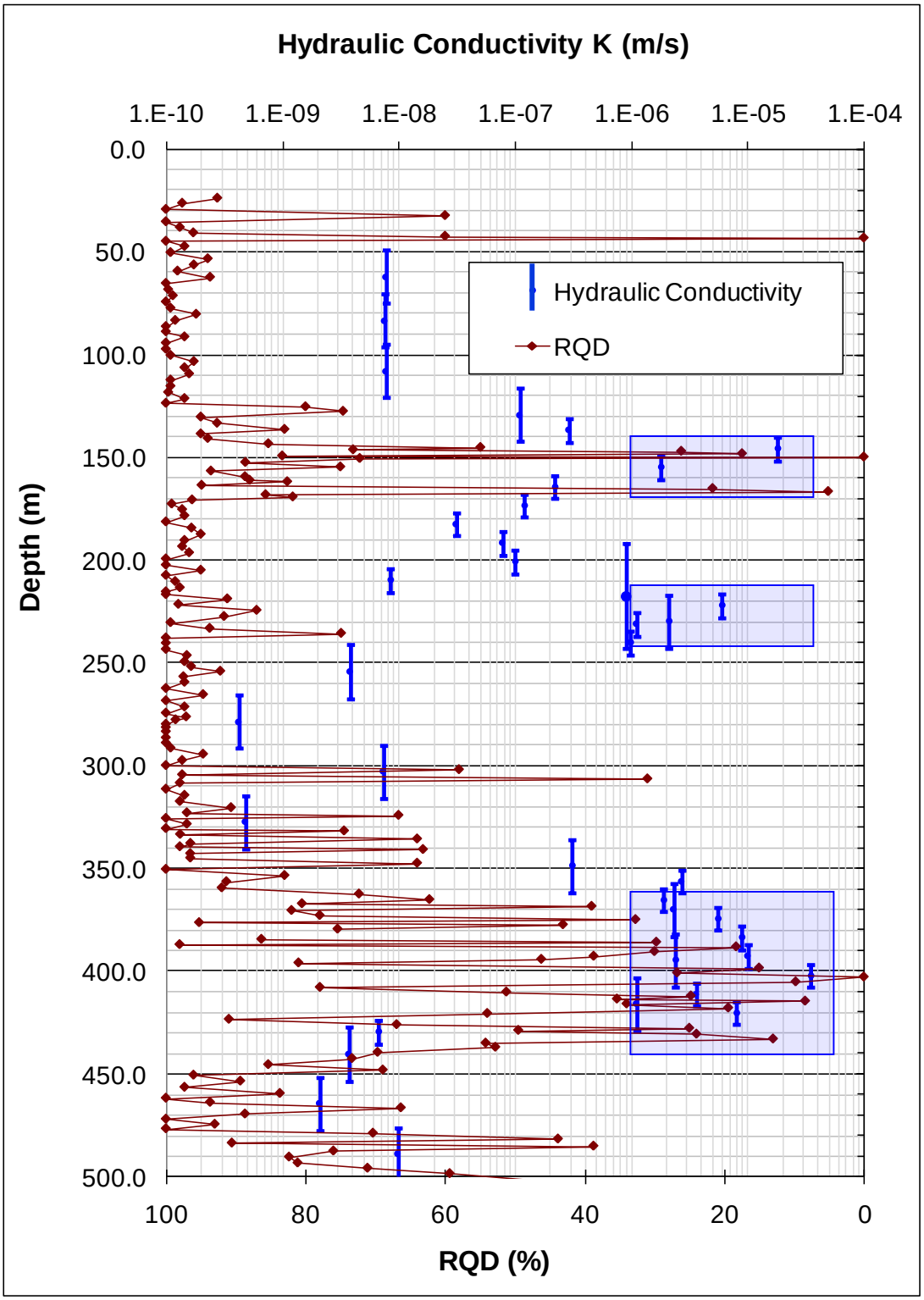

Figure 3.11 - Hydraulic conductivity versus RQD, MC-316. Shaded regions highlight zones of high hydraulic conductivity.

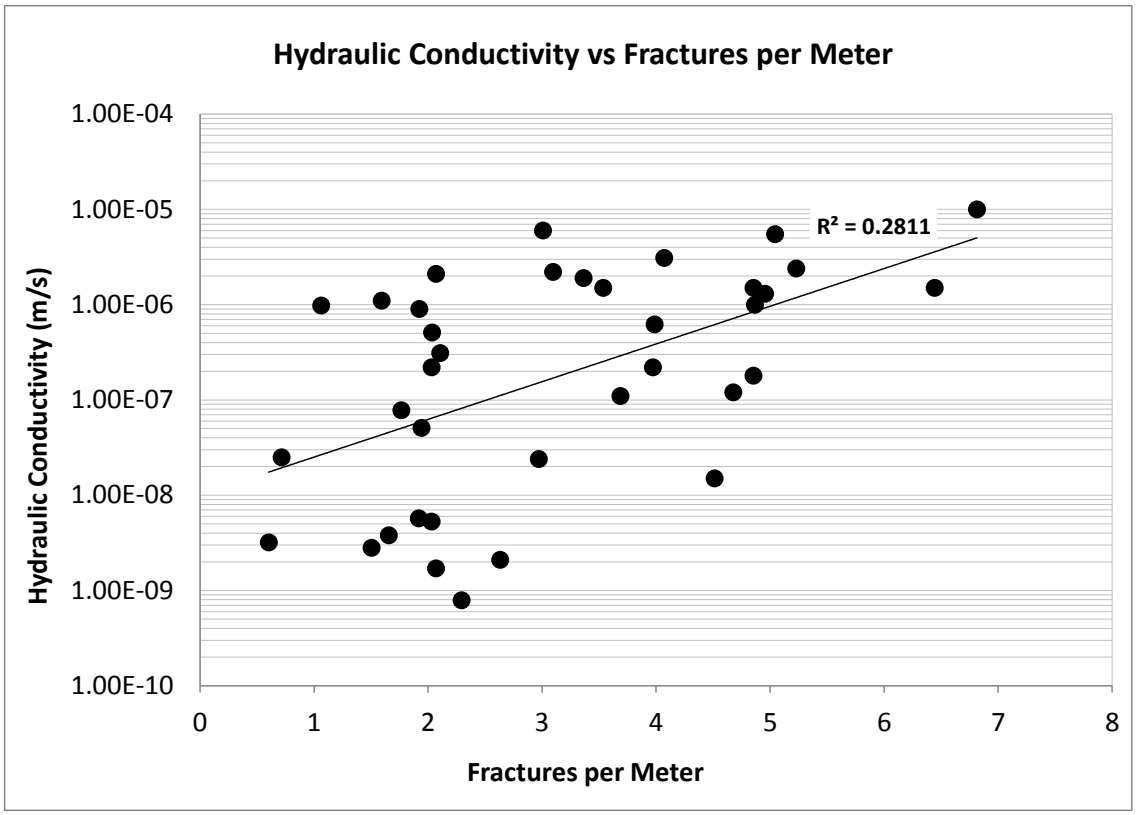

Figure 3.12 - Fractures versus hydraulic conductivity, MC-316

As noted in section 3.1, it has been proposed that larger inflow potential occurs in areas that have a greater number of sub-vertical fractures. This is due to better rock mass connectivity (e.g., communication between permeable beds and/or bedding-parallel fractures enabled by sub-vertical fractures) as well as the sub-vertical fractures possibly being more conductive. Though two sub-vertical fracture sets are believed to exist in the study area, it was not possible to distinguish between them because core orientation was not measured as it was drilled. The two fracture sets were therefore treated as one for analysis purposes. Upon separating the horizontal fractures from the sub-vertical fractures, more trends started to emerge. Figures 3.13 and 3.14 show horizontal and sub-vertical fractures per 5 meter interval. Based on visual examination of Figure 3.13, horizontal fractures seem to have no obvious relationship hydraulic conductivity.

In Figure 3.14, sub-vertical fractures often appear to increase in frequency at depth intervals of relatively high hydraulic conductivity. The relationship is not perfect, however. For example, there is not much of an increase in fracture frequency in the high hydraulic conductivity interval from 200 m to 250 m, nor is there an increase in sub-vertical fracture frequency between 450-500 m, where an increase in hydraulic conductivity is observed.

Figures 3.15 and 3.16 were generated to investigate the impact of sub-vertical and horizontal fracture frequencies on hydraulic conductivity through regression analysis. Table 3.1 summarizes the results. Figure 3.15 displays an exponential trend line relating hydraulic conductivity to the number of horizontal fractures per metre. R^2 = 0.0688 was obtained for this trend line, which is statistically insignificant at the P = 0.05 level. Sub-vertical fracture frequency (Figure 3.16) shows a stronger correlation; i.e., an exponential trend line fit to these data achieved R^2 = 0.317, which is statistically significant at the P = 0.05 level. The sub-vertical fractures prove to be a better indicator of hydraulic conductivity. Based on the data from borehole MC-316, it appears likely the sub-vertical fractures influence the hydraulic conductivity of the Manitou Falls Formation in the study area.

Table 3.1 Regression Values from Hydraulic Conductivity vs. Fracture Frequency Graphs

	R^2 Value	Significant at P=0.05
Total fractures per meter (Figure 3.12)	0.281	Yes
Horizontal fractures per meter (Figure 3.15)	0.0688	No
Sub-vertical fractures per meter (Figure 3.16)	0.317	Yes

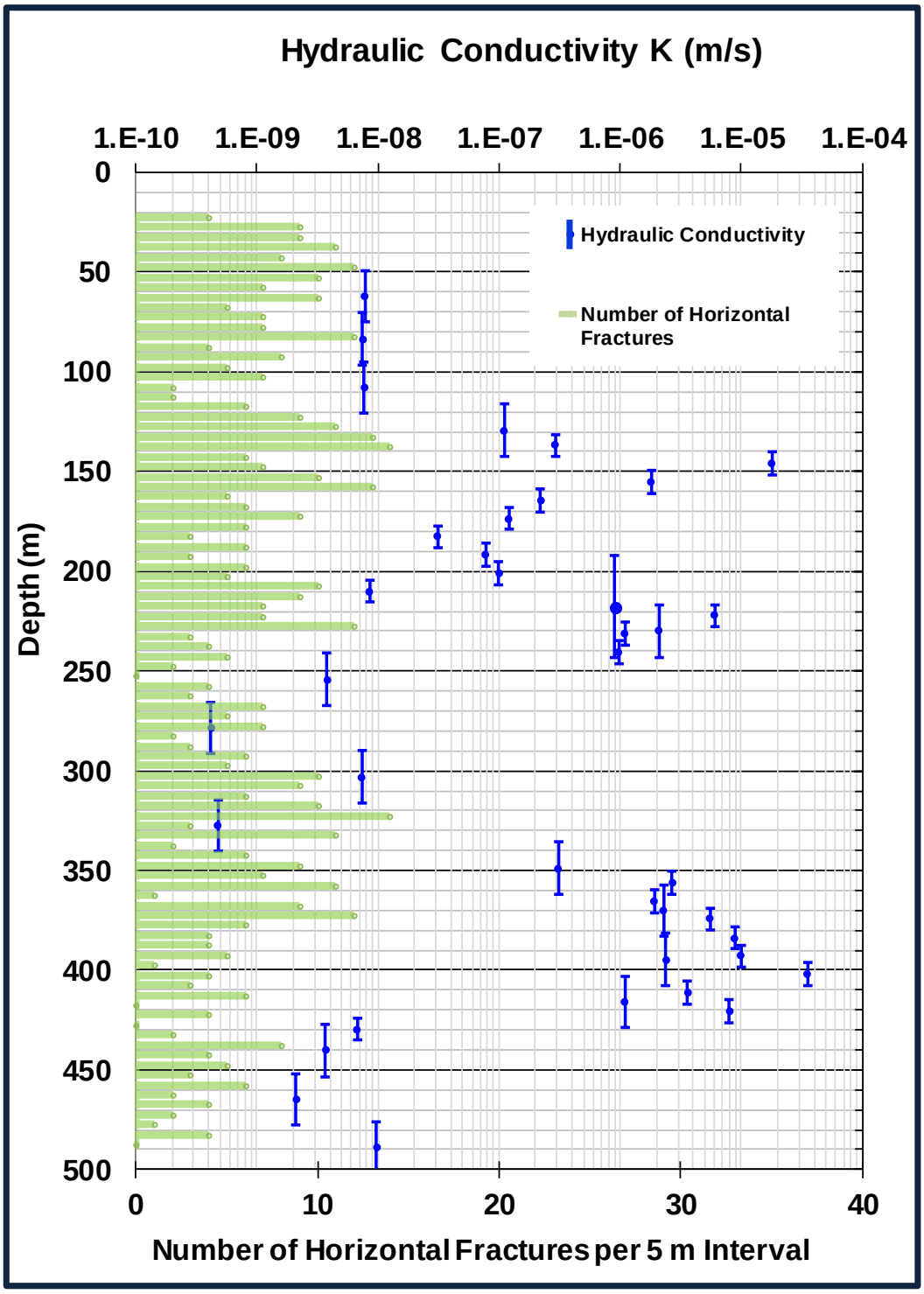

Figure 3.13 - Number of horizontal fractures per 5 m interval, MC-316

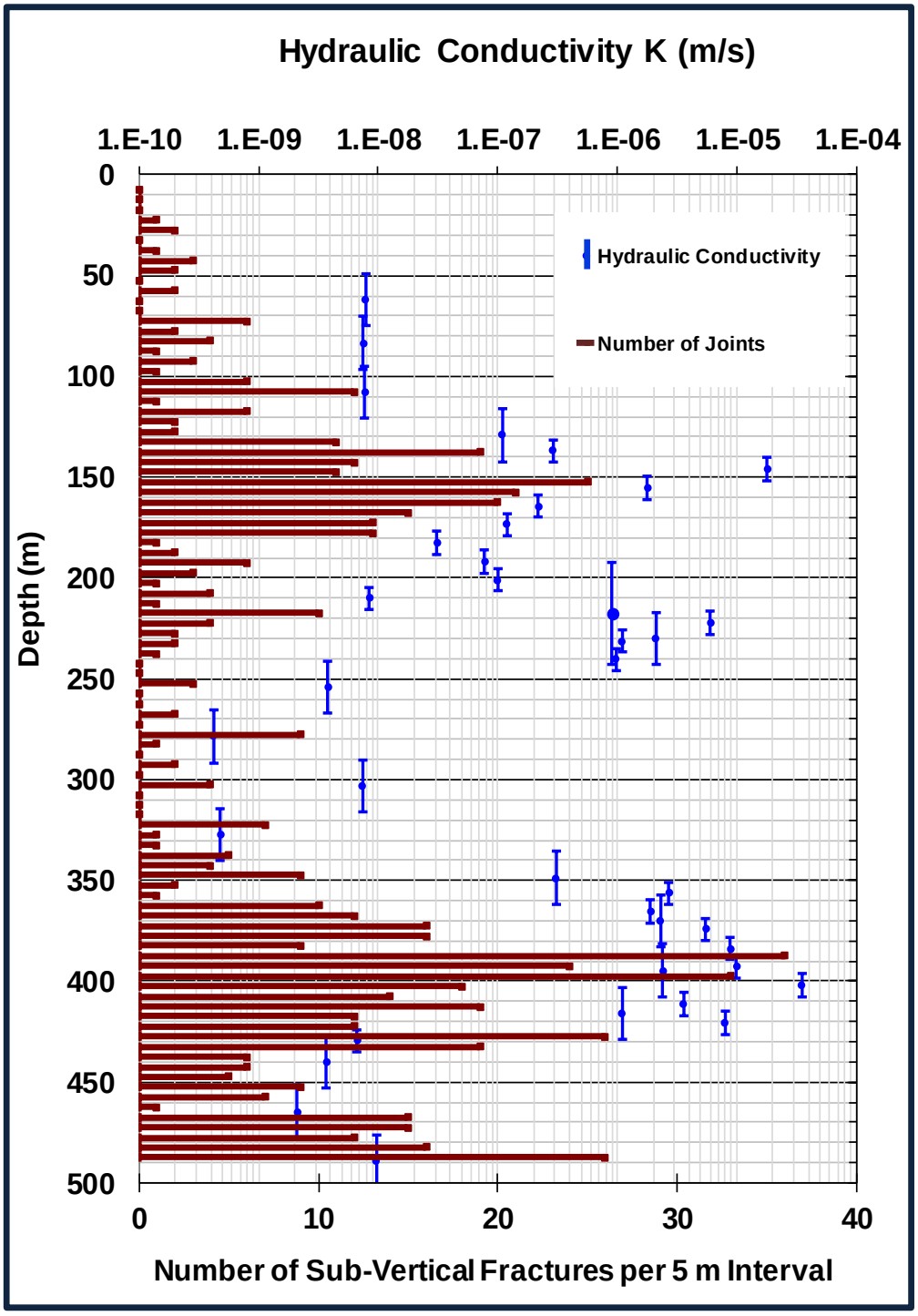

Figure 3.14 - Number of sub-vertical fractures per 5 m interval and hydraulic conductivities, MC-316

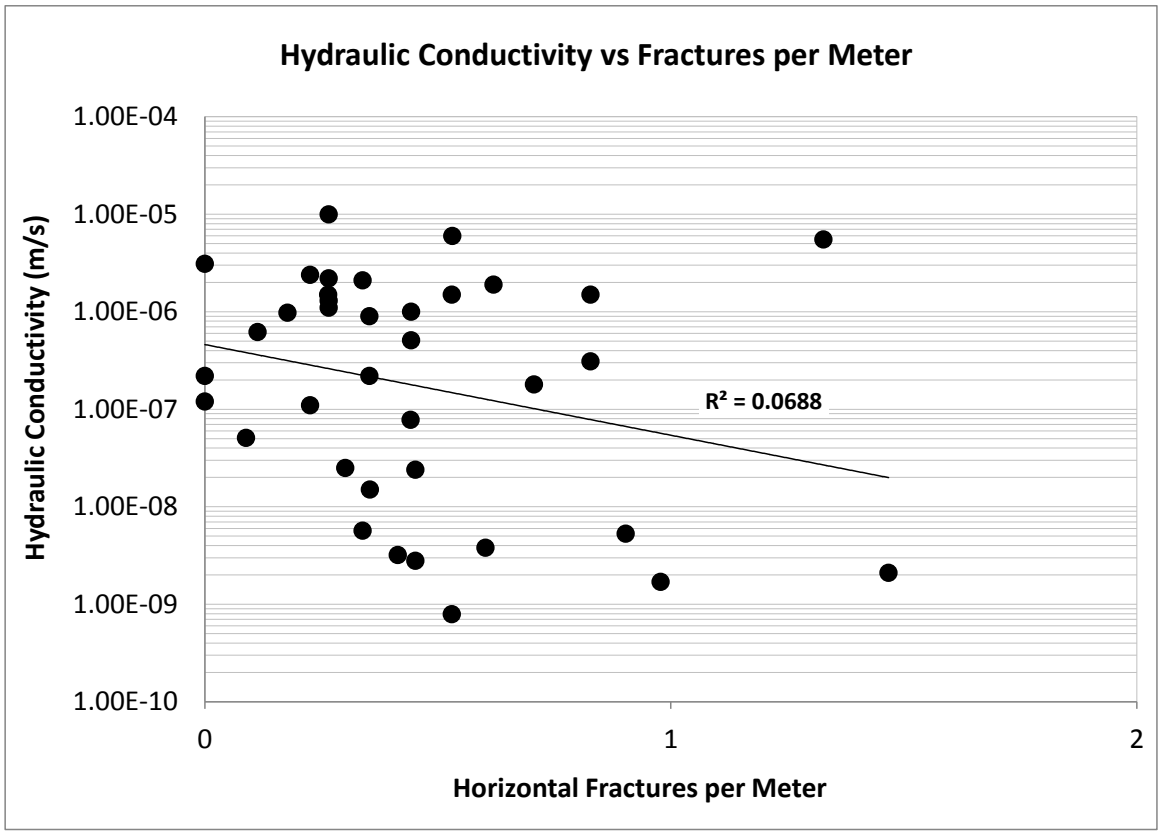

Figure 3.15 - Horizontal fractures versus hydraulic conductivity, MC-316

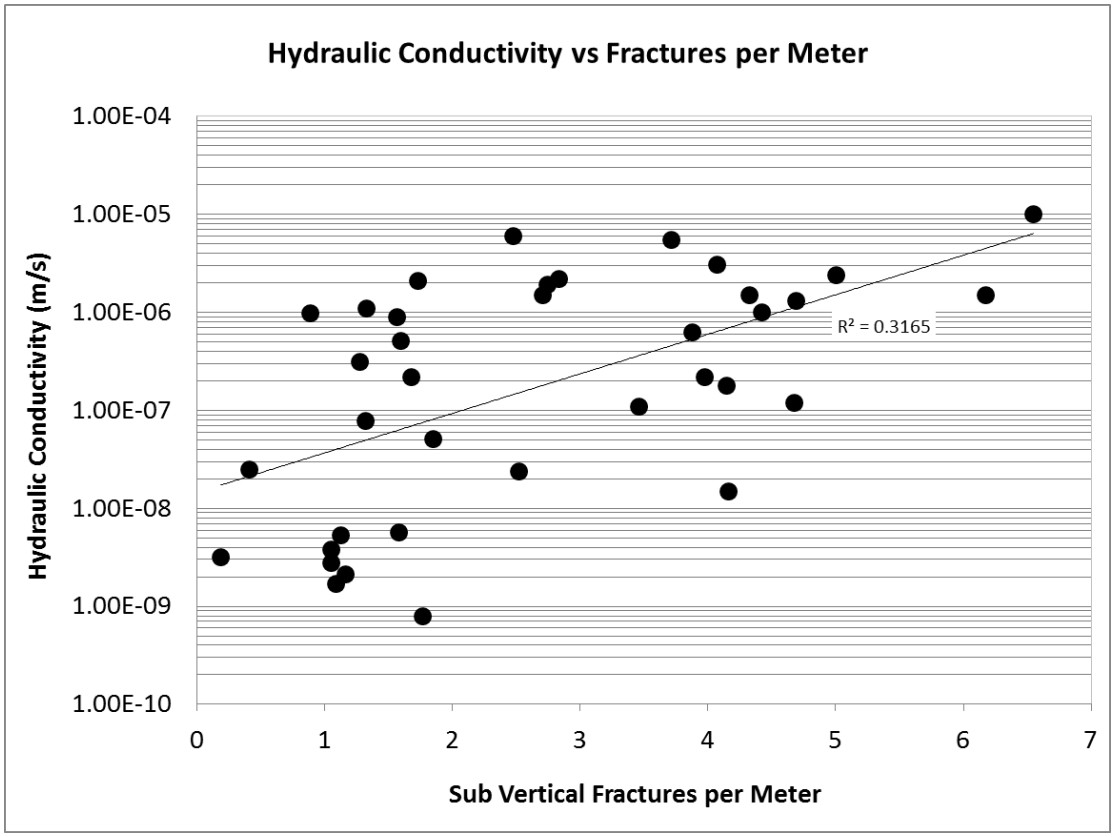

Figure 3.16 - Sub-vertical fractures versus hydraulic conductivity, MC-316

Additional data on the condition/properties of sub-vertical fractures may also provide indications of elevated hydraulic conductivity. Oxidization in the form of iron staining is a strong indication of flow. As water flows through a fracture, iron may be oxidized. Generally, the more water the more staining. Infilling generally occurs when minerals precipitate out of water in the fractures. Fractures can be completely healed if the infilling fills the fracture. In this study, healed fractures were not classified as fractures as they have no contribution to flow. Partial infilling can indicate the fracture is still flowing.

To assess the effects of staining, the number of sub vertical fracture with staining per 5 m interval was graphed against depth (see Figure 3.17). This figure also shows the number of joints with quartz crystals per 5 m interval. Fractures with quartz crystals tend to appear when there is an increase in hydraulic conductivity. Sub-vertical fractures with staining and quartz crystals appear in two concentrations that coincide with two of the spikes in hydraulic conductivity at approximately 150 m and 400 m depth. Large quartz crystals (>1 mm) in fractures indicate that apertures must be large and likely result in a larger hydraulic conductivity. The two indicators are the result of very different processes but both may indicate a current state of elevated hydraulic conductivity.

The intervals possessing the most prominent quartz crystal growth (see Figures 3.8 and 3.9) coincides with a high hydraulic conductivity interval from 397 m to 419 m in depth. To investigate the relationship of these quartz crystals to the quartz-rich matrix, a thin section was cut normal to the fracture surface. In Figure 3.18, the quartz crystals within the fracture can be seen on the right side of the section. It is evident, based on crystal size and texture, that the quartz near the right edge of the image grew subsequent to the creation of a large-aperture fracture. Observation of the core on a larger scale (e.g., see Figures 3.8 and 3.9) indicates that this large-aperture fracture is only fully occluded by quartz crystals in localized areas. This suggests that its hydraulic conductivity should be very high where it is partially or fully lacking quartz crystals.

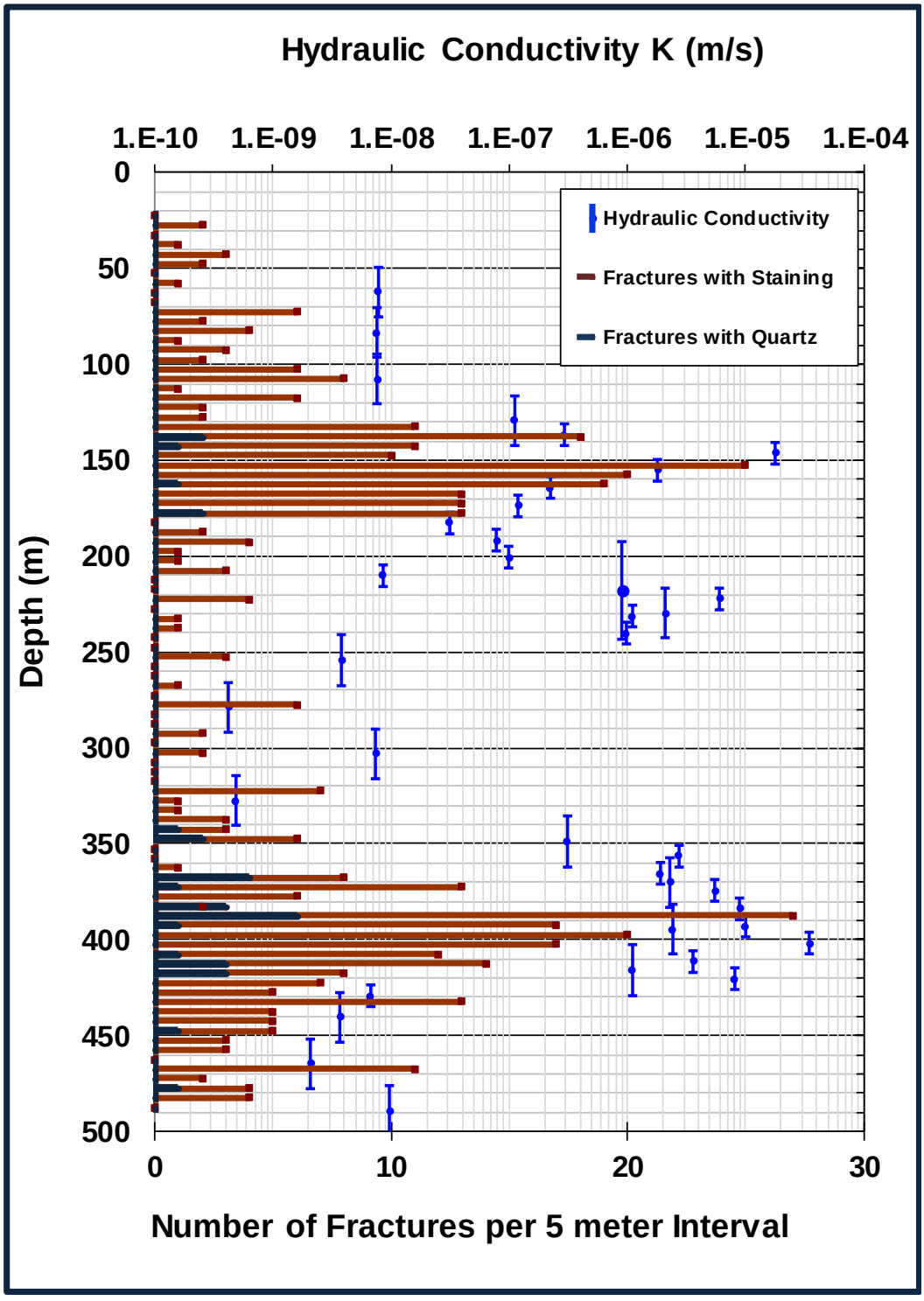

Figure 3.17 - Number of sub-vertical fractures with staining or quartz crystals per 5 m interval, MC-316

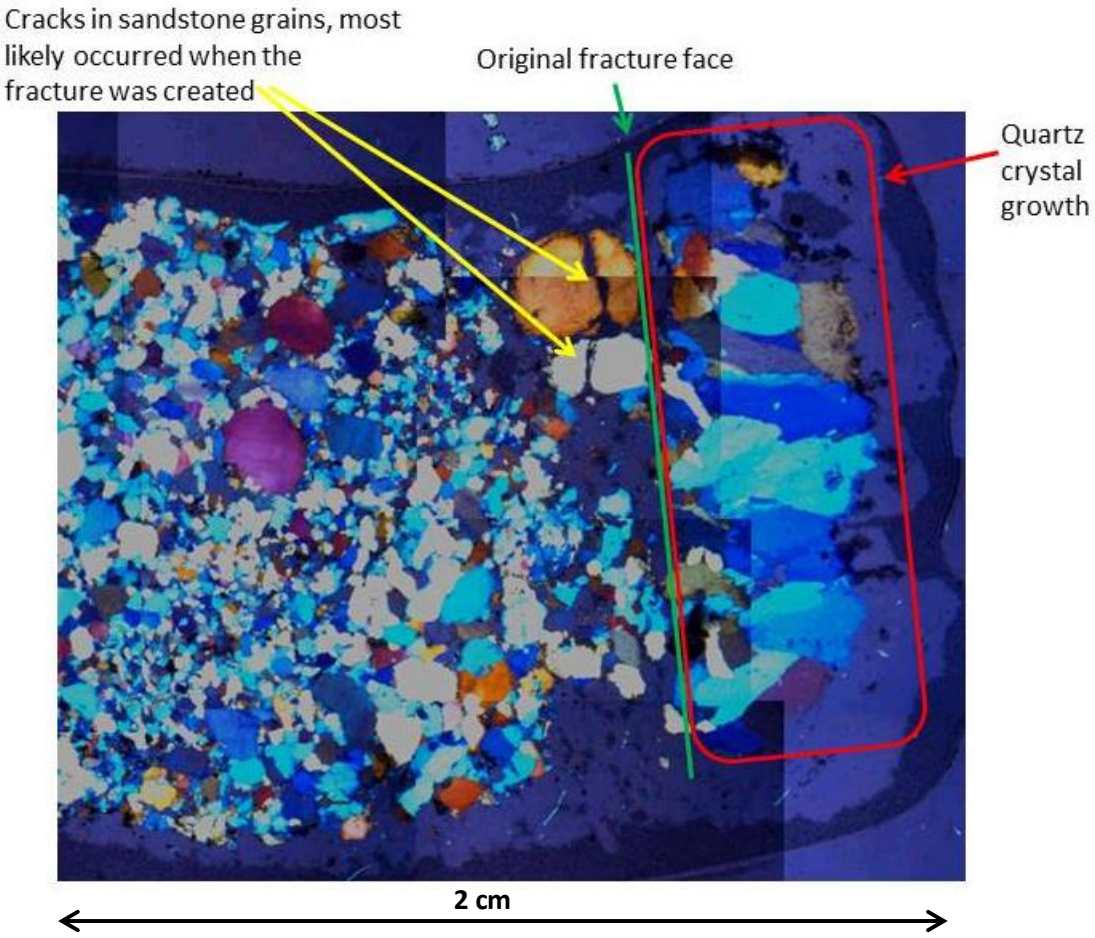

Figure 3.18 - This section on quartz-lined fracture, MC-316

Isolated features may be responsible for a large portion of local flow. When logging core, close attention should be given to sub-vertical fractures that are continuous with heavy staining. Figure 3.19 shows a set of sub-vertical fractures found at a depth of 214 m. The fractures highlighted are likely the cause of the high hydraulic conductivity interval that was not identified based on the fracture – hydraulic conductivity relationships shown in Figures 3.16 and 3.17.

Figure 3.19 - A discrete feature found at a depth of 218 m, MC-316

3.3 ANALYSIS OF BOREHOLE SP-001

To extend the findings extracted from the study of borehole MC-316, a subsequent shaft pilot borehole (SP-001) was examined on Oct 20, 2010. The same investigation techniques described for MC-316 were used on SP-001. The core had been logged by SRK in detail in advance of this author's site visit. Review of these logs conducted as part of this research project led the author to the conclusion that the logging had been well executed and that reporting was clear and comprehensive. It should be noted that packer testing intervals for SP-001 were 30-50 m whereas MC-316 was tested at intervals of 10 to 30 m, hence vertical resolution is lower and average effects ("smearing") are more pronounced for SP-001. Given SRK's log as a sound and reliable starting point, the author focused on features most likely to be associated with high inflow potential. Hydraulic conductivity values provided by SRK (see Figure 3.20) were used as a benchmark when analyzing core.

Quartz crystals were observed in several joints in the SP-001 cores. In many cases the crystals appear to have grown from opposing faces of a fracture, with well-formed euhedral crystals occurring on both faces. This suggests significant "openness" of the fracture. . Examples of these can be seen in figures 3.21 to 3.23.

Similar to borehole MC-316, the fractures with quartz crystals in SP-001 were generally observed to coincide with zones of elevated hydraulic conductivity. At 128.3 m, partially open fractures were observed with quartz lining the joint faces. At roughly 150 m depth, similar fractures were observed, as shown in Figure 3.21. At 194.5 m – 195 m and 197.2 m - 198.8 m, open fractures were observed with crystal sizes typically 1 - 2 mm.

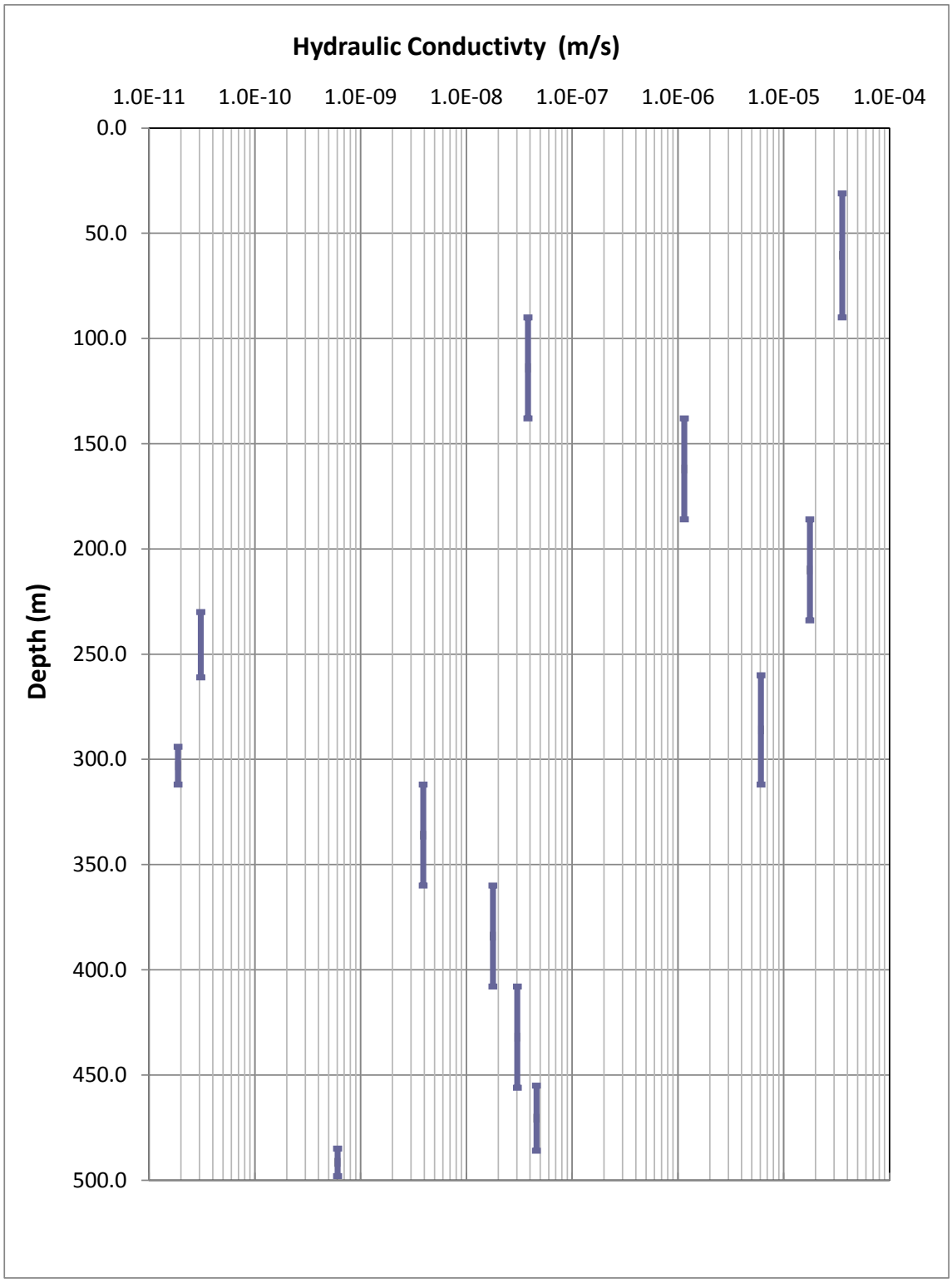

Figure 3.20 - Hydraulic conductivities measured by packer testing of borehole SP-001

Figure 3.21 - Crystals present in an open joint at 197.3 m depth, SP-001

Figure 3.22 - View of joint openness, 197.3 m depth, SP-001

Figure 3.23 - Quartz-lined open joint at 150 m depth, SP-001

Results from analysis of core logging data for borehole SP-001 are shown in Figures 3.24 through 3.27. The total number of fractures seen was lower than MC-316. This may be partially due to the triple tube coring process that was used for SP-001. The coring technique minimizes drill induced damage resulting in fewer fractures. On MC-316, obvious drill induced fractures were dismissed, however as the author later discovered, some drill induced fractures on micro defects with staining were most likely included. On SP-001, many cracks, micro defects and partial fractures were closed (see Figure 3.28). These closed fractures were not counted in this analysis, but because of a difference in drilling techniques the same features most likely would have been assessed as fractures on MC-316. This presents an error in comparing the two boreholes, primarily due to drilling techniques and assessing the core compared to its in-situ condition.

Due to the lower number of fractures on SP-001, a poorer sample size was available for plotting. Analysis methods from MC-316 still apply on SP-001; however, more attention needs to be paid to specific fractures rather than a density of fractures. Sub-vertical fractures with staining were encountered in every zone of larger hydraulic conductivity. This observation generally agrees with conclusions drawn from MC-316.

Quartz lined crystals appeared in the highest hydraulic conductivity intervals, most likely due to their larger apertures. Both staining and the presence of quartz can correspond to a higher hydraulic conductivity.

Quartz crystals and iron staining are believed to derive from separate origins. The staining observed on the fractures resulted from oxidization reactions that occurred when meteoric water, which is oxygen rich, reacted with iron in the sandstone. Quartz crystal growth resulted from hydrothermal processes, which implies that the quartz crystals originated when the sandstone was more deeply buried, hence at an earlier time than the staining.

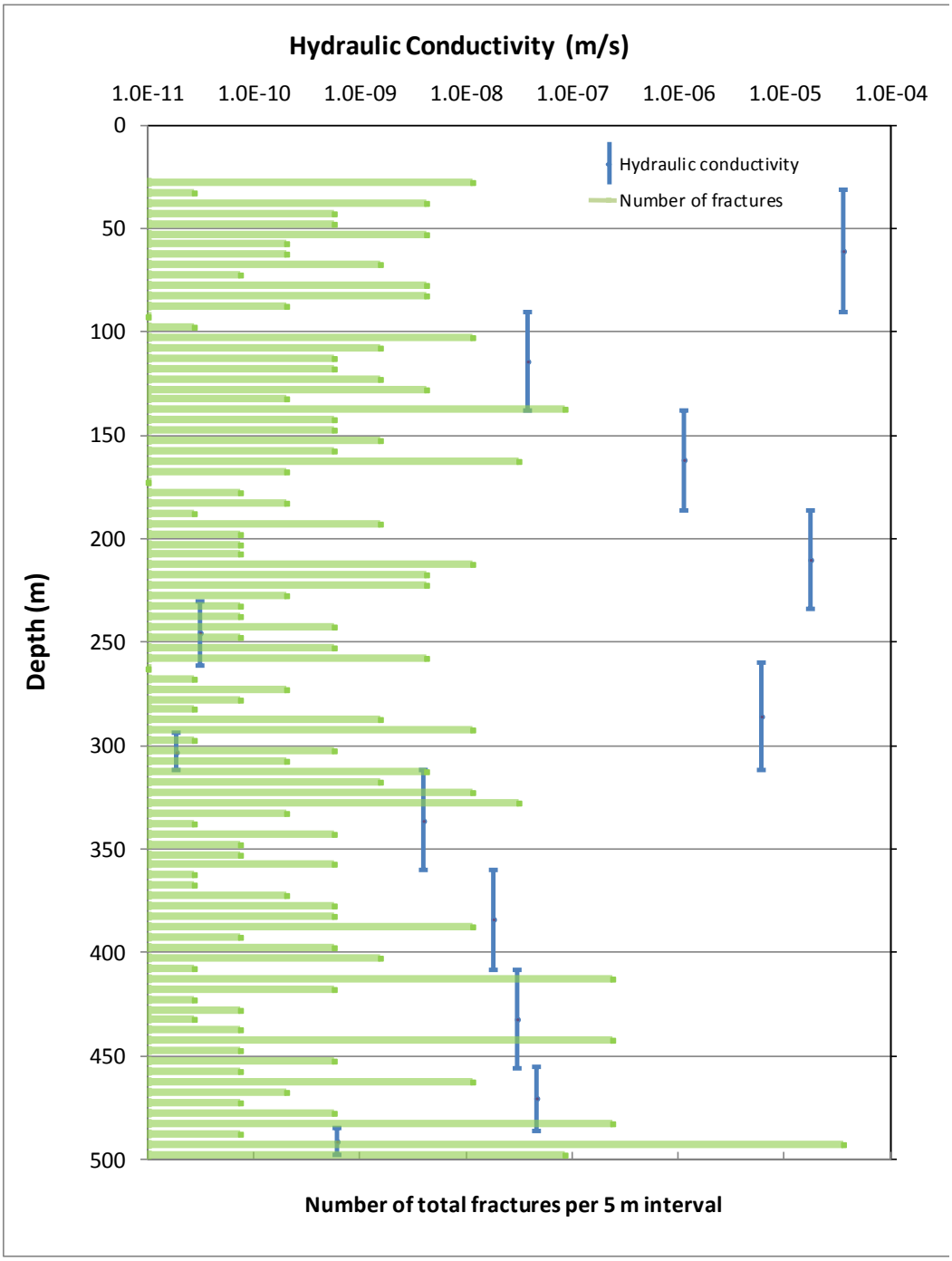

Figure 3.24 - Total fractures per 5 m interval and hydraulic conductivity versus depth, SP-001

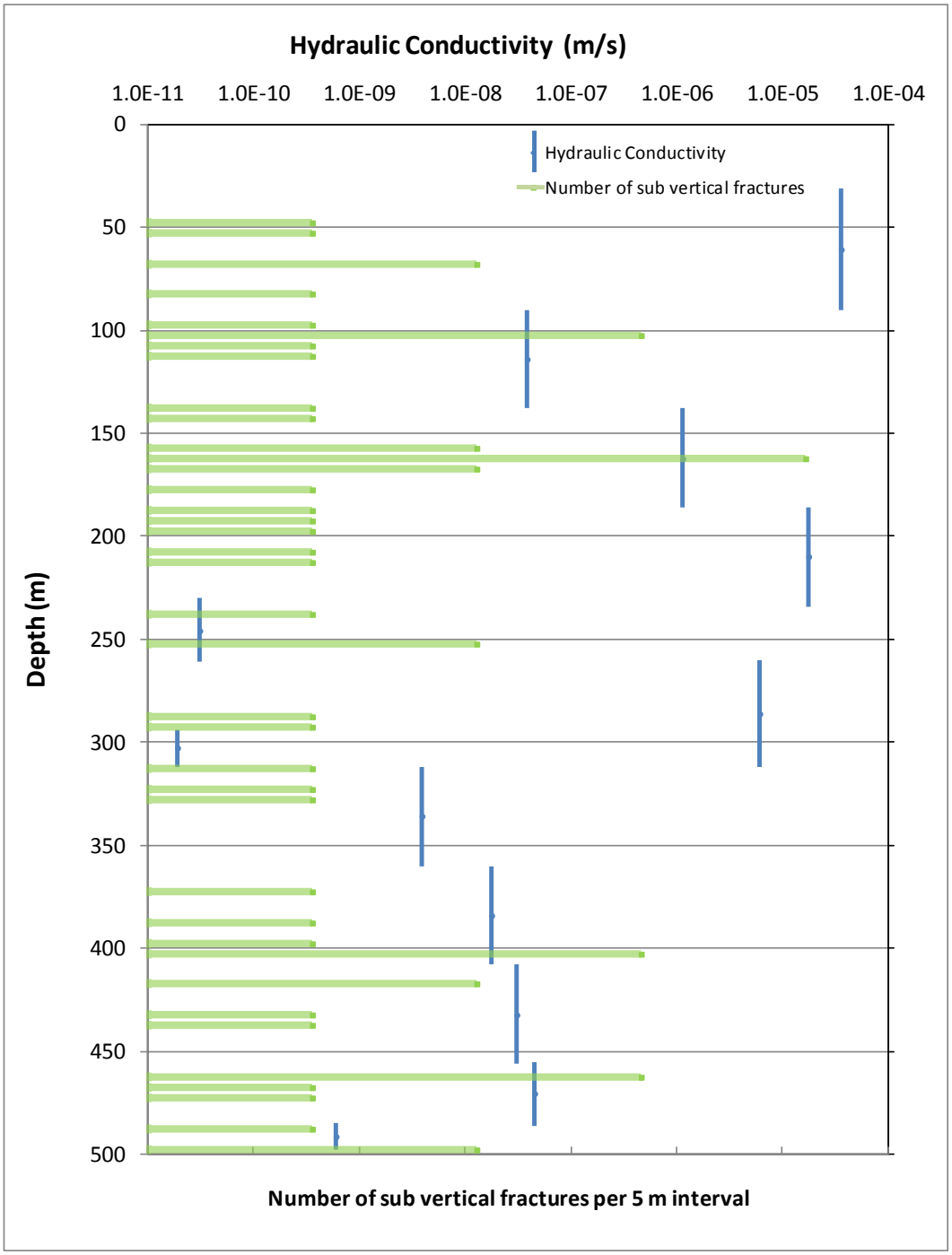

Figure 3.25 – Sub-vertical fractures per 5 m interval and hydraulic conductivity vs Depth, SP-001.

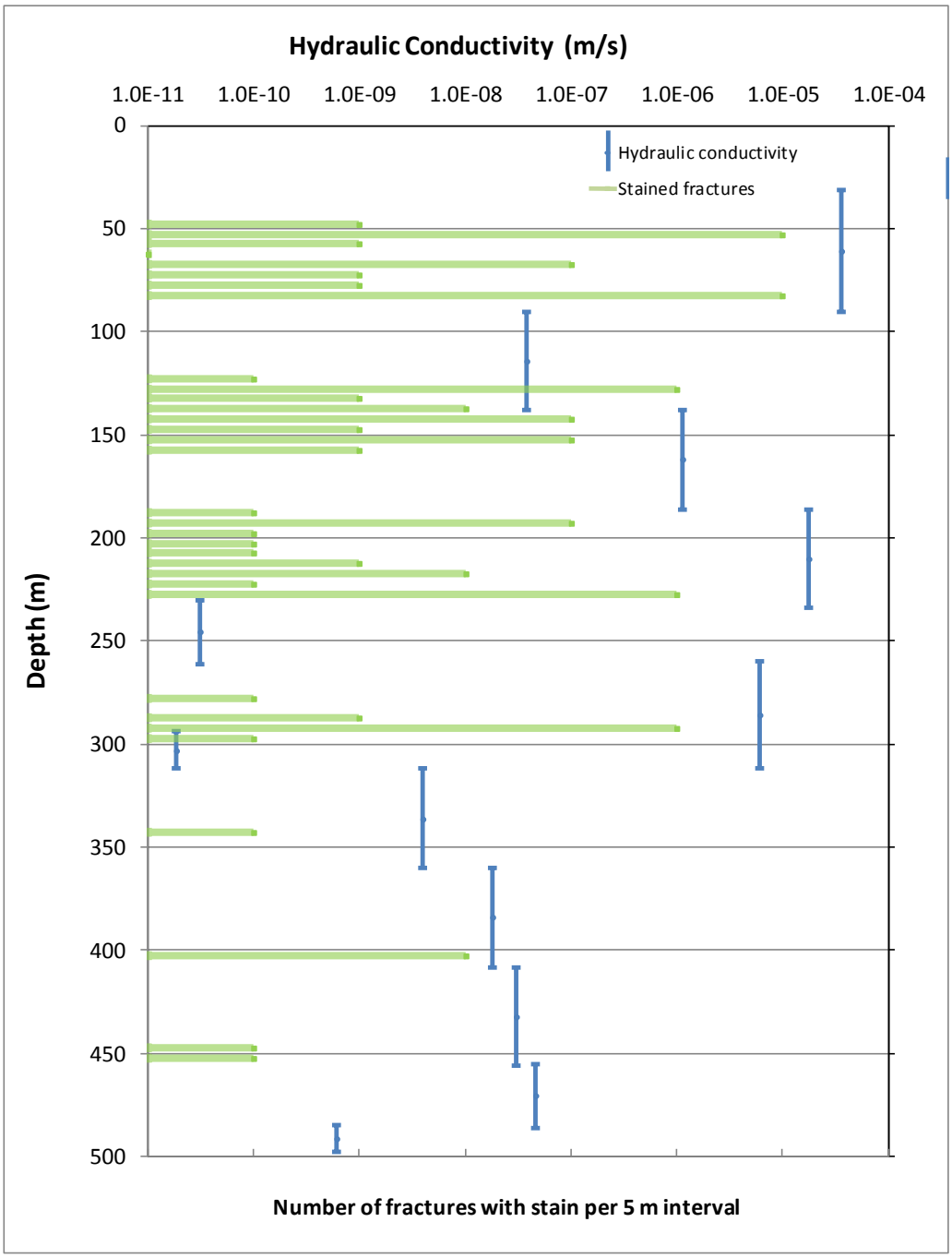

Figure 3.26 - Total fractures with stain per 5 m interval and hydraulic conductivity versus depth, SP-001

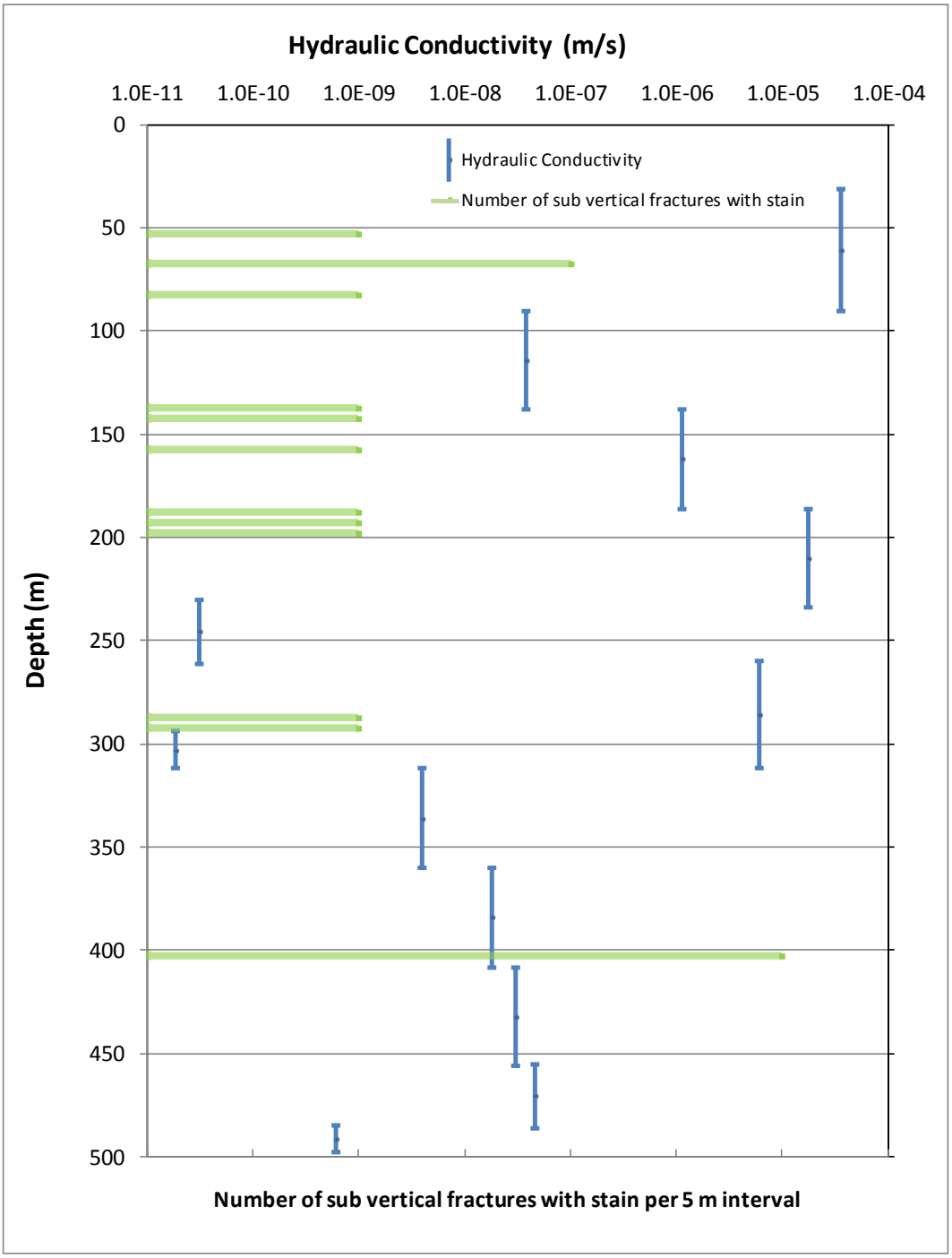

Figure 3.27 – Sub vertical fractures with stain per 5 m interval and hydraulic conductivity vs Depth, SP-001.

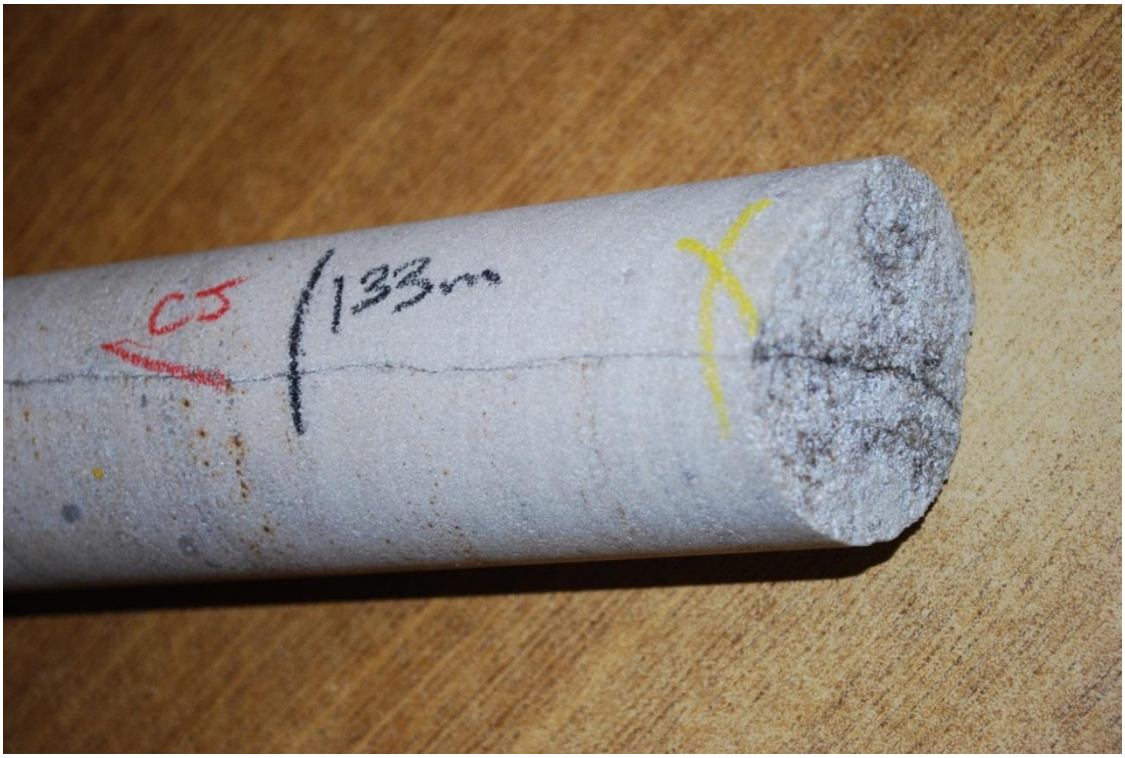

Figure 3.28 - Closed stained fracture in core, SP-001

3.4 SUMMARY

General trends in rock mass hydraulic conductivity can be obtained from core logging. Staining of sub-vertical fractures and the presence of quartz generally indicate a high hydraulic conductivity. Fractures that appear to have larger apertures may also be indicative of a larger flow potential. Basic logging can yield important data that can be cheaply and efficiently collected. Such data can help identify intervals of high inflow potential, but not as a predictive tool; packer testing remains the most confident method of identifying such intervals

CHAPTER 4 LABORATORY TESTING

4.1 INTRODUCTION

Core samples were collected during the site visits mentioned in Chapter 3 and shipped to the University of Saskatchewan Rock Mechanics Laboratory for further analysis. Laboratory testing was conducted to assess the hydraulic conductivity of the fractures and matrix in a controlled environment. The majority of the testing focused on the hydraulic conductivity of fractures. A test was designed in a triaxial cell to measure the hydraulic conductivity of core containing sub-vertical natural fractures while mimicking in-situ conditions. Fracture closure was measured to investigate the relationship between stress, aperture, and hydraulic conductivity.

4.2 MATRIX TESTING

Analysis of intact rock matrix properties was conducted on four 25 mm diameter core samples that were extracted from larger intact samples. The porosities of these samples were measured by the gravimetric method (i.e., based on a comparison of dry mass and water-saturated mass). Matrix hydraulic conductivities were measured at nominal confining pressure (< 100 kPa) using a Ruska Liquid Permeameter. Table 4.1 displays the results of these measurements.

Table 4.1 – Matrix hydraulic conductivity and porosity values from borehole MC-316

Depth of Sample (m)	**Porosity (%)**	**Hydraulic Conductivity (m/s)**
306.6	**7.7**	**3.18×10^{-10}**
335.4	**8.5**	**1.03×10^{-10}**
377.1	**6.4**	**2.8×10^{-11}**
377.2	**3.0**	**1.89×10^{-11}**

Dynamic elastic properties were determined on the same four samples using the pulse velocities of compressional (p) and shear (s) waves. The tests were conducted and analyzed as outlined in ASTM D2845 – 08 (ASTM, 2008). The results are listed in Table 4.2.

Table 4.2 – Dynamic elastic properties of intact samples

Depth of Sample (m)	**Bulk Density (kg/m^3)**	**Young's Modulus (GPa)**	**Poisson's Ratio**
306.6	2427	56.7	0.17
335.4	2403	47.0	0.23
377.1	2381	62.0	0.18
377.2	2550	66.6	0.18

4.3 FRACTURE TESTING

4.3.1 *Sample Selection*

Of the core samples brought to the Rock Mechanics Laboratory for further analyses, six fractured samples were ultimately selected for hydraulic conductivity testing. The first sample was a trial run using new testing equipment and procedures, complications were encountered so no further analysis was done on this sample.

Table 4.3 presents a summary of the six samples used for fracture testing; photographs of these samples are shown in Figures 4.1 through 4.6. The samples all contained fractures that day-lighted on both ends. Fractures with a variety of attributes (notably staining and quartz infilling) were selected, to assess the variability of hydraulic conductivity as a function of these attributes. Three of the five samples analyzed in detail were fully parted along the fracture plane when they were found in the core box. Though the fracture surfaces did not contain any obvious signs of coring and handling-related damage, it is possible that the mating of their surfaces during the lab testing was not identical to in-situ conditions. Two of the samples, though containing a through-going fracture, were mated (i.e., closed and intact) when found in their core boxes, and remained mated throughout sample preparation and testing. As such, it is felt that the mating of these fractures during the lab testing should match in-situ conditions. Joint Roughness Coefficient (JRC) values were found by scanning the surface of the fractures using a laser profilometer and assigning a value to the resulting trace. Regrettably the mated samples were not scanned prior to aperture testing (see section 4.7) which rendered surface scanning impossible. The four available fracture scans are displayed in Figure 4.7. JRC was determined from the amplitude of the fracture profile using equation [2.2]. Amplitude was measured as the total difference in height from the highest point to the lowest point occurring over the 10 cm section. Micro roughness r_a was also measured from the fracture profile and is determined as the largest change in amplitude over a 5 mm span on any interval of the scan. In Figure 4.7, the location of the r_a calculation is marked with a green square.

Table 4.3 – List of fractured samples tested in this work

Sample No.	Hole	Depth (m)	Description	JRC Values	Micro Roughness (mm)	Separated on fracture surface?
1	MC-316	301.77 - 302.32	Clean	13	0.97	yes
2	MC-316	335.44 – 335.76	Medium stain	13	1.00	yes
3	SP-001	132.8 – 133.1	Heavy stain			no
4	SP-001	150.0 – 150.3	Partially quartz-filled			no
5	MC-316	306.60 – 306.87	Medium stain, loose sand grains	18	1.26	yes
6	SP-001	288.7 – 289.0	Very heavy stain	15	1.63	yes

Figure 4.1 - Photograph of sample 1 (test run)

Figure 4.2 - Photograph of sample 2 (medium stain)


Figure 4.3 - Photograph of sample 3 (which was observed to have heavy iron-staining after testing, when the sample was pulled apart)


Figure 4.4 - Photograph of sample 4 (partially quartz-filled)

Figure 4.5 - Photograph of sample 5 (medium stain, lose sand grains)

Figure 4.6 - Photograph of sample 6, prior to cutting ends square for testing (heavy stain)

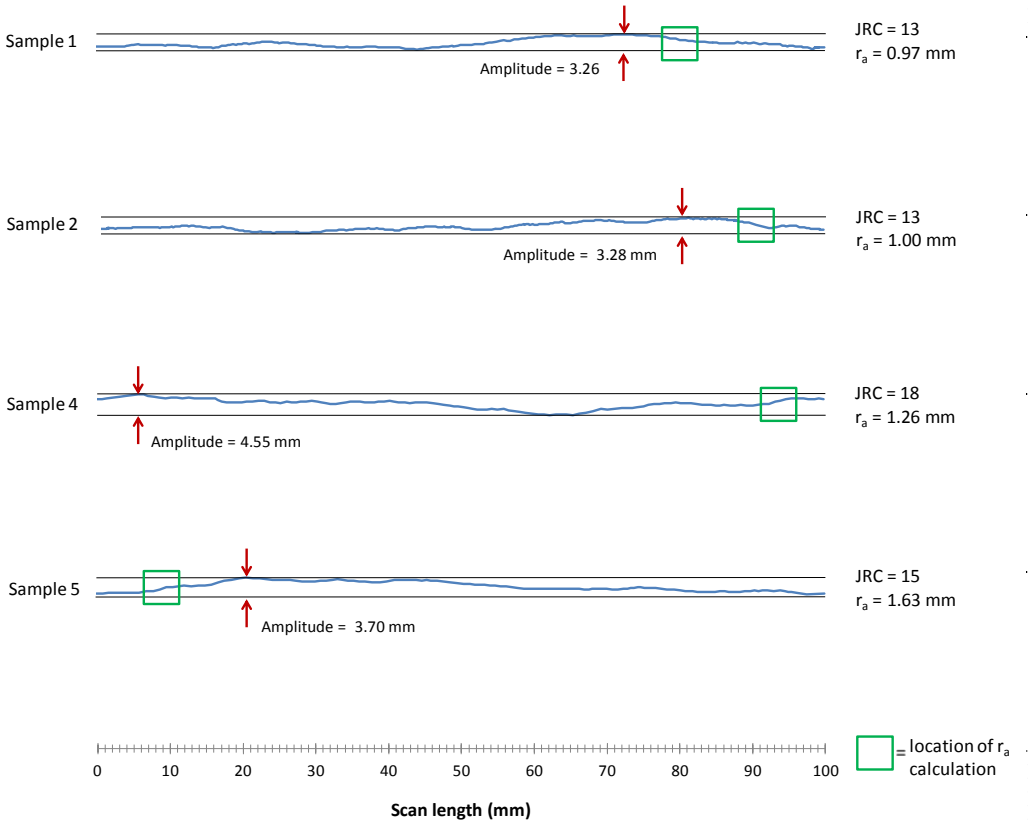

Figure 4.7 - Fracture scan lines from lab samples. JRC values are determined by the maximum peak-to-trough amplitude over the 10 cm scan. r_a is the largest change in amplitude is any 5 mm section of the 10 cm scan

4.4 TESTING PROCEDURES

The diameters of the samples tested were 63 mm (± 1 mm), and the lengths (after cutting) varied from 97 to 146 mm. The ends of the samples were cut at a length greater than 1.5 times the diameter of the sample. The cut samples were saturated in distilled water for a period of 48 hours or more. Once saturated, each sample was sandwiched between a pair of porous stainless steel disks (1 cm thick, each), which distributed pore fluid over the surface of each sample end. A heat shrinkable Teflon jacket was used to enclose each sample and the porous disks at its ends. With the jacket and platens in place, the sample was saturated again for a period greater than twelve hours. A layer of elastomer (Skinflex) was set around each end of the Teflon jacket using a purpose-built mold, sealing the sample, porous plates, platens, and jacket in place. Figure 4.8 displays a picture of the Skinflex setting in a mold around the sample. Loading platens each contained a single pore fluid port near the platen center (to supply or collect fluid). Pore fluid was injected through the top platen into the porous plate and distributed into the sample. At the bottom of the sample the fluid was gathered through the porous plate into a collection port on the other platen.

A strain chain was placed around the middle of the sample. The chain was used to measure circumferential displacement, which was ultimately used to estimate fracture closure (change in aperture) during testing. Figure 4.9 shows sample 2, fully prepped for the cell.

Once the sample was connected, the lines were vacuumed to remove all air from the system. The cell was then sealed and filled with oil. The oil pressure was controlled using a syringe pump and a transducer within the cell. The sample was pressured to simulate in-situ pressures of the rock while measuring fracture closure with the strain chain.

A syringe pump was used to supply a constant flow rate of water to one end of the sample. The other end of the sample was vented to atmosphere. The flow rate at the outlet pipe was measured and compared against the input flow rate, to confirm that steady-state flow conditions were reached. The pressure at the inlet end of the sample was measured with a transducer. To correct for pressure drop within the apparatus, a test was conducted with no sample (i.e., two porous disks sandwiched between platens), and pressure drop as a function of injection rate was measured. The collected data was then corrected for this systematic error in the apparatus.

During initial trial testing for sample 1, the jacket ruptured at high confining pressure at a point adjacent to an open fracture segment where there were relatively sharp edges. In the final five tests, two layers of Teflon heat shrink were used to jacket the sample and mitigate the potential for leakage of hydraulic oil from the cell into the sample. Sample six had a relatively large aperture which was covered by thin tin plates to avoid rupture.

Near the end of the test on sample 2, pressure within the sample began to increase, unexpectedly. It was discovered that the oil used to pressurize the sample had penetrated between the interface of the Skinflex and the Teflon jacket. In the subsequent four tests, hose clamps were installed and tightened around the Skinflex at the Skinflex-Teflon interface, and a bead of silicone sealant that was applied at this interface.

Figure 4.8 - Skinflex setting in a mold around a fractured core

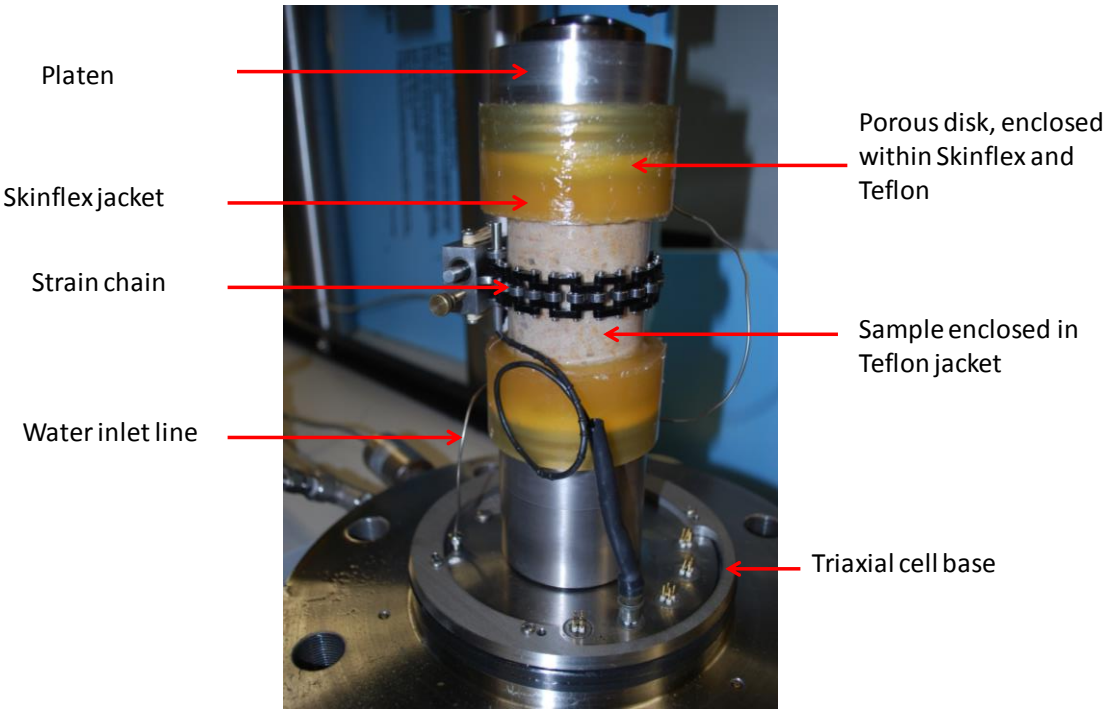

Figure 4.9 - A fully jacketed and instrumental fracture core sample prior to testing. Note hose clamps, not shown here, were placed around the innermost edge of each Skinflex jacket for samples 3 through 6.

The equivalent hydraulic conductivity (K_{eq}) was calculated for each sample tested. K_{eq} was calculated using the corrected pressure drop across the sample, the specified flow rate, and the cross sectional-area and length of the sample. The assumption that the relationship between flow rate and pressure was controlled by Darcy's law was made. See section 4.10 for an assessment of flow conditions.

The term equivalent hydraulic conductivity is used here to denote the hydraulic conductivity that an intact sample of the same size would possess in order to flow at the same rate at the pressure drop that was measured during the test (i.e., the matrix permeability of an equivalent continuum). The equivalent hydraulic conductivities presented in this chapter may be regarded as the hydraulic conductivity per meter squared of cross-sectional area, for an impermeable matrix containing a fracture trace length (in the cross-sectional plane) of approximately 20 m (based on a fracture trace length of roughly 60 mm for each of the samples tested, with a cross-sectional area of roughly 3000 mm^2 each). Assuming parallel, equally-spaced fractures oriented normal to a cross-sectional plane of rock mass that is 1 m by 1 m, this would correspond to a fracture spacing of 50 mm. As shown in Chapter 5, proper scaling of the conductivities measured on these samples to field conditions can be done, if an appropriate fracture spacing for a rock mass is known (or assumed).

The goal of the fracture testing was to measure hydraulic conductivities as a function of effective confining pressure. A range extending up to the maximum value of mean effective in-situ stress for the study site (estimated to be between 6000 and 7000 kPa) was used. It was desired to measure hydraulic conductivities as effective confining pressures were cyclically increased then decreased, to assess if hysteresis is observed. In some cases, it was not possible to achieve the targeted number of load cycles due to test failure (e.g., jacket leakage) or time constraints (e.g., long testing times required for low hydraulic conductivity samples). For the final test (sample 6), the final cycle was conducted to a significantly higher effective confining pressure (18000 kPa) in order to assess the limits of the testing system.

4.5 FRACTURE TESTING RESULTS

Figures 4.10 through 4.14 show the equivalent hydraulic conductivities (K_{eq}) measured as a function of effective confining pressure (P_c') for samples 2 through 6. With the exception of sample 4, the K_{eq} values measured are orders of magnitude greater than the values measured on intact samples. This suggests that fracture flow is the dominant transport mechanism in samples 2, 3, 5 and 6. As expected, K_{eq} for the fractured samples decreased with increasing confinement. In all cases, K_{eq} measured at maximum P_c' was more than an order of magnitude smaller than the initial value, which was measured at low P_c'. For the samples that were subjected to two or more loading cycles (i.e., samples 2, 3, 5 and 6), hysteresis was observed; i.e., K_{eq} was less sensitive to P_c' upon initial unloading from the maximum P_c' value reached at a given stage in a testing sequence. Upon re-loading, the form of the $K_{eq} - P_c$' curve was generally similar to the unloading curve. It is suggested that the behaviour observed during unloading is likely more representative of in-situ behavior, given that the behavior observed during initial loading is affected by the reversal of aperture increase that occurred during coring and sample handling.

For samples 2 through 5, which were loaded to a maximum P_c' less than 9000 kPa, the general form of the $K_{eq} - P_c$' curves is concave upwards. For sample 6, which was loaded to a maximum P_c' of 18000 kPa, a more complex behavior was observed, with more of a concave-downwards form during loading to progressively higher P_c' values. This behavior is suggestive of the type of response expected for a porous medium that is being loaded above its pre-consolidation stress level.

To provide a consistent basis for comparing K_{eq} values amongst all of the samples, the value measured upon reaching a P_c' value between 6000 and 7000 kPa, for the first loading sequence, was recorded and plotted in Figure 4.15. Of these samples, K_{eq} of the sample with the heaviest staining (sample 6; 2.3×10^{-6} m/s) was significantly greater than the samples with medium staining (samples 2 and 5; 9.9×10^{-8} and 1.3×10^{-7} m/s, respectively).

The only sample tested with partial infilling of quartz (sample 3) had the lowest K_{eq} value. This is not viewed as a representative result on the whole. Based on core logging and packer testing of these boreholes, partial infilling with quartz crystals is believed to be an indicator of potentially high hydraulic conductivity. Once the core of sample 3 was open is was observed that the fracture was not continuous, hence flow through the matrix would have occurred. This was qualitatively confirmed by the core inspection conducted during this project, given that partially quartz-filled fractures were observed with apertures locally in the vicinity of 2-10 mm. These fractures were noted to correspond to high-conductivity zones identified in the packer tests. These samples were deemed unsuitable for laboratory testing, however, partly due to the assessment that these fracture surfaces had been mechanically damaged during coring and handling, and partly because the hydraulic conductivities measured at the core scale would likely have been too high to measure.

Samples 3 and 4 were both partially cemented when tested. Both of the samples were separated after the lab testing was completed. Sample 3 showed moderate to heavy staining which suggests that it had experienced significant flow in-situ.

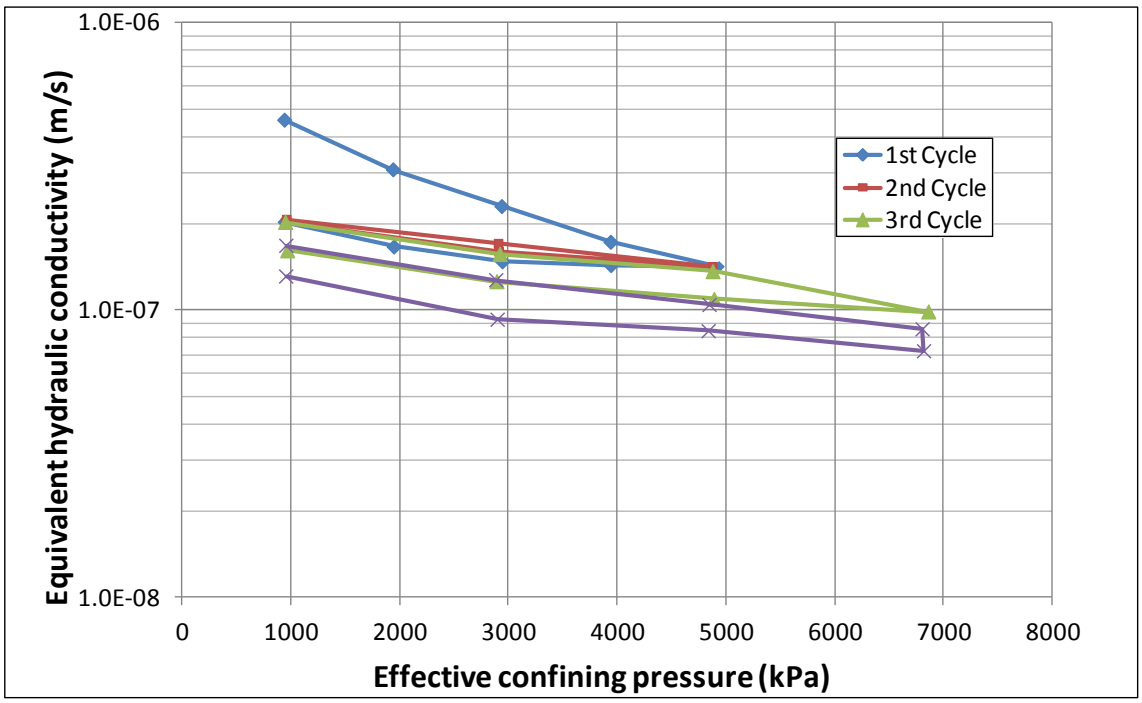

Figure 4.10 - Equivalent hydraulic conductivity as a function of effective confining pressure, sample 2

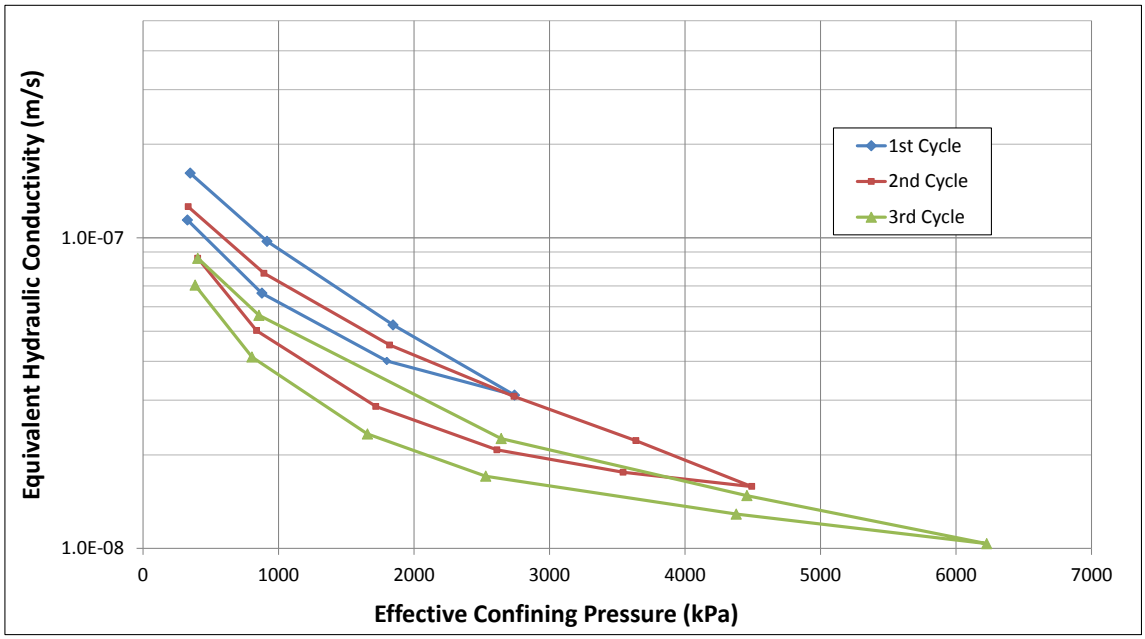

Figure 4.11 - Equivalent hydraulic conductivity as a function of effective confining pressure, sample 3

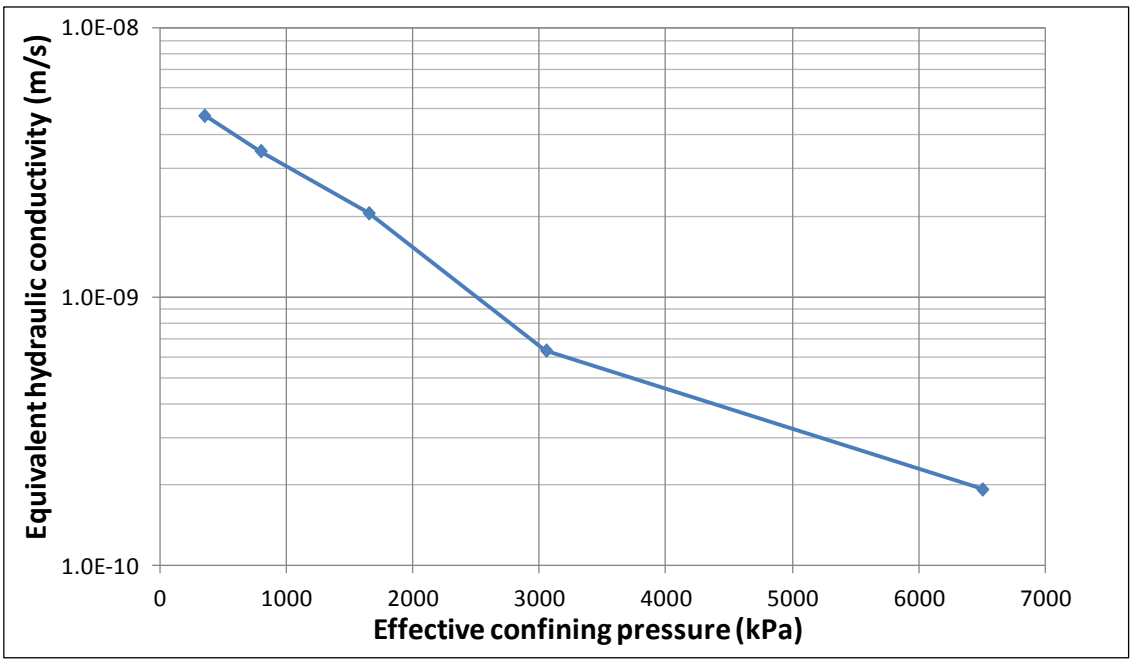

Figure 4.12 - Equivalent hydraulic conductivity as a function of effective confining pressure, sample 4

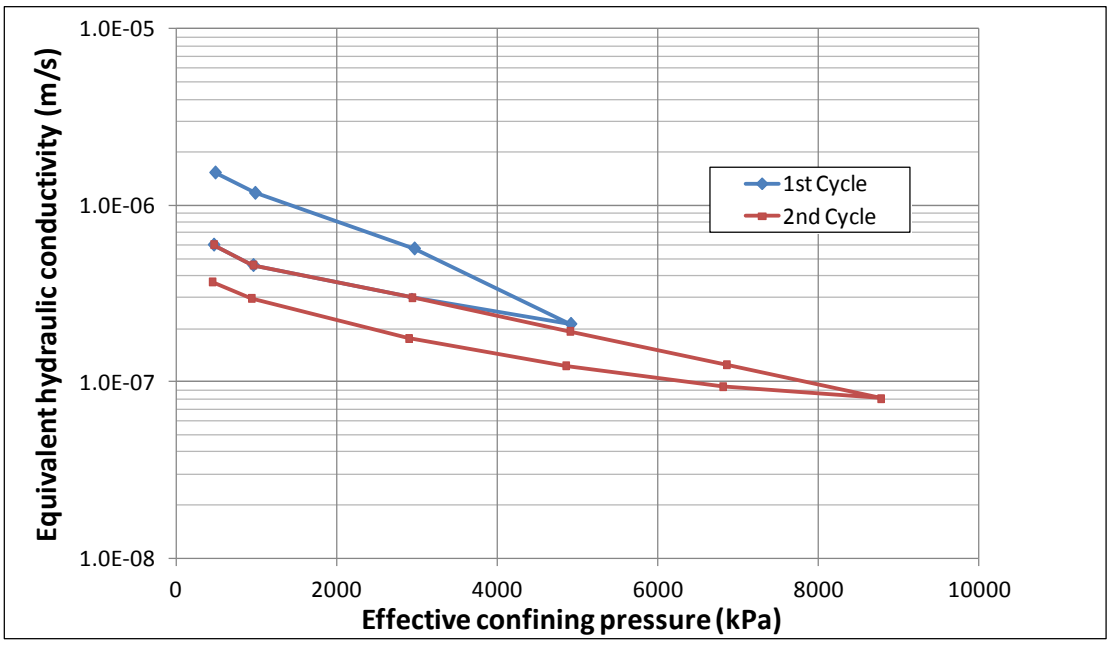

Figure 4.13 - Equivalent hydraulic conductivity as a function of effective confining pressure, sample 5

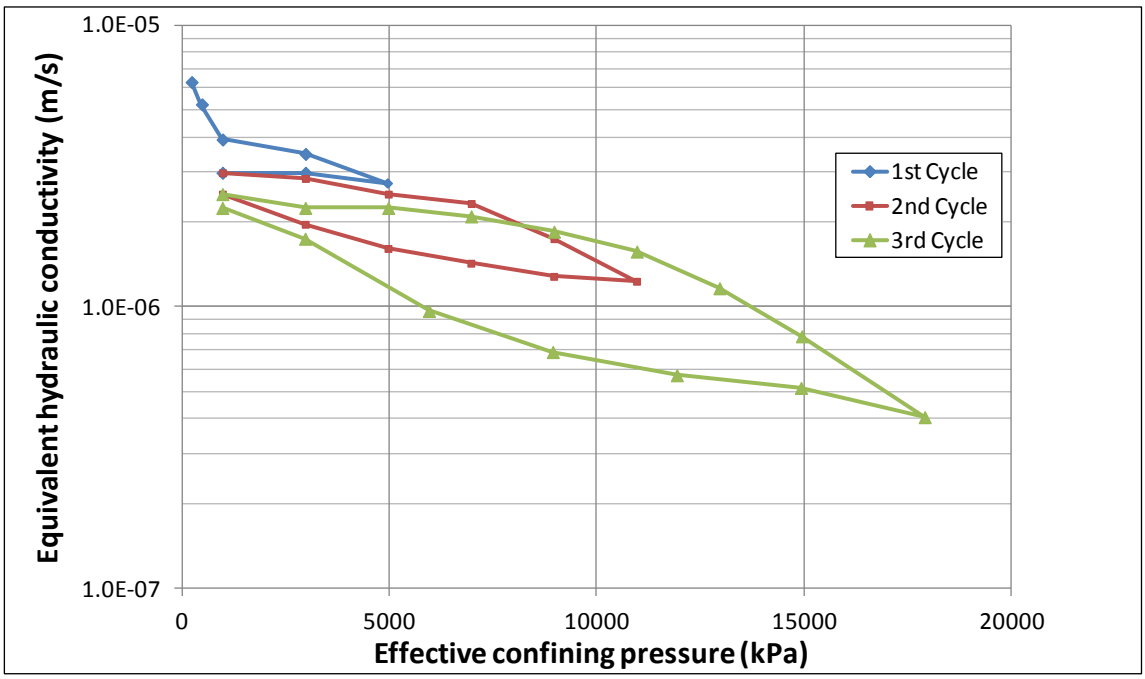

Figure 4.14 - Equivalent hydraulic conductivity as a function of effective confining pressure, sample 6

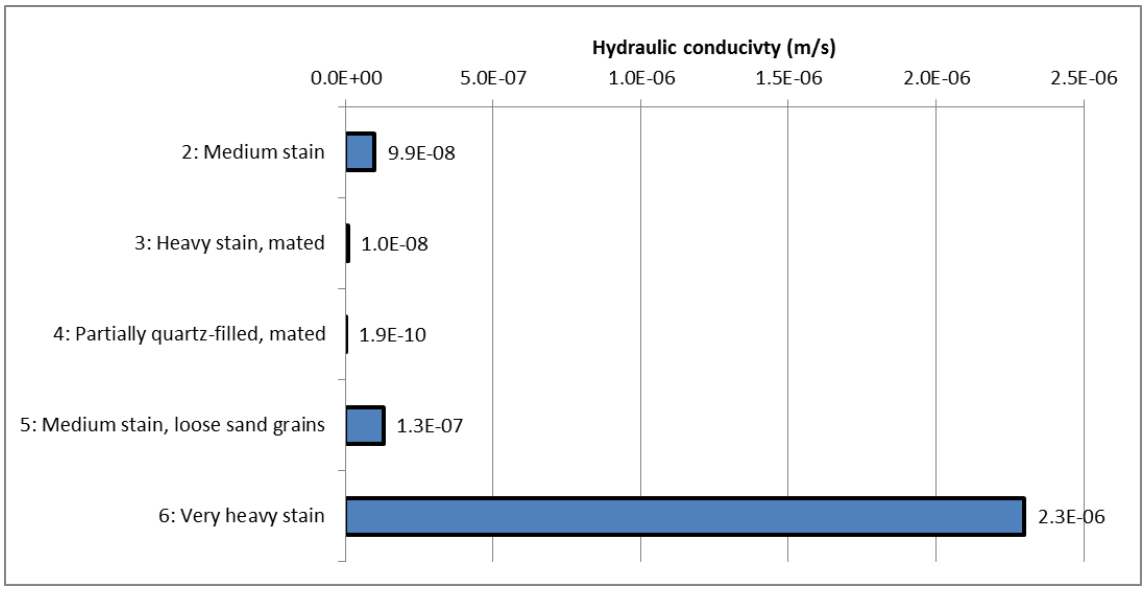

Figure 4.15 - Equivalent hydraulic conductivity for each fractured sample, measured upon reaching an effective confining pressure between 6000 and 7000 kPa for the first time

4.6 MEASUREMENT OF FRACTURE CLOSURE

This section describes the procedures used to analyze the change in mechanical fracture aperture as a function of effective confining pressure to enable an assessment of the relationship between mechanical aperture and hydraulic conductivity. During the experiments, circumferential displacements were measured. A component of the displacements was due to elastic deformation of the intact rock matrix, and a component was due to deformation (opening / closing) of the fracture. In order to determine the latter component, it was necessary to subtract the matrix deformation from the measured deformation.

Sample 4 had a low hydraulic conductivity and a low change in circumference compared to the other samples tested. When pried apart, it was observed that the fracture did not extend entirely through the sample. The K_{eq} of the sample was 1.9 x 10^{-10} m/s, which falls within the range of matrix testing results (1.89 x 10^{-11} to 3.18 x 10^{-10} m/s). The sample was hence regarded as effectively intact matrix and suitable to use as an indicator of matrix compressibility. The effects of compressibility due to effective stress were calculated and subtracted from the other samples (2, 3, 5, 6) to determine a corrected change in circumference, and in turn a corrected change in aperture. Figure 4.16 illustrates the manner in which the correction was applied for one of the samples. Figure 4.16 a) shows raw circumferential displacement for samples 3 and 4; b) displays the corrected circumferential displacement of sample 3 based on sample 4; c) displays the resulting change in aperture, which is taken as half of the corrected circumferential displacement.

Change in aperture versus the effective confining pressures for samples 2, 5, and 6 are shown in Figures 4.17 – 4.19 (sample 3 and 4 are included in Figure 4.16).

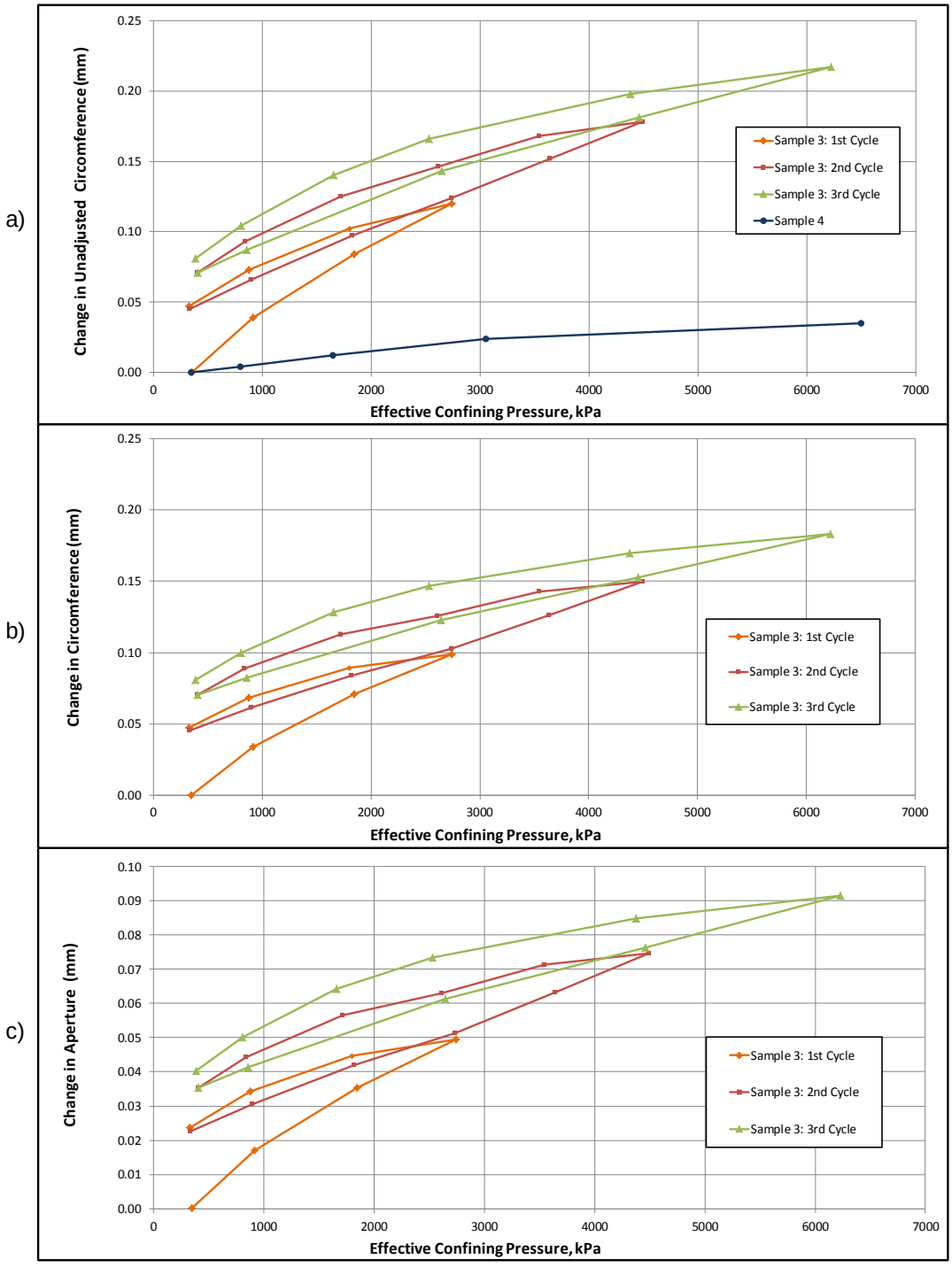

Figure 4.16 - Illustration of method used to interpret fracture aperture change from circumferential deformation measurements: a) measured change in circumference versus effective confining pressure for sample 3 and 4 (“intact” sample; deformation due solely to matrix deformation); b) change in circumference due solely to fracture deformation (matrix deformation subtracted from measured circumferential deformation); c) change in aperture versus confining pressure for sample 3.

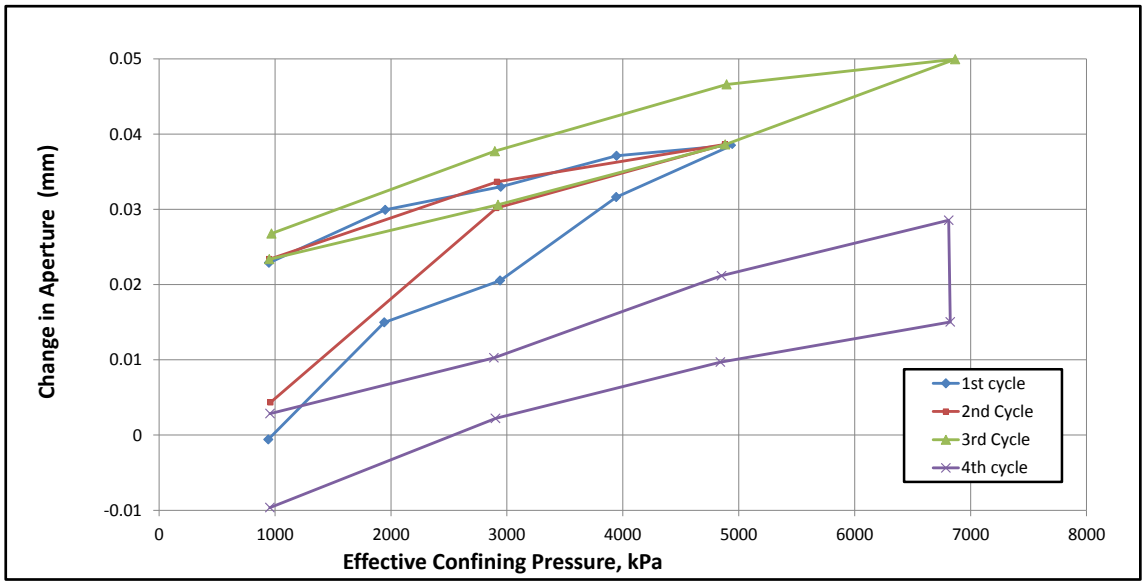

Figure 4.17 - Change in aperture versus effective confining pressure of sample 2. The chain used to measure circumferential displacement used an elastic to create tension. During testing of sample 2, creep in the elastic band caused the chain to relax over the course of the test, causing the measured change in circumference to creep to a lower value. The elastic was replaced with a spring that prevented this on subsequent tests. Graphs from here on dealing with the aperture of sample 2 will only show the 3rd cycle, where the creep error was the least.

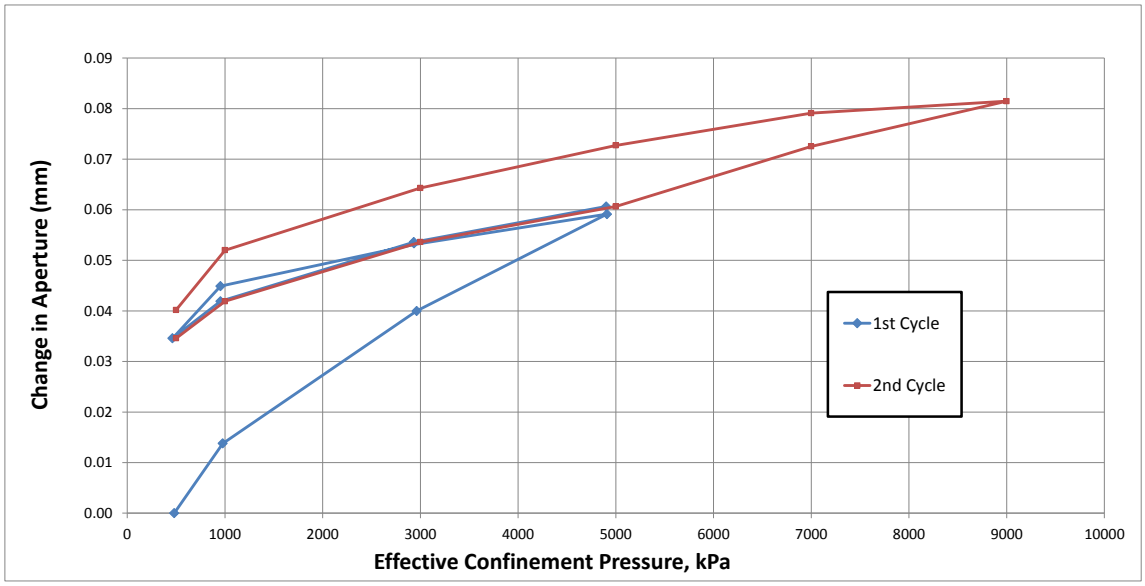

Figure 4.18 - Change in aperture versus effective confining pressure of sample 5

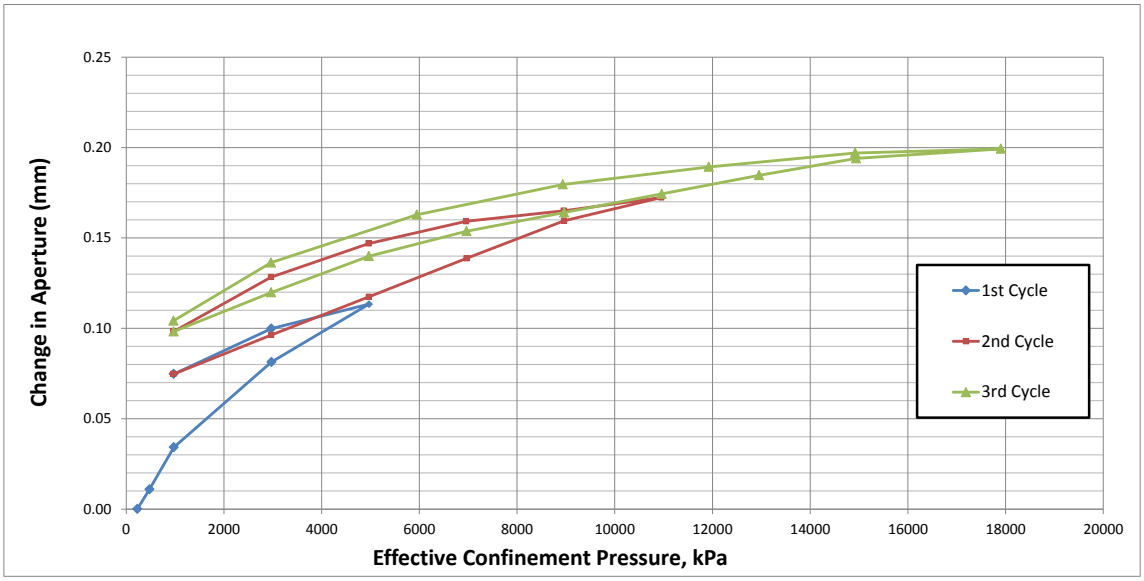

Figure 4.19 - Change in aperture versus effective confining pressure of sample 6

To compare the effects of the change in aperture on equivalent hydraulic conductivity the results from the tests of samples 2, 3, 5, and 6 are combined on Figure 4.20. As expected, all of the tests displayed a drop in equivalent hydraulic conductivity with aperture reduction.

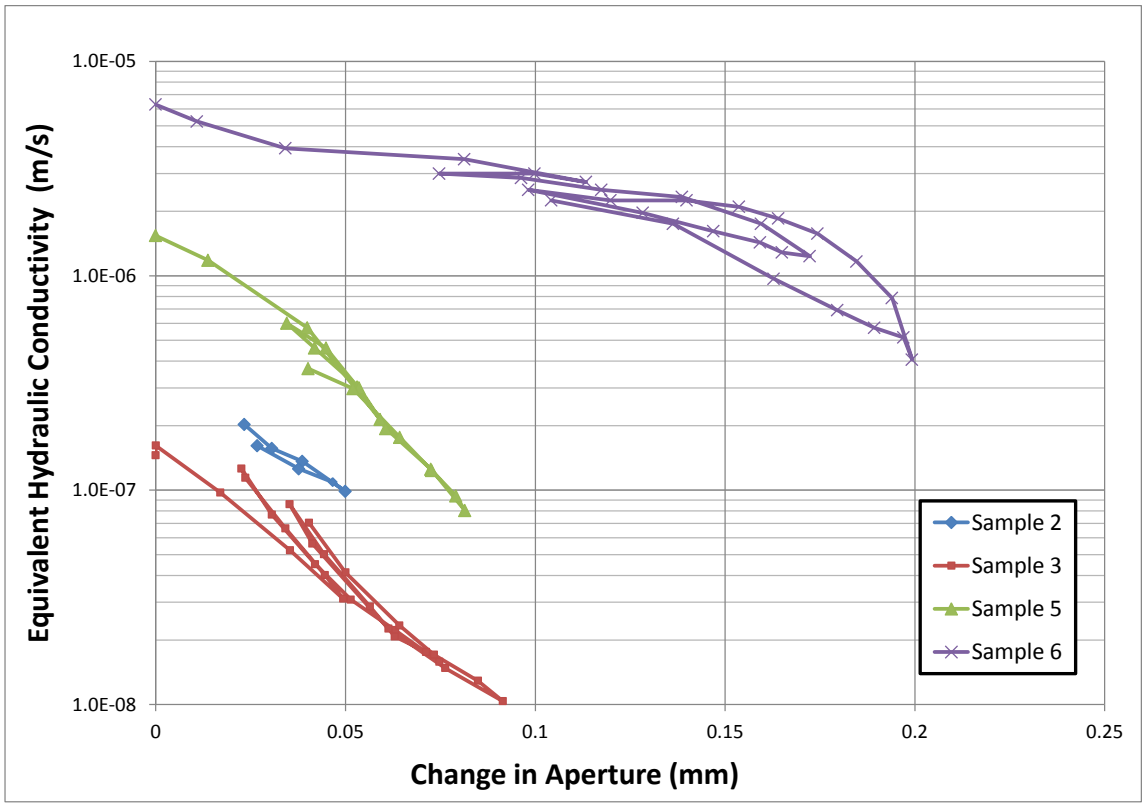

Figure 4.20 - Measured change in mechanical aperture versus the equivalent hydraulic conductivity of samples 2, 3, 5 and 6

4.7 MEASUREMENT OF INITIAL MECHANICAL FRACTURE APERTURE

To further analyze the lab testing results, which provided a measurement of the *change* in aperture during each test, estimates of the initial mechanical fracture apertures were needed. After investigating many methods of aperture estimation, a relatively simple solution was selected. This involved weighing the sample initially, and then coating one of the fracture faces was liberally with a urethane rubber compound. The two faces of the fracture were then mated; a normal stress representative of the initial stress level used in the hydraulic conductivity testing was applied. This stress was maintained for 24 hours (at least) allowing the excess urethane rubber to flow out of the fracture, while the remainder set. After trimming the excess urethane rubber, each sample was weighed. The density of a control sample of the same urethane rubber (after setting in a cup) was also determined, hence enabling calculation of the volume of the fracture.

Based on fracture volume and the length and width of the fracture an average aperture was calculated. Table 4.4 summarizes the calculated apertures, and the corresponding hydraulic conductivities measured at effective confining pressures similar to those used during the aperture measurements.

Table 4.4 – Estimated mechanical aperture values

Sample Number	**Average Mechanical Aperture, mm**	**Measured k_{eq}, m/s**
Sample 2	0.270	4.3E-07
Sample 3	0.279	9.7E-08
Sample 4	0.770	2.1E-09
Sample 5	0.127	1.2E-06
Sample 6	0.277	3.9E-06

When comparing aperture measurements and corresponding hydraulic conductivity values, one grossly anomalous results is evident; most notably, the high aperture measured on sample 4, which had the lowest hydraulic conductivity. This anomaly is deemed to be due to experimental error. The surfaces on sample 4 were not mated well, and a noticeable offset was discovered after the urethane had set. This would have caused a misfit with the asperities, creating an artificially large aperture.

Figure 4.21 shows the hydraulic conductivities of samples 2, 3, 5 and 6 versus their respective apertures using the estimated initial average aperture values and aperture changes resulting from confining pressure change. Samples 5 and 6 seem to follow a similar trend; however, the results from 2 and 3 do not match up. Due to the lack of a clear and consistent trend for all samples, the data does not completely validate the experimental method used for aperture estimation, and the results presented in Table 4.4 should be regarded with caution.

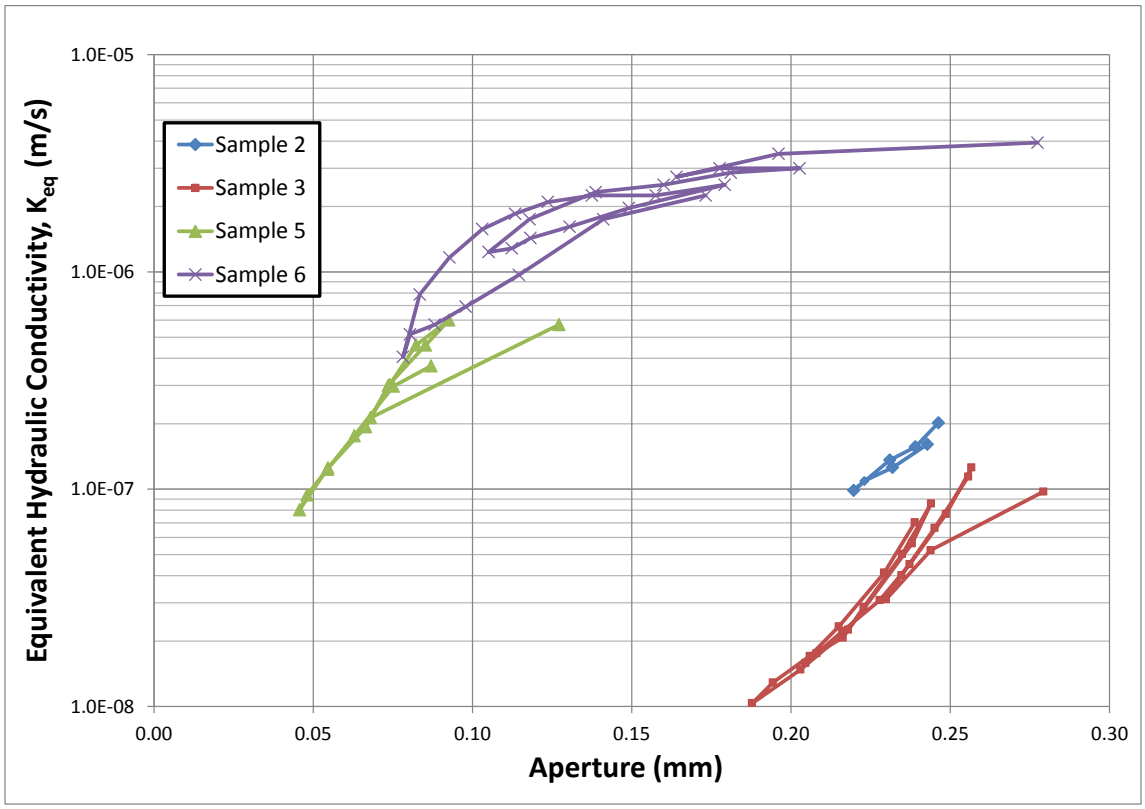

Figure 4.21 - Hydraulic conductivity versus measured aperture

4.8 ASSESSING THEORETICAL APERTURES

Theoretical relationships between fracture aperture and hydraulic conductivity were presented in Chapter 2. In summary, equation 2.7 represents an idealized situation of flow between two smooth parallel surfaces. Equation 2.11 accounts for roughness effects by using micro roughness. Equation 2.12 adapts equation 2.11 to use JRC as a roughness parameter. To assess these three equations they were graphed against the test data generated during this research. In the first set of graphs, figures 4.22 to 4.24, equivalent hydraulic conductivity versus aperture is graphed. Samples 2, 5, and 6 were used for comparison as they are the only samples with micro roughness and JRC estimates. The sample apertures presented were calculated as described in section 4.7.

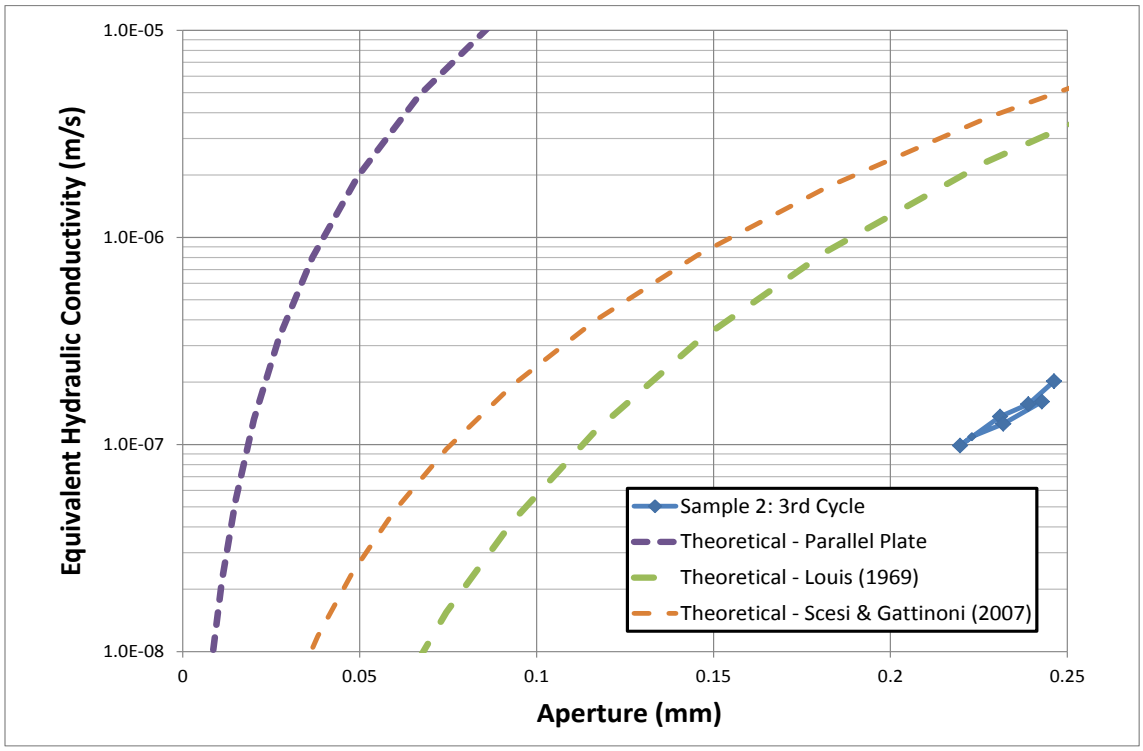

Figure 4.22 - Hydraulic conductivity versus aperture of sample 2 where JRC = 13 and r_a = 1.00 mm

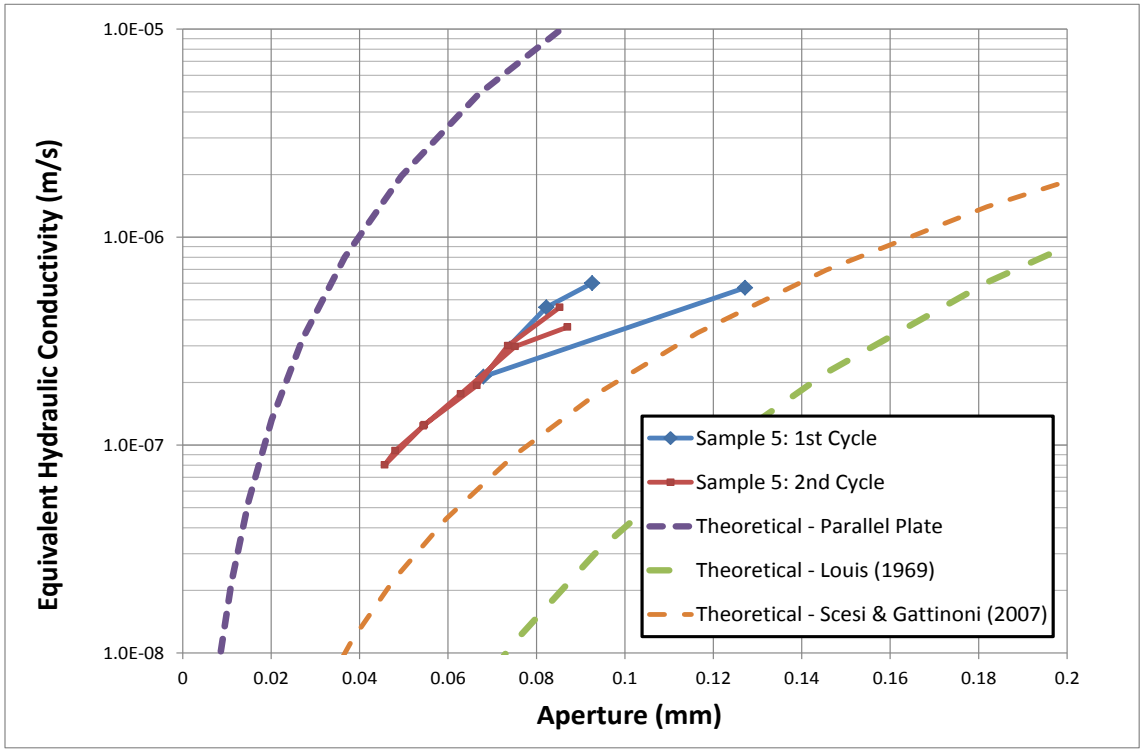

Figure 4.23 - Hydraulic conductivity versus aperture of sample 5 where JRC = 18 and r_a = 1.26 mm

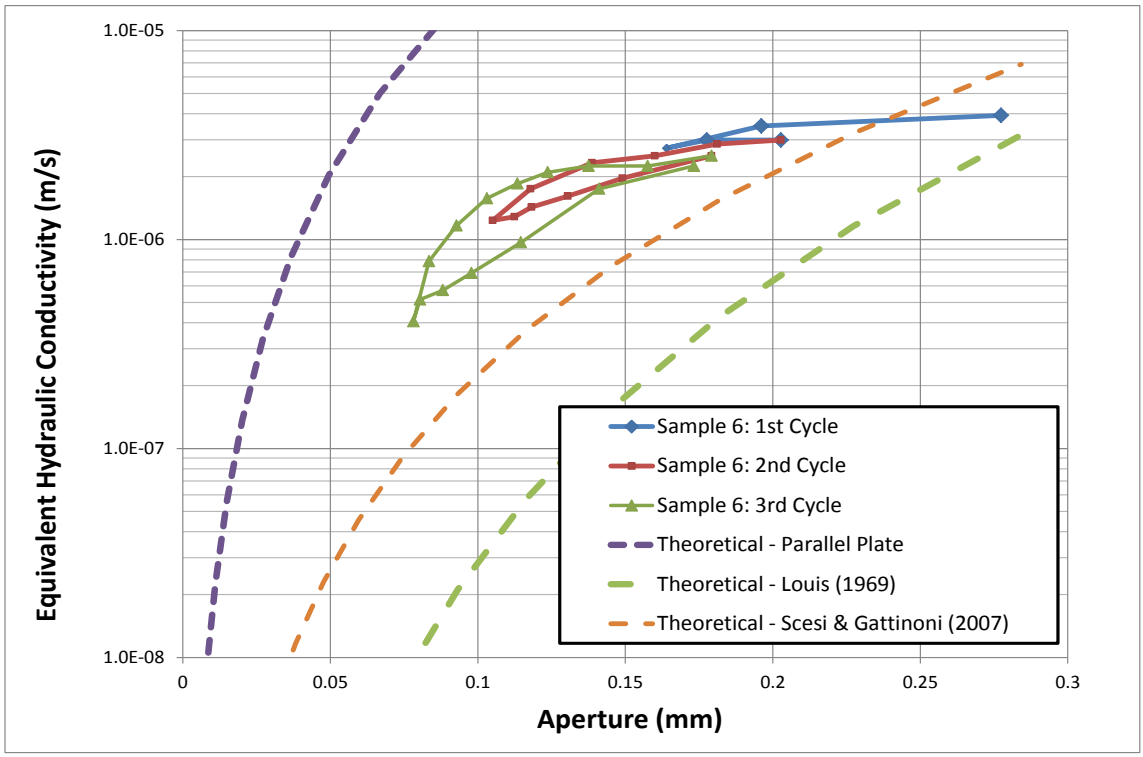

Figure 4.24 - Hydraulic conductivity versus aperture of sample 6 where JRC = 15 and r_a = 1.63 mm

The estimates of initial fracture aperture may not be accurate, as previously discussed. This seems especially likely for sample 2, which correlates poorly with the theoretical estimates as compared to samples 5 and 6. The range of aperture values on sample 2 is over twice of what was predicted by the theoretical relationships. This is most likely due to an error in the initial estimate of aperture.

In order to assess the results against theoretical relationships without using estimates of initial fracture aperture, a comparison of measured and theoretical aperture changes was undertaken. Using the hydraulic conductivity values from lab testing of each sample, aperture values were calculated using each of the three afore-noted theoretical relations (equations 2.7, 2.11 and 2.12), and these values were used in turn to calculate the change in aperture. This latter calculation required an estimate of the initial aperture. For each theoretical relation that was used, a theoretical initial aperture was calculated from the

first measured value of K_{eq}. In essence, this approach assumes that each theoretical relation is valid for the first measurement, then all changes are measured relative to this measurement point. The theoretical relationships determined in this way for samples 2, 5, and 6, are graphed alongside the corresponding lab measurements in Figures 4.25 to 4.27, respectively.

The trends of the two relations that use roughness (i.e., equations 2.11 (Louis,1969) and 2.12 (Scesi and Gattinoni, 2007)), are better aligned with the test data than the parallel plate estimate. This suggests that these equations provide more accurate representations of the relationships between hydraulic conductivity and aperture. Based on Figures 2.24 to 2.27, Scesi and Gattinoni's (2007) equation, which is based on JRC, provides a slightly closer match to the lab data in two out of three cases. This is noteworthy because JRC is a practical and more commonly used roughness parameter in many applications.

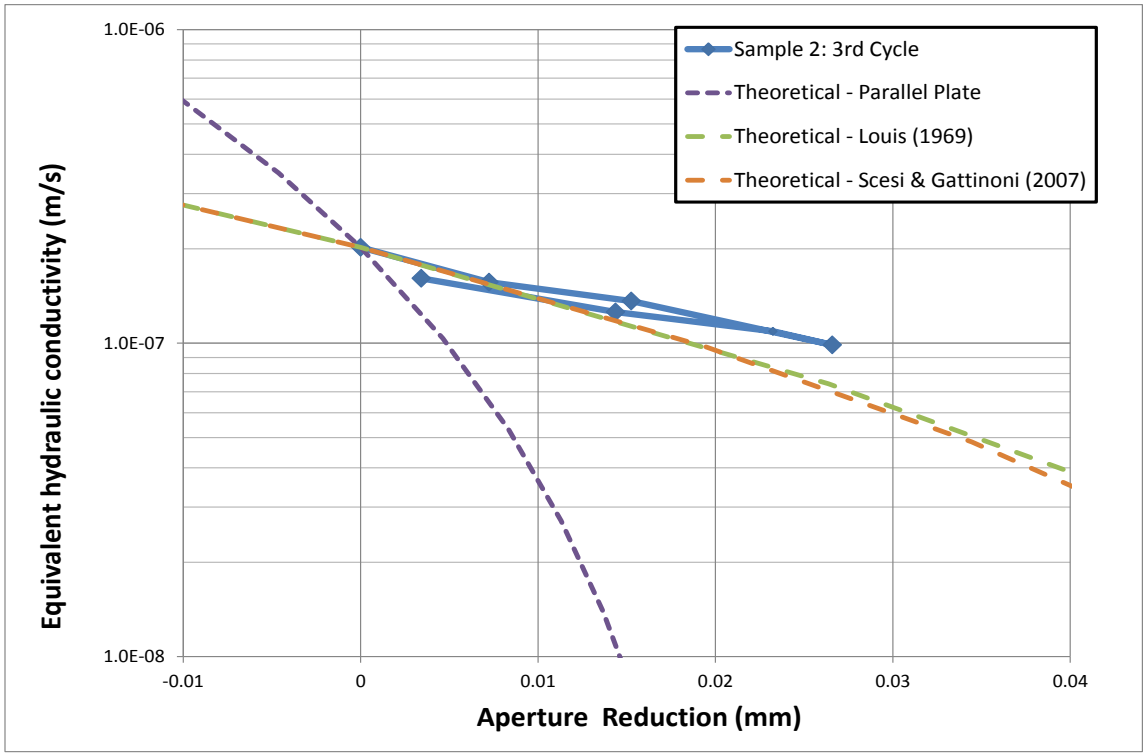

Figure 4.25 - Hydraulic conductivity versus aperture reduction of sample 2

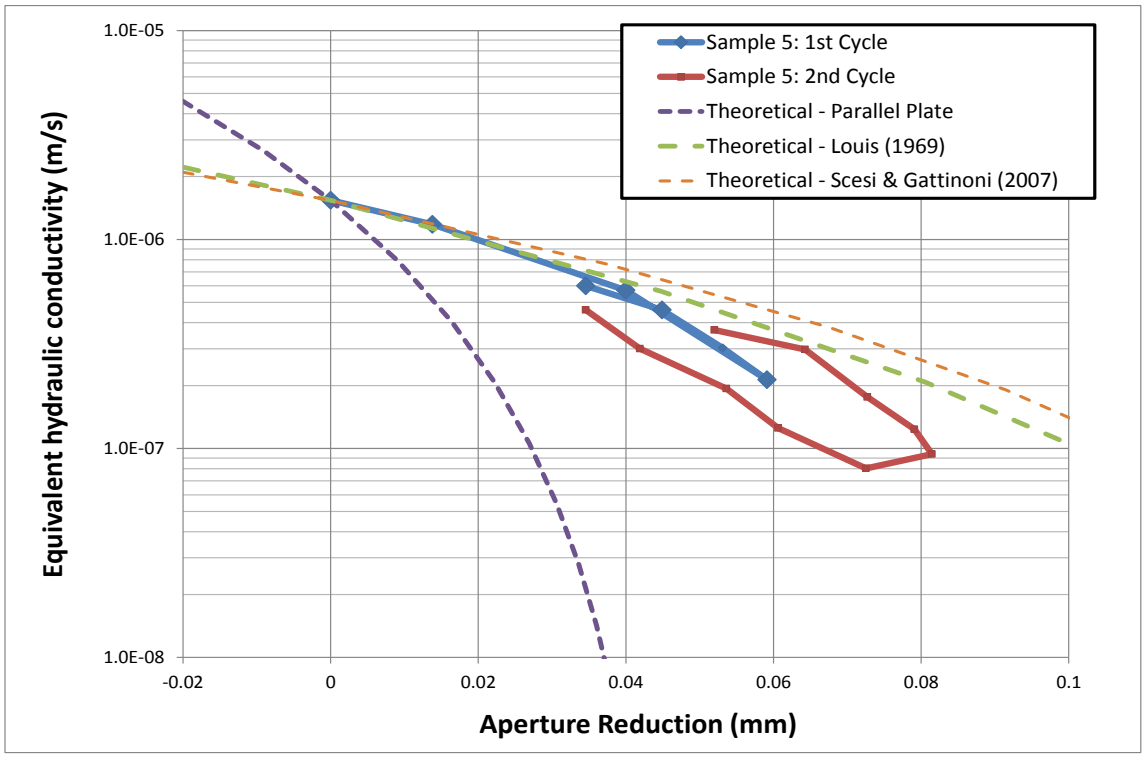

Figure 4.26 - Hydraulic conductivity versus aperture reduction of sample 5

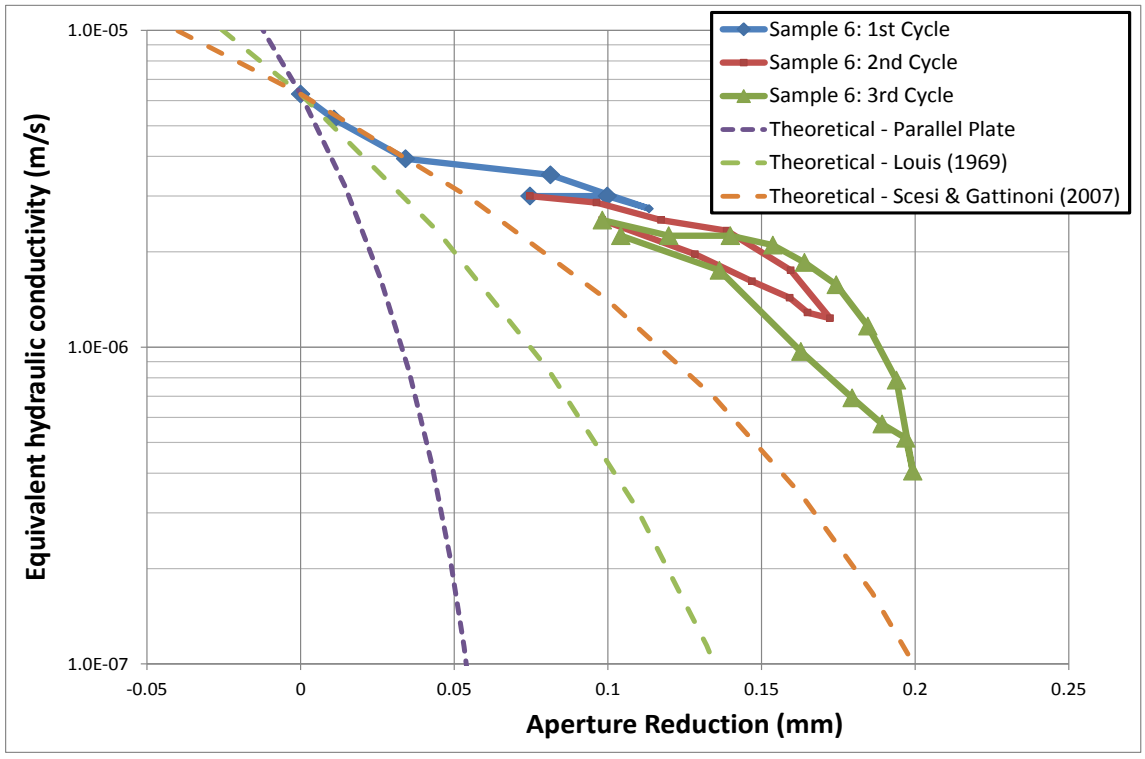

Figure 4.27 - Hydraulic conductivity versus aperture reduction of sample 6

The goal of laboratory testing was to confirm observations made in core logging and attempt to obtain comparable hydraulic conductivity values. Unfortunately, the features that most likely had the largest hydraulic conductivity were not testable. The apertures seen in the open, quartz-lined fractures were estimated to range from 2 to 10 mm. To estimate the effects of these features, a graph of the three theoretical equations was made over this range; see Figure 4.28. For this calculation, average roughness values were assumed (r_a = 1.0 mm and *JRC* = 10).

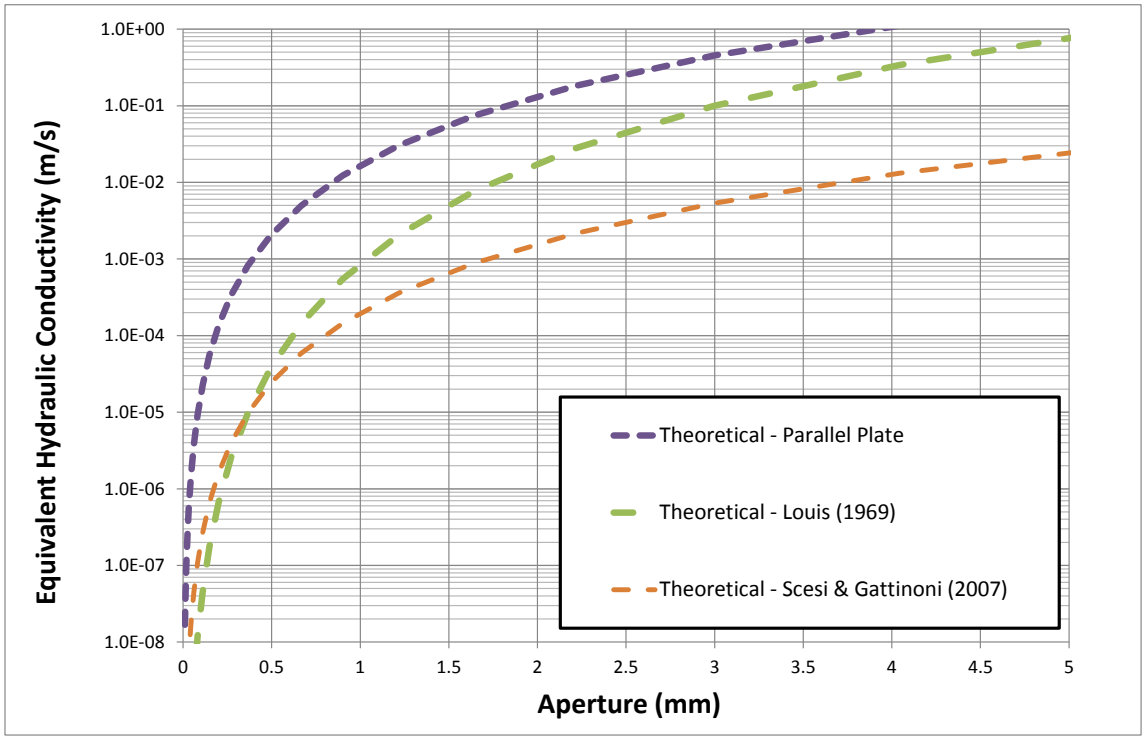

Figure 4.28 - Theoretical hydraulic conductivity versus aperture where JRC = 10 and r_a = 1.00 mm

It is apparent that there is a significant increase in hydraulic conductivity with aperture. The Figure shows the significance of having fractures open more than 1 mm. This supports the hypothesis that the open quartz lined fractures may be very conductive. The graph also demonstrated the deviation of the three theoretical methods when pushed to extreme values.

4.9 LAMINAR FLOW INVESTIGATION

To investigate the validity of assuming a laminar flow, the Reynolds number was calculated for sample 6, for which the largest flow rate (10 ml/min) was achieved during testing. Conservatively (for the purpose of this analysis) estimating a hydraulic aperture of 0.1mm, at a temperature of 20^{o}C, a Reynolds number of 2.69 was calculated. This is well below the commonly accepted threshold number of 2300 for turbulent flow(Sarkar, 2004). Based on Figure 2.11 the lowest threshold for laminar flow is 200, for a rough surface. By either of these estimates, the assumption of using laminar flow appears valid.

4.10 SENSITIVITY OF FRACTURE ROUGHNESS

The equations used above use fracture roughness as a primary input parameter. To investigate the effect of roughness on fracture hydraulic conductivity, a sensitivity analysis was conducted. Using equation 2.1 (based on Louis, 1969), , hydraulic conductivity were calculated over an extreme range of micro roughness values (0.1 mm to 10 mm) and graphed against aperture. The results, shown in Figure 4.29, suggest that roughness can affect hydraulic conductivity by several orders of magnitude. This verifies that roughness is an important parameter to consider when characterizing fractures.

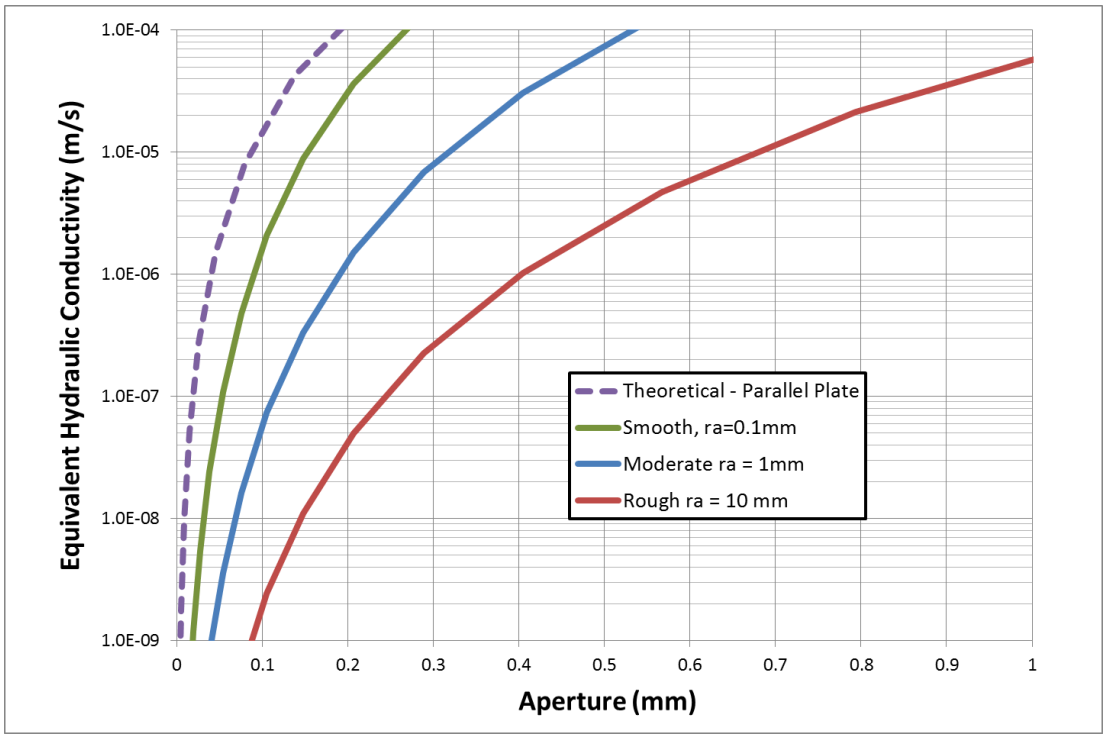

Figure 4.29 – Estimated fracture flow over a range of micro roughness values r_a

4.11 SUMMARY

It was verified that the hydraulic conductivity of the matrix of the Manitou Falls Formation sandstones of the Athabasca Basin near McArthur River mine site is low enough to consider the sandstone as fracture dominated with respect to flow. Six samples were tested to determine the equivalent hydraulic conductivity, K_{eq}, of fractures through the core samples under simulated in-situ conditions. The heavily stained sample showed the highest K_{eq} of the samples tested, which verified the identification of the fractures with potentially high hydraulic conductivity based on staining. The fracture containing voids with quartz crystals proved to have poor connectivity, hence low hydraulic conductivity. Since the apertures measured on this sample were smaller than 0.2 mm and voids observed in the field were up to 10 mm, it is suggested that the lab results are not representative. The presence and shape of the euhedral crystals indicate that relatively large fracture apertures most likely exist, hence

hydraulic conductivities may be relatively high. Theoretical relations between fracture aperture and conductivity were found to be significantly more accurate when fracture roughness is accounted for.

CHAPTER 5 INTEGRATION OF LABORATORY AND FIELD DATA

5.1 HYDRAULOC CONDUCTIVITY AS A FUNCTION OF SCALE OF INVESTIGATION

The concept of representative hydraulic conductivity for a bulk rock mass is based on the assumption that the volume of investigation of a rock mass is large enough so that the behavior of the medium can be described with Darcy's law. In a fractured medium, this implies that the connectivity of the fractures creates a system that behaves in an equivalent manner to a porous medium. This assumption holds true in many situations and was assumed to be valid, at the field scale, for this study. With decreasing scale of investigation, however, individual fractures have a greater influence on overall flow as the number of fractures also decreases. This complicates the comparison of small-scale measurements (such as the lab testing results presented in Chapter 4) and field-scale results. This chapter attempts to upscale the results obtained on fractures tested at the lab scale, to assess their relevance at the large scale. The relationship between depth-related stress increase and hydraulic conductivity is also explored.

5.2 ROCK MASS HYDRAULIC CONDUCTIVITY, $K_{eq\text{-}field}$

As discussed in section 4.4, the equivalent hydraulic conductivity (K_{eq}) values interpreted from the lab testing are based on an average fracture spacing of 50 mm (i.e., 0.05 m). As such, the following equation was used to convert K_{eq} to a field-scale equivalent, $K_{eq\text{-}field}$:

$$K_{eq\text{-}field} = (0.05 / S) * K_{eq} \quad [5.1]$$

Where S is the fracture spacing (in m) determined for the rock mass of interest.

In order to use this equation appropriately, two corrections were required.

Firstly, in order to compensate for the biasing effect of spacing measurements made along a single trajectory (i.e., the borehole axis), the Terzaghi correction was applied to get the corrected fracture spacing $\underline{S_t}$:

$$S_t = L\left(\frac{\sin\alpha}{fc}\right) \qquad [5.2]$$

Where *S* is the adjusted fracture frequency, *L* is the length of the interval studied, *fc* is the fracture count for the interval, and α is the average angle of fracture planes measured relative to the borehole axis.

The second correction pertained to the fact that flow measured in the lab was one-dimensional (i.e., parallel to the core axis, along a single fracture). As noted in Section 2.2, the majority of flow in the Manitou Falls Formation is believed to be carried by two orthogonal, sub-vertical fracture sets. As such, the fracture spacings interpreted from the total number of fractures observed in the field data, were multiplied by two prior to substitution into equation 5.1. As such, the $K_{eq\text{-}field}$ values resulting from these calculations represent the equivalent hydraulic conductivities of the rock mass for flow occurring in two orthogonal directions (i.e., parallel to each sub-vertical fracture set, as illustrated in the right-hand side of Figure 5.1). Though the bi-linear flow system implied by this approach is not identical to the radial flow system assumed in the interpretation of packer testing results, it is deemed to be suitable to enable a rough comparison between these two data types.

An equivalent field-scale hydraulic conductivity was calculated for each borehole interval containing a sample that was measured in the lab testing program. For each sample, a 20 m interval (10 m above and 10 m below the sample depth) was used to calculate the fracture spacing and mean fracture angle. The results are listed in Table 5.1.

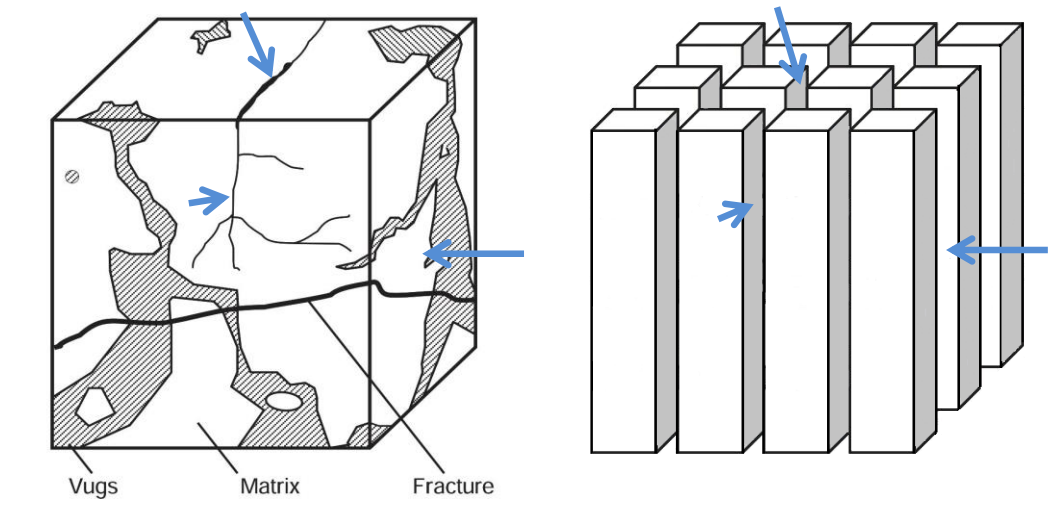

Figure 5.1 - Three dimensional flow simplified in a match stick model (after Warren, 1962 and Aguilera, 1987)

Table 5.1 – List of fractured samples and Hydraulic Conductivity

Sample No.	Hole	Depth (m)	K_{eq} (m/s)	Fracture Spacing, S (m)	Flow Direction Adjusted Fracture Spacing (m)	Average α (°)	Corrected Fracture Spacing, S_t (m)	$K_{eq\text{-}field}$ (m/s)
2	MC-316	335.44 – 335.76	4.3E-07	3.4	6.7	18	2.06	$2.09X10^{-8}$
3	SP-001	132.8 – 133.1	9.7E-08	5	10.0	37	4.02	$2.4x10^{-9}$
4	Sp-001	150.0 – 150.3	2.1E-09	5	10.0	25	2.76	$7.61x10^{-11}$
5	MC-316	306.60 – 306.87	1.2E-06	20	40.0	7	4.88	$2.46x10^{-8}$
6	SP-001	288.7 – 289.0	3.9E-06	6.2	12.4	14	1.66	$2.35x10^{-7}$

5.3 COMPARING SCALES OF INVESTIGATION

The field adapted equivalent hydraulic conductivity, $K_{eq\text{-}field}$ and the hydraulic conductivity from packer tests are show in Figure 5.2. The results, especially at shallow depths, reflect some differences between the two methods. One difference is in assumed flow regimes (bi-linear for the lab testing; radial for the packer testing). Another significant difference comes from the limitations of testing open fractures in the laboratory. Several fractures were observed with apertures thought to be several times larger than those tested in the lab. The effects of larger apertures were demonstrated with the theoretical results in Chapter 4, Figure 4.28. The results are also supported by findings of Winkler and Reichl (2014), who concluded that to truly characterize an aquifer tests at multiple scales must be conducted.

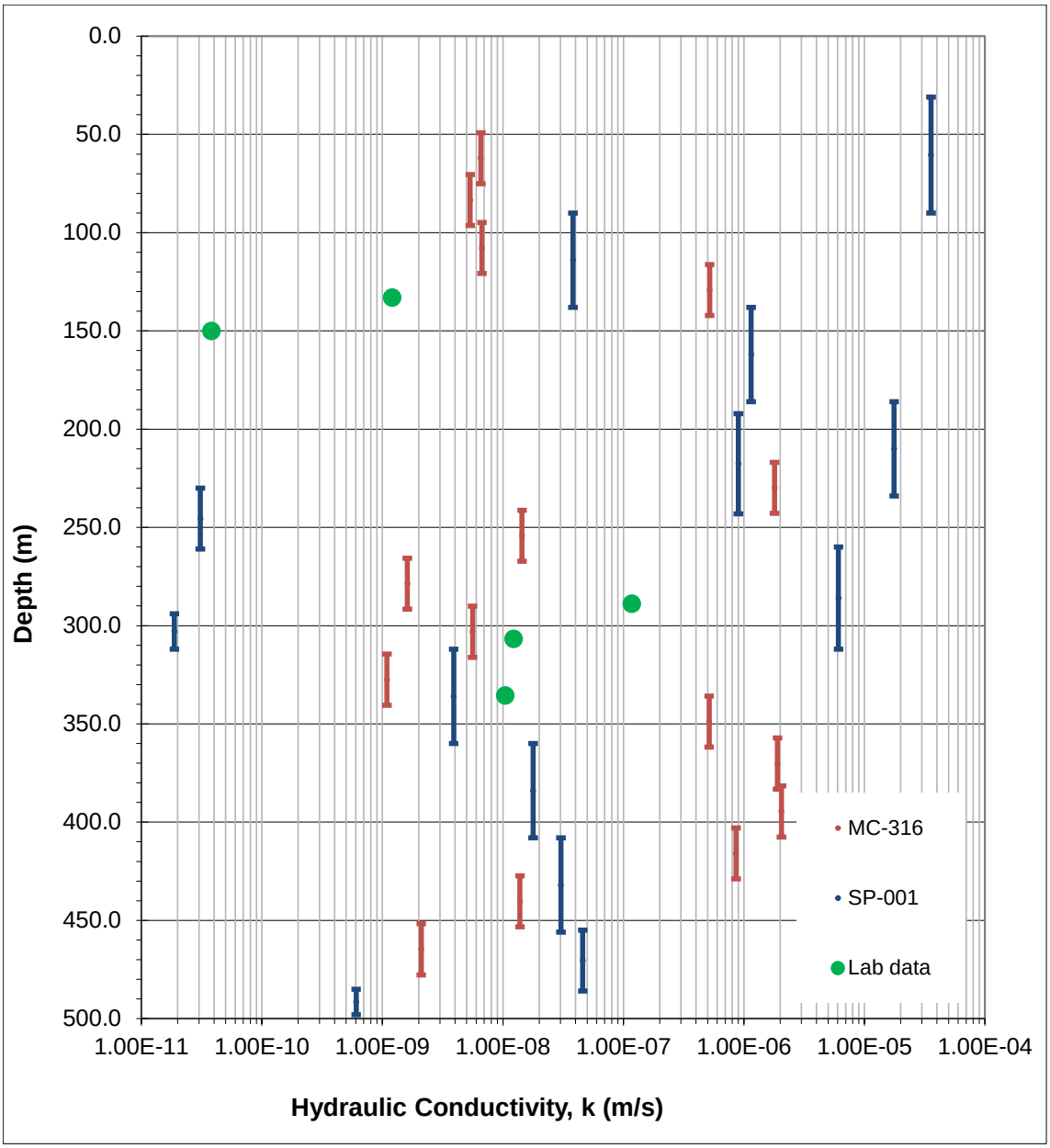

Figure 5.2 - Comparisons of lab and field data. Core samples from lab data originate from both MC-316 and SP-001

Figure 5.3 contains a compilation of measured hydraulic conductivities over a broad range of scales. Packer testing results from MC-316 and SP-001 have been added in blue. Lab testing data is shown in red (fractured samples) and green (matrix).

The lab measurements made in this research are in the typical range for the field results. The lab-scale values were generally lower than the packer test results. This can be attributed to the fact that fractures responsible for maximum hydraulic conductivity values are in a state that could not be sampled and tested in the lab. This highlights a limitation of lab testing in general.

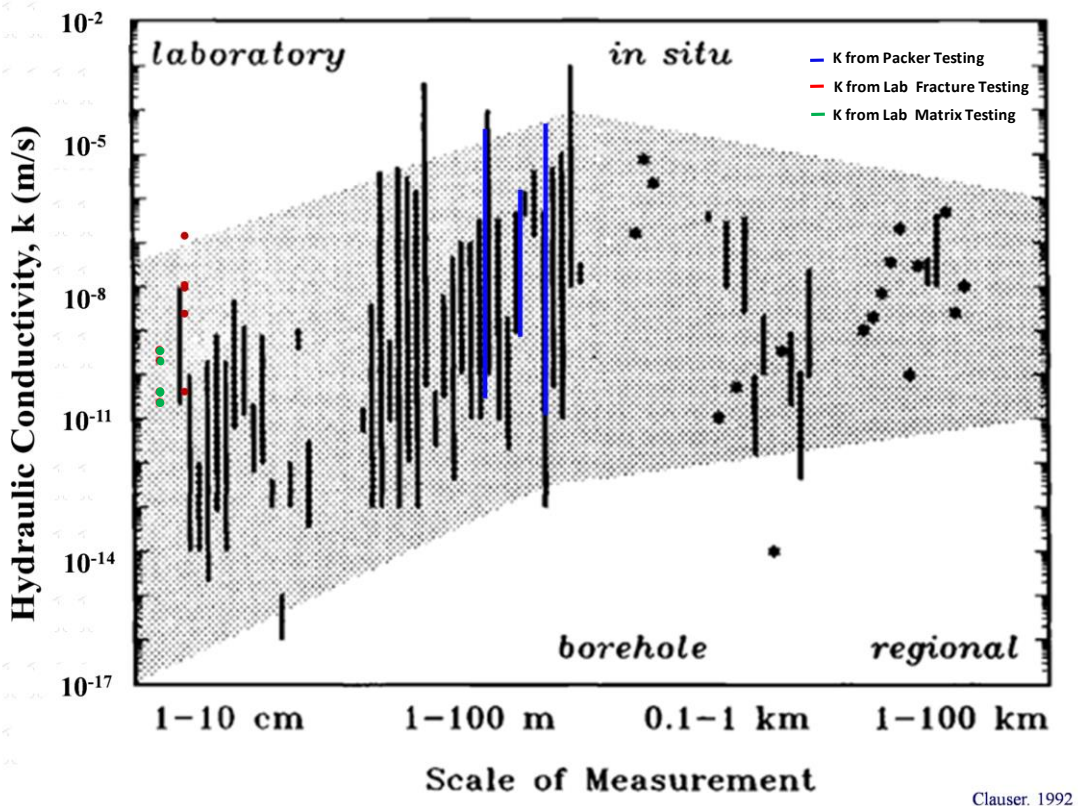

Figure 5.3 - Hydraulic conductivity data over a range of scales (after Clauser, 1992)

5.4 STRESS AND HYDRAULIC CONDUCTIVITY

A relationship between stress and hydraulic conductivity was observed during lab testing. Increasing effective confining pressure caused fracture closure and a reduction in the hydraulic conductivity, though the magnitude of the effect diminished with increasing confining pressure. This is consistent with the relationship between aperture (hence conductivity) and stress observed in laboratory data (see sections 4.5 and 4.6), and generally reported in rock mechanics literature (see section 2.3.5). It thus seems reasonable to expect that such an effect should occur in-situ, where effective stress increases with depth.

Figure 5.4 shows calculated rock mass hydraulic conductivity versus theoretical depth for all five fractured samples that were tested. Pressure for each test was converted to depth assuming a 2:1 horizontal to vertical stress ratio, and an average rock specific gravity of 2.4. All of the samples show a trend of reduced rock mass hydraulic cond

uctivity with increasing depth due to the closure of the fractures. The hydraulic conductivities from packer tests from 15 drill holes at McArthur River are shown in Figure 5.4. No apparent trends can be seen with depth for the packer test data, and the conductivities interpreted from packer testing tend to be significantly greater than the lab-derived depth profiles. It should be noted that in some of the drill holes the packer testing methods were not consistent, and testing often focused on the zones presumed to have higher hydraulic conductivity.

Figure 5.5 displays compilation of hydraulic conductivity with depth from various locations. It supports the trend predicted using the lab data, as does a study by Rutqvist and Stephansson (2002). The depths ranges tested far exceed those conducted in this study. Figure 5.6 is split into two parts; the lower part is labeled with the mechanisms acting on the fractures. All data in the Manitou Falls sandstone falls under the brittle deformation part of the graph, but the depth interval analyzed in this study might be too small to reveal a trend, especially considering the heterogeneity in fracture attributes and spacings.

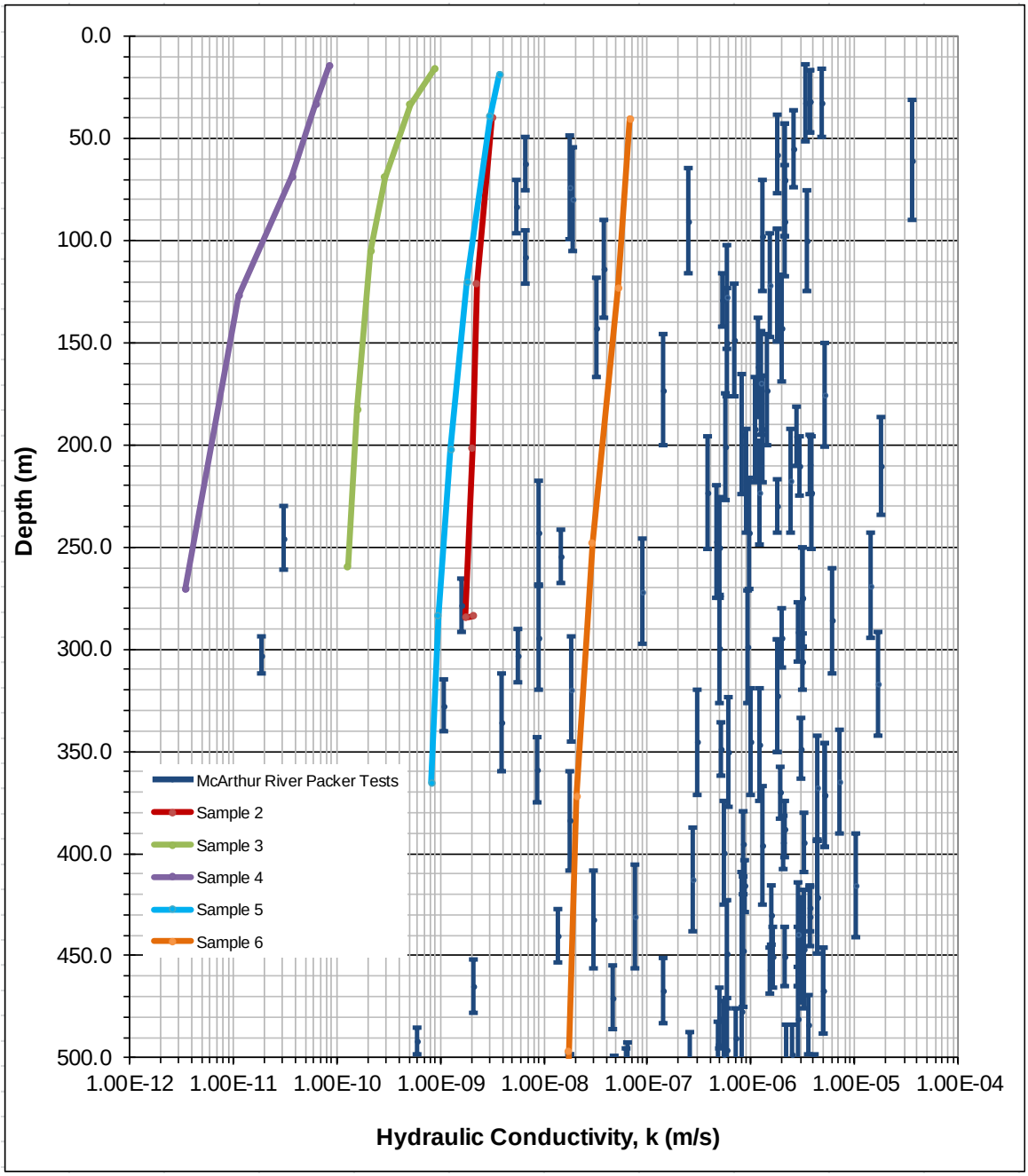

Figure 5.4 – Theoretical rock mass hydraulic conductivity (calculated from laboratory data) against depth, compared to packer testing results compiled for 15 drill holes at the McArthur River mine site.

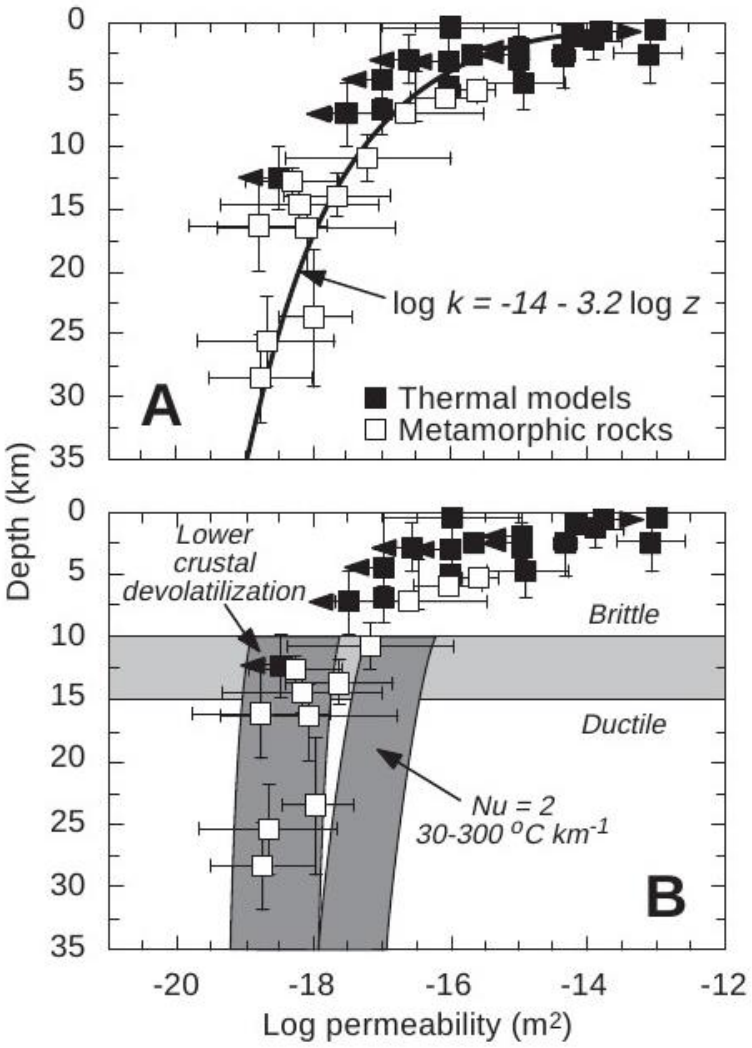

Figure 5.5 - Hydraulic conductivity with depth (after Ingebritsen and Manning, 1999)

5.6 SUMMARY

The scale of interpretation for a given test type is an important factor to consider when assessing hydrogeological information. Testing on the small scale tends to underestimate the range of hydraulic conductivity values occurring at the large scale.

For a given fracture, effective stress has been found to influence hydraulic conductivity causing a general decrease in hydraulic conductivity with depth due to fracture closure. However variations in fracture attributes and spacing can obscure this trend.

CHAPTER 6 CONCLUSIONS AND RECOMMENDATIONS

6.1 CONCULSIONS

General trends in hydraulic continuity can be obtained from core logging data. By focusing efforts on indicators of flow, a good understanding of potential inflow can be obtained prior to conducting more sophisticated and expensive testing. The core-based techniques applied to the Manitou Falls Formation in this work do not give accurate estimates of field-scale hydraulic conductivity, but they can identify zones where more detailed packer testing and geophysical assessment of the rock are warranted. In the cores studied, it was found that an increase in sub vertical fractures generally indicated a potential increase in hydraulic conductivity. Similarly, fractures showing oxidization or other staining (most notably, limonite) tended to be associated with zones of elevated hydraulic conductivity. Open quartz-lined fractures were also observed in zones of high hydraulic conductivity. Based on observations noted for these fractures, it appears they have apertures of several millimeters and would be significant conduits of flow.

Through lab testing it was verified that hydraulic conductivities of the Manitou Falls sandstone matrix are low relative to fractures, and the matrix may be considered impermeable for most practical applications. This verifies the author's initial hypothesis that flow in this sandstone is predominantly fracture controlled

Six fractured core samples were tested in a cell to determine the equivalent hydraulic conductivity, K_{eq}, under simulated in-situ conditions. The heavily stained sample showed the highest K_{eq} of the samples tested, which verified this author's interpretation of core logging and packer testing data. Laboratory testing of the fracture containing quartz crystals did not directly confirm observations based on core logging and packer testing, as this sample actually had the lowest hydraulic conductivity. Closer inspection revealed that the areas of open aperture in this sample were small (sub-millimeter) and poorly connected, compared to other fractures that were observed to be well connected with apertures up to 10 mm. It is presumed that laboratory testing of the latter intervals,

had it been possible, would have confirmed that these features are large conduits of flow in situ.

The laser roughness profilometer (LRP) proved to be a quick and easy field tool to extract JRC and micro roughness from a fracture. Equations accounting for fracture roughness (e.g., Louis, 1969) proved to be more effective than the smooth-walled fracture model for relating fracture aperture to hydraulic conductivity.

Testing of individual fracture samples is not efficient or the most productive method of estimating bulk hydraulic conductivity. It does highlight the complexity of rock mass flow. At smaller scales individual fractures become more important. The scale of information required is a critical starting point when designing a program to test for hydraulic conductivity. Core logging can be a powerful tool to characterize a rock mass. As a drill hole is being advanced attention to the degree of staining, fracture orientation and spacing, and indications of open fractures is critical to an efficient packer test program. Once packer testing is complete fractured samples can be tested to gain a detailed understanding of the features underlying the hydraulic behavior of the rock mass.

Hydraulic conductivity of a rock mass is generally expected to decrease with depth due to the increase of stress, which results in fracture closure. This trend was not clearly observed in this investigation, however, due to rock mass heterogeneity.

6.2 RECOMMENDATIONS

It was not feasible to obtain roughness measurements for all of the samples collected. More measurements of this type are recommended, and they would provide more insight into the relationship between roughness and hydraulic conductivity.

The pursuit of a method to estimate mechanical apertures with greater precision is recommended. High resolution x-ray techniques have proved reliable in other applications, but were not feasible for this project. A dependable estimate of fracture aperture would complement the flow testing that was conducted.

More investigation of fracture (joint) set orientations should be undertaken to assess if three sets truly are consistently present in the Manitou Fall Formation.

It may be possible to model fracture flow using distributions of fractures and fracture hydraulic conductivity. In addition to collecting additional field data, it is recommended that a more rigorous modeling method for upscaling laboratory and borehole measurements should be developed.

Fractures with clay infilling were not recorded during core logging, as fractures were considered either stained or clean. If clays are present, they may clog fractures and reduce flow. The effects of the clay infilling were not tested or explored during this investigation. Further study on the presence of clay, and its effects on flow, is recommended.

REFERENCES

Aguilera, R. 1987. Well Test Analysis of Naturally Fractured Reservoirs. Paper SPE 13663, SPE Formation Evaluation, p. 239 - 252,

Aldrin Resources. http://www.aldrinresourcecorp.com/i/maps/Triple-M-Location.jpg. Accessed on February 2, 2015

Association for Standards in Testing of Materials. 2008. Standard Test Method for Laboratory Determination of Pulse Velocities and Ultrasonic Elastic Constants of Rock. Standard No. D2845 – 08.

Baker, W. J. 1955. Flow in fissured formations. In Proceedings Fourth Petroleum Congress, Rome (Vol. 2, No. 1955, pp. 379-393).

Barton, N., & Choubey, V. 1977. The shear strength of rock joints in theory and practice. Rock Mechanics, 10(1-2), 1-54.

Barton N. and Bandis SC. 1982. "Effects of block size on the shear behaviour of jointed rock–23rd US Symp. on Rock Mechanics. 739-760.

Barton, N Bandis, S., & Bakhtar, K. 1985. Strength, deformation and conductivity coupling of rock joints. In International Journal of Rock Mechanics and Mining Sciences & Geomechanics Abstracts (Vol. 22, No. 3, pp. 121-140).

Beattie, D. 2007. Impact of Geotechnical Parameters Upon Shaft Sinking Performance in the Athabasca Basin. Cameco Engineering and Projects. Cameco Internal Report

Brown, T. 1981. Rock Characterization, Testing and Monitoring. Pergamon Press. ISRM, Yellow Book.

Clauser, C. 1992. Permeability of crystalline rocks. Eos, Transactions American Geophysical Union, 73(21), 233-238.

Cook, P., 2003. A Guide to Regional Groundwater Flow in Fractured Rock Aquifers. Peter Cook. CSIRO Land and Water, Glen Osmong SA Australia. Seaview Press, Hentley Beach, South Australia.

DeCoursey, W. 2003. Statistics and probability for engineering applications. Elsevier. doi:10.1016/B978-075067618-2/50000-7

Golder Associates. 1997. Hydraulic Conductivity Testing Vent Shaft Pilot Holes MAC 258 and MAC 259 McArthur River Project 1996. Project # 962-6420. Prepared for Cameco Corporation.

Golder Associates. 1998. Hydraulic Conductivity Testing Shaft No. 3 Pilot Hole MAC 260 - Report by Golder Associates 1997. Project # 972-6669. Prepared for Cameco Corporation

Golder Associates Ltd. 2002. Geotechnical and Hydrogeological Assessment of No. 2 Pilot Hole 233, Cigar Lake Project, Saskatchewan. Project #022-1475. Prepared for Cameco Corporation.

Golder Associates. 2009. Geotechnical and Hydrogeological Testing for Proposed Shaft 4 Pilot Holes. Project Number 08-1362-0560. Prepared for Cameco Corporation.

Goodman,R.E., 1989, Introduction to Rock Mechanics. Library of Congress Cataloging in Publication Data.

Goodman, R. E., and Yuzo Ohnishi. 1973. Undrained shear testing of jointed rock. Rock Mechanics 5.3 129-149.

GR Pertrology Consultants. 2010. XRD, SEM, and Elemental Analysis of Five Solid Samples for University of Saskatchewan. GR 16019 2010

GR Pertrology Consultants. 2011. Elemental Analysis and Thin Section Photography of Two Solid Samples for University of Saskatchewan. GR 16019 2011

Hakami, Eva, and Erik Larsson. 1996. Aperture Measurements and Flow Experiments on a Single Natural Fracture. International Journal of Rock Mechanics and Mining Sciences & Geomechanics Abstracts. Vol. 33. No. 4. Pergamon,

Iwai, K. 1976. Fundamental Studies of Fluid Flow through a Single Fracture. Doctoral Dissertation, University of California, Berkeley.

Jefferson, C. W., Delaney, G., & Olson, R. A. 2003. EXTECH IV Athabasca Uranium Multidisciplinary Study of Northern Saskatchewan and Alberta, Part 1: Overview and Impact. Current Research, C18.

Jefferson, C. W., Thomas, D. J., Gandhi, S. S., Ramaekers, P., Delaney, G., Brisbin, D., Olson, R. A. 2007. Unconformity-associated uranium deposits of the Athabasca Basin, Saskatchewan and Alberta. Bulletin-Geological Survey of Canada, 588, 23.

Jensen, J. A., Holm, O., Jerisen, L. J., Bendsen, H., Nikolov, S. I., Tomov, B. G., Ammelmark, K. L. 2005. Ultrasound Research Scanner for real-time Synthetic

Aperture Data Acquisition. Ultrasonics, Ferroelectrics, and Frequency Control, IEEE Transactions on, 52(5), 881-891.

Johns, R. A., Steude, J. S., Castanier, L. M., & Roberts, P. V. 1993. Nondestructive Measurements of Fracture Aperture in Crystalline Rock Cores using X ray Computed Tomography. Journal of Geophysical Research: Solid Earth (1978–2012), 98(B2), 1889-1900.

Klimczak, C., Schultz, R. A., Parashar, R., & Reeves, D. M. 2010. Cubic Law with Aperture-Length Correlation: Implications for Network Scale Fluid Flow. Hydrogeology Journal, 18(4), 851-862.

Lee, C. H., & Farmer, I. W. 1993. Fluid flow in Discontinuous Rocks. Cahpman & Hall, London.

Louis, C, 1969, A Study of Ground Water Flow in Jointed Rocks and its Influence on the Stability of Rock Masses. Imperial College of Rock Mechanics Research Report No. 10, 90pg.

Mahoney, T. 2009. Conversation at McArthur River Mine

Manning, C. E., and S. E. Ingebritsen. 1999. Permeability of the Continental Crust: Implications of Geothermal Data and Metamorphic Systems. Reviews of Geophysics 37.1 127-150.

Milne, D., Hawkes, C. and Hamilton, C. 2009. A New Tool for the Field Characterization of Joint Surfaces, 3rd Canada – US Rock Mechanics Symposium, Toronto, Canada.

Ramaekers, P. 1990. Geological Maps of the Athabasca Group (Helikian) in Northern Saskatchewan. Saskatchewan Energy and Mines, Saskatchewan Geology Survey

Ramaekers, P., G. Yeo, and C. Jefferson. 2001. Preliminary overview of regional stratigraphy in the Late Paleoproterozoic Athabasca Basin, Saskatchewan and Alberta. Summary of Investigations 2 (2001): 2001-4.

Robb, J. L., Kotzer, T., Hawkes, C., 2007. Investigation of the 3D Geometry of Low Permeability Rocks using Synchrotron X-Ray Computed Microtomography." Earth and Environmental Science. 97-99.

Romm, E. S. 1966. Flow Characteristics of Fractured Rocks. Nedra, Moscow, 283.

Rutqvist, J., Stephansson, O., 2002. The Role of Hydraulic Coupling in Fractured Rock Engineering. Hydrogeology Journal 11 7-30

Scesi,L., Gattinoni, P., Roughness Control on Hydraulic Conductivity in Fractured Rocks. Hydrogeology Journal. 15, 201-211

Sarkar, Sudipta, M. Nafi Toksoz, and Daniel R. Burns. 2004. Fluid Flow Modeling in Fractures. Massachusetts Institute of Technology. Earth Resources Laboratory

Sharp, J. C. (1970). Fluid Flow Through Fissured Media. Doctoral Dissertation. University of London, Imperial College London

Sharp, J.M., Al-Johar, M.M., Slottke, D.T., Ketcham, R.A. 2014. Predition of Fracture Roughness and other Hydraulic Properties: Is upscaling Possible? Fractured Rock Hydrogeology. International Association of Hydrogeologists Selected Papers. CRC Press, London

Snow, D. T. 1969. Anisotropic Permeability of Fractured Media. Water Resources Research, 5(6), 1273-1289.

Sutera, Salvatore P., and Richard Skalak. 1993. The history of Poiseuille's law. Annual Review of Fluid Mechanics 25.1 1-20.

Voegele, M., E. Hardin, D. Lingle, M. Board, N. Barton, 1981. Site Characterization of Joint Permeabilty Using the Heated Black Test. Proceedings of the 22nd U.S Symposium on Rock Mechanics, Boston, Massachusetts, pp. 120-127

Warren, J.E. and Root, P.J. 1962. "The Behavior of Naturally Fractured Reservoirs". Paper SPE 426 presented at the Fall Meeting of the Society of Petroleum Engineers in Los Angeles, October 7 - 10, 1962.

Winkler, G. Reichl, P. 2014. Scale Dependent Hydraulic Investigations of Faulted Vrystalline Rocks – Examples from Eastern Alps, Austria. Fractured Rock Hydrogeology. International Association of Hydrogeologists Selected Papers. CRC Press, London2014 Page 93

Witherspoon, P. A., Wang, J. S. Y., Iwai, K., & Gale, J. E. 1980. Validity of Cubic Law for Fluid Flow in a Deformable Rock Fracture. Water resources research, 16(6), 1016-1024.

Yeo, G., Jefferson, C. W., & Ramaekers, P. 2002. A Preliminary Comparison of Manitou Falls Formation Stratigraphy in Four Athabasca Basin Deposystems. Summary of Investigations, 2, 2002-4.

APPENDIX – REPORTS FROM GR PETROLOGY

XRD, SEM, and Elemental Analysis

of

Five Solid Samples

for

University of Saskatchewan

GR 16019 2010

GR Petrology Consultants Inc.
Suite 8, 1323 – 44th Avenue N.E.
Calgary, Alberta T2E 6L5
Tel: 403-291-3420 Fax: 403-250-7212
E-mail: berna.hablado@grpetrology.com

November 2010

XRD, SEM, and Elemental Analysis of Five Solid Samples
University of Saskatchewan

Summary of Analyses

Five solid samples were submitted by University of Saskatchewan for bulk X-ray Diffraction Analysis (XRD), elemental analysis by X-ray Energy Dispersive Spectrometry (EDS) and Scanning Electron Microscopy (SEM).

Quantitative elemental analysis was performed by an **Oxford INCA** microanalysis system attached to a **JEOL JSM-6610** scanning electron microscope. The INCA system was designed to obtain standardless quantitative elemental analysis from rough samples by SEM. The INCA system has enhanced light element capabilities, and is able to identify beryllium (Be), and quantify boron (B), and carbon (C).

The following Tables, Figures and Plates are included in this report:

- Table A: Bulk Fraction X-Ray Diffraction Data
- Table B: Comparison of Elemental Composition by EDS and XRD
- Plates 1 to 5: Photographs and EDS Results
- Tables 1 to 5: EDS and XRD Results
- Figures 1 to 5: Bulk X-Ray Diffractograms

The following samples were analyzed:

- GR-001: MC316 321.14 Rust Weathered Surface
- GR-002: MC316 321.14 Grey Weathered Surface
- GR-003: MC316 321.14 Matrix
- GR-004: SP001 288.8 Grey Weathered Surface
- GR-005: SP001 288.8 Matrix

COMPANY: University of Saskatchewan
GR PROJECT #: GR 16019 2010
COMPANY: University of Saskatchewan
GR FILE #: GR 16019 2010

TABLE A
BULK FRACTION X-RAY DIFFRACTION DATA

GR Sample #	Sample ID	Qtz	KFd	Plag	Pyr	Sid	Kaol	Ill	Chl	M-L	Smec	Total Clay
GR-001	MC316 321.14 Rust Weathered Surface	95.6	0.7	-	1.0	0.5	-	2.2	-	-	-	2.2
GR-002	MC316 321.14 Grey Weathered Surface	100.0	-	-	-	-	-	-	-	-	-	0.0
GR-003	MC316 321.14 Matrix	95.9	1.1	-	-	-	-	3.0	-	-	-	3.0
GR-004	SP001 288.8 Grey Weathered Surface	100.0	-	-	-	-	-	-	-	-	-	0.0
GR-005	SP001 288.8 Matrix	96.1	0.5	-	-	-	1.7	1.7	-	-	-	3.4

Qtz - Quartz - SiO_2
KFd - Potassium Feldspar - $KAlSi_3O_8$
Plag - Sodium Feldspar - $NaAlSi_3O_8$
Pyr - Pyrite - FeS_2
Sid - Siderite - $FeCO_3$
Kaol - Kaolinite - $Al_2Si_2O_5(OH)_4$
Ill - Illite - $(K,H_3O)Al_2Si_3AlO_{10}(OH)_2$
Chl - Chlorite - $(Mg,Fe,Al)_6(Si,Al)_4O_{10}(OH)_2$
M-L - Mixed Layer
Smec - Smectite
Total Clay - Kaol+Ill+Chr+M-L+Smec

16019 Table A

TABLE B
Comparison of Elemental Composition by EDS and XRD

GR Sample #	Sample ID	H	C	O	Na	Mg	Al	Si	P	S	Cl	K	Ca	Ti	Cr	Mn	Fe	Ni	Cu
GR-001	MC316 321.14 Rust Weathered Surface	-	5.68	48.02	-	0.08	2.61	37.96	0.11	0.04	-	1.27	-	0.20	-	-	3.96	-	0.09
		0.03	0.05	52.54	-	-	0.49	45.34	-	0.53	-	0.30		-	-	-	0.71	-	-

GR-002	MC316 321.14 Grey Weathered Surface	-	20.97	44.20	0.04	0.07	2.05	25.67	0.11	0.05	-	0.96	0.09	0.23	0.06	1.07	4.09	-	0.33
		-	-	53.26	-	-	-	46.74	-	-	-	-	-	-	-	-	-	-	-
GR-003	MC316 321.14 Matrix	-	4.70	48.80	-	0.14	4.21	39.50	-	-	-	2.14	0.05	0.12	-	-	0.27	-	0.08
		0.04	-	53.07	-	-	0.69	45.77	-	-	-	0.44	-	-	-	-	-	-	-
GR-004	SP001 288.8 Grey Weathered Surface	-	17.75	44.54	0.05	0.03	0.76	31.46	-	0.03	0.03	0.21	0.08	0.06	0.29	1.87	2.47	0.10	0.27
		-	-	53.26	-	-	-	46.74	-	-	-	-	-	-	-	-	-	-	-
GR-005	SP001 288.8 Matrix	-	15.31	48.09	-	0.08	1.84	33.73	-	-	-	0.63	-	-	-	-	-	-	0.32
		0.05	-	53.20	-	-	0.73	45.78	-	-	-	0.23	-	-	-	-	-	-	-

H - Hydrogen	Al - Aluminum	K - Potassium	Fe - Iron
C - Carbon	Si - Silicon	Ca - Calcium	Ni - Nickel
O - Oxygen	P - Phosphorus	Ti - Titanium	Cu - Copper
Na - Sodium	S - Sulphur	Cr - Chromium	Black - EDS Analysis
Mg - Magnesium	Cl - Chlorine	Mn - Manganese	Red - Calculated from XRD

16019 Table B

Summary of XRD Results

X-ray diffraction analysis was conducted on samples GR-001 to GR-005. Sample GR-001 consists of 98% silicates (mainly quartz) and minor amounts of iron sulphide and iron carbonate scale. Samples GR-002 and GR-004 are composed of 100% quartz. Samples GR-003 and GR005 both contain 96% quartz and minor amounts of illite and microcline. Sample GR-005 also contains minor amounts of kaolinite.

Comparison of EDS and XRD Results

In many cases the EDS weight percent calculation for some of the elements is different from the XRD weight percent calculation. EDS analysis identifies and quantifies elements present in both crystalline and non-crystalline components. XRD analysis only detects elements in crystalline compounds because only crystalline components of the sample diffract X-rays. Thus our XRD weight percent calculation can only include those elements present in the crystalline compounds. It must be emphasized that each element identified by X-ray diffraction analysis should also be detected by EDS; however, the reverse is not necessarily true.

Table B summarizes the following comments regarding the comparison of EDS and XRD results.

Sample GR-001 showed a moderate-good correlation between the XRD and EDS results. Minor differences with respect to carbon, oxygen, aluminum, silicon and iron were found in sample GR-001.

- Carbon was measured at 5.68% in the elemental analysis, while XRD analysis detected 0.05% carbon.
- In the elemental analysis, oxygen forms 48.02% of the sample, whereas XRD analysis calculated oxygen to be 52.54%.

- Aluminum represents 2.61% in the EDS analysis, while XRD analysis calculated aluminum to be 0.49%.
- Silicon was measured at 37.96% in the elemental analysis, whereas XRD analysis calculated silicon to be 45.34%.
- Iron represents 3.96% in the EDS analysis, while 0.71% iron was detected in XRD analysis.

The EDS results for carbon, aluminum and iron are greater than the XRD results indicating the presence of non-crystalline carbon, aluminum and iron bearing compounds. The XRD results for oxygen and silicon are greater than the EDS results indicating these elements occur in wellcrystalline compounds.

Sample GR-002 showed a moderate-good correlation between the XRD and EDS results.

Significant differences with respect to carbon and silicon were observed in sample GR-002.

- EDS analysis detected 20.97% carbon, whereas XRD analysis did not detect carbon.
- Silicon was measured at 25.67% in the elemental analysis, while 46.74% silicon was detected in XRD analysis.

Minor differences with respect to oxygen, aluminum and iron were noted in sample GR002.

- In the elemental analysis, oxygen forms 44.20% of the sample, whereas XRD analysis calculated oxygen to be 53.26%.
- Aluminum was measured at 2.05% in the elemental analysis, while XRD analysis detected no aluminum.
- In the elemental analysis, iron forms 4.09% of the sample, whereas XRD analysis did not detect iron.

The EDS results for carbon, aluminum and iron are greater than the XRD results indicating the presence of non-crystalline carbon, aluminum and iron bearing compounds. The XRD results for oxygen and silicon are greater than the EDS results indicating these elements occur in wellcrystalline compounds.

Sample GR-003 showed a good correlation between the XRD and EDS results.

Minor differences with respect to carbon, oxygen, aluminum and silicon were found in sample GR-003.

- Carbon represents 4.70% in the EDS analysis, while XRD analysis detected no carbon.
- EDS analysis detected 48.80% oxygen, while 53.07% oxygen was detected in XRD analysis.
- Aluminum was measured at 4.21% in the elemental analysis, while XRD analysis calculated aluminum to be 0.69%.
- Silicon represents 39.50% in the EDS analysis, while XRD analysis detected 45.77% silicon.

The EDS results for carbon and aluminum are greater than the XRD results indicating the presence of non-crystalline carbon and aluminum bearing compounds. The XRD results for oxygen and silicon are greater than the EDS results indicating these elements occur in wellcrystalline compounds.

Sample GR-004 showed a good correlation between the XRD and EDS results.

Moderate differences with respect to carbon and silicon were noted in sample GR-004.

- Carbon was measured at 17.75% in the elemental analysis, while XRD analysis did not detect carbon.
- EDS analysis detected 31.46% silicon, while 46.74% silicon was detected in XRD analysis.

Minor differences with respect to oxygen and iron were noted in sample GR-004.

- In the elemental analysis, oxygen forms 44.54% of the sample, whereas XRD analysis calculated oxygen to be 53.26%.
- Iron represents 2.47% in the EDS analysis, while no iron was detected in XRD analysis. The EDS results for carbon and iron are greater than the XRD results indicating the presence of non-crystalline carbon and iron bearing compounds. The XRD results for oxygen and silicon are greater than the EDS results indicating these elements occur in well-crystalline compounds.

Sample GR-005 showed a good correlation between the XRD and EDS results.

Moderate differences with respect to carbon and silicon were observed in sample GR-005.

- In the elemental analysis, carbon forms 15.31% of the sample, while XRD analysis did not detect carbon.
- EDS analysis detected 33.73% silicon, while XRD analysis detected 45.78% silicon.

A minor difference with respect to oxygen was observed in sample GR-005.

- In the elemental analysis, oxygen forms 48.09% of the sample, whereas XRD analysis calculated oxygen to be 53.20%.

The EDS result for carbon is greater than the XRD result indicating the presence of noncrystalline carbon bearing compounds. The XRD results for oxygen and silicon are greater than the EDS results indicating these elements occur in well-crystalline compounds.

GR Petrology usually mounts a ground sample on a glass slide for X-ray diffraction analysis. The X-ray beam scans an area of approximately 250mm^2; however, the electron beam in the EDS that generates the elemental analysis scans a much smaller area of approximately 6mm^2. We attempted to obtain the elemental analysis from the most representative area of the sample; however, the irregular distribution of the materials in the sample may have skewed the EDS results in some instances.

Apparent differences in the elemental weigh percent calculation of the above-mentioned elements are a function of:

1) The presence of non-crystalline components in the sample.
2) The difference in the area analysed by both methods.

Sample ID: MC316 321.14 Rust Weathered Surface

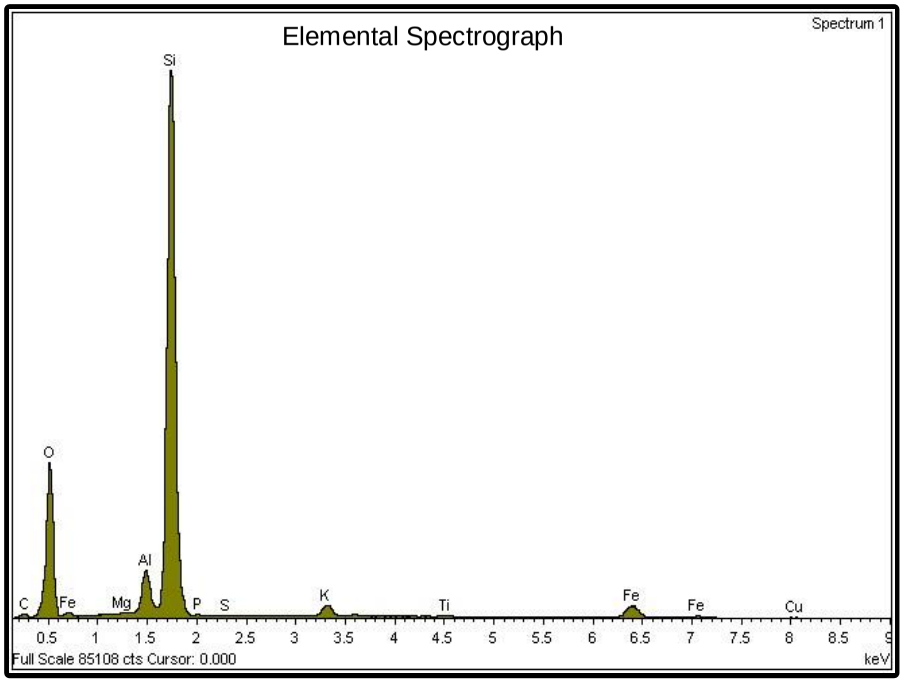

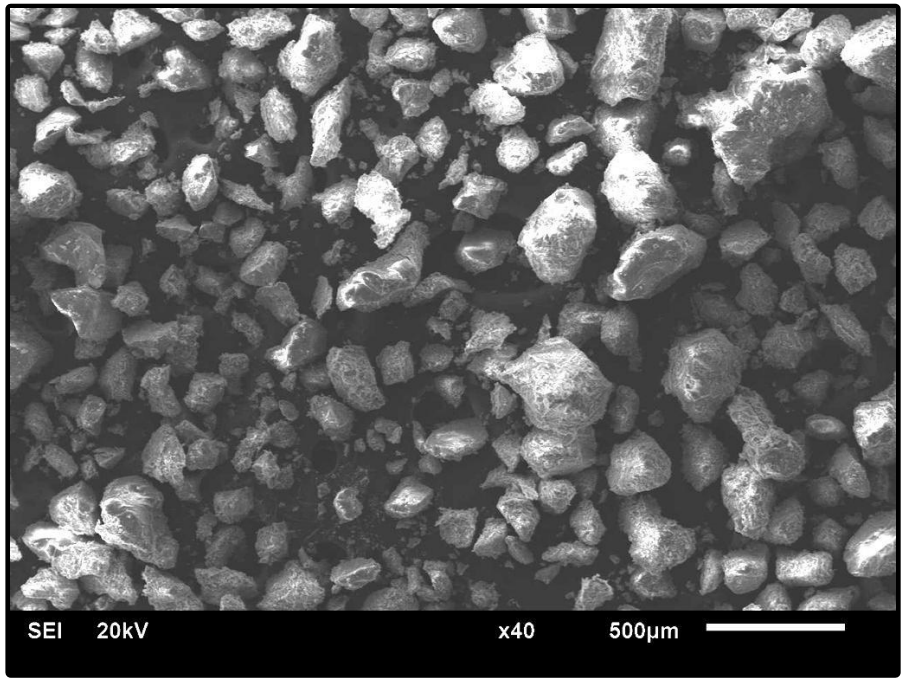

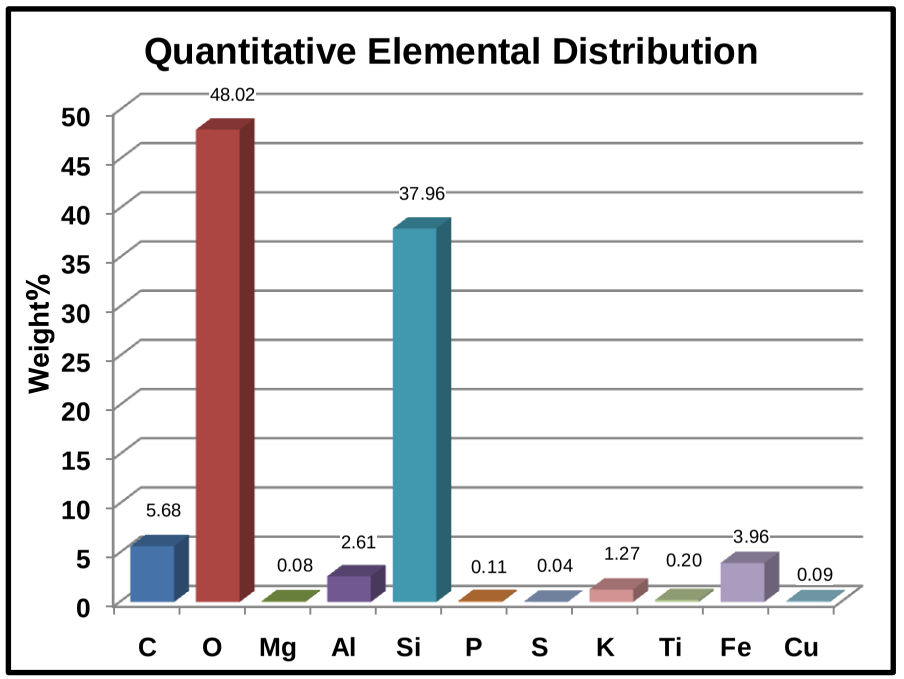

Description of Samples

GR-001: MC316 321.14 Rust Weathered Surface

The scanning electron photomicrograph on the facing page (lower left) shows sample GR-001 consists of angular, subangular and subrounded, very fine sand size to medium sand size particles. The upper left photograph illustrates the bulk sample.

Oxygen (O) and silicon (Si) dominate the elemental spectrograph, respectively forming about 48.0% and 38.0% of the sample. Carbon (C), aluminum (Al) and iron (Fe) are moderately abundant, respectively forming about 5.7%, 2.6% and 4.0% of the sample. Trace to minor amounts of magnesium (Mg), phosphorus (P), sulphur (S), potassium (K), titanium (Ti) and copper (Cu) are present.

The sample generated a good quality diffractogram indicating the sample is mainly composed of crystalline compounds. X-ray diffraction analysis shows the crystalline components of the sample consist of about 98% silicates **(quartz [SiO_2]**, **illite-2m1 (nr) [$(K,H_3O)Al_2Si_3AlO_{10}(OH)_2$]** and **microcline [$KAlSi_3O_8$])**, 1% iron sulphide scale or corrosion products **(pyrite [FeS_2])** and 1% iron carbonate scale **(siderite [$FeCO_3$])**.

Elemental analysis also suggests the presence of non-crystalline carbon, aluminum and iron bearing compounds. Trace volumes of magnesium, phosphorus, titanium and copper bearing compounds were detected during elemental analysis.

TABLE 1: EDS and XRD Results
University of Saskatchewan; Sample ID: MC316 321.14 Rust Weathered Surface
GR 16019-01 2010

ELEMENTS:

DOMINANT: O, Si **MODERATE:** C, Al, Fe

COMMON: **MINOR-TRACE:** Mg, P, S, K, Ti, Cu

COMPOUNDS:

Formula	*Name*	*Percentage*
SiO_2	Quartz	95.6%
$(K,H_3O)Al_2Si_3AlO_{10}(OH)_2$	Illite-2M1 (NR)	2.2%
$KAlSi_3O_8$	Microcline	0.7%
FeS_2	Pyrite	1.0%
$FeCO_3$	Siderite	0.5%
		100.0%

COMMENTS:

The sample generated a good quality diffractogram indicating the sample is mainly composed of crystalline compounds. X-ray diffraction analysis shows the crystalline components of the sample mainly consist of silicates (about 98%). Iron sulphide scale or corrosion products and iron carbonate scale occur in minor amounts. Elemental analysis also suggests the presence of non-crystalline carbon, aluminum and iron bearing compounds. Trace volumes of magnesium, phosphorus, titanium and copper bearing compounds were detected during elemental analysis.

ABUNDANCE OF COMPOUNDS

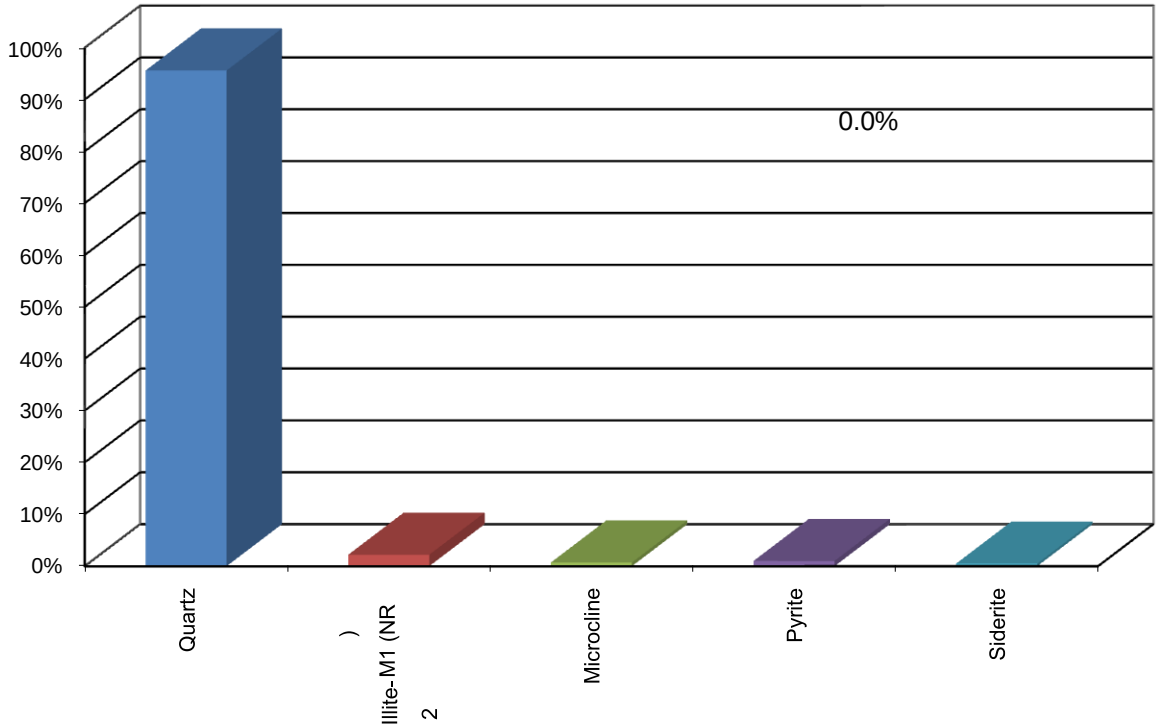
100%
90%
80%
70%
60%
50%
40%
30%
20%
10%
0%
0.0%
Quartz
)
Illite-M1 (NR
2
Microcline
Pyrite
Siderite

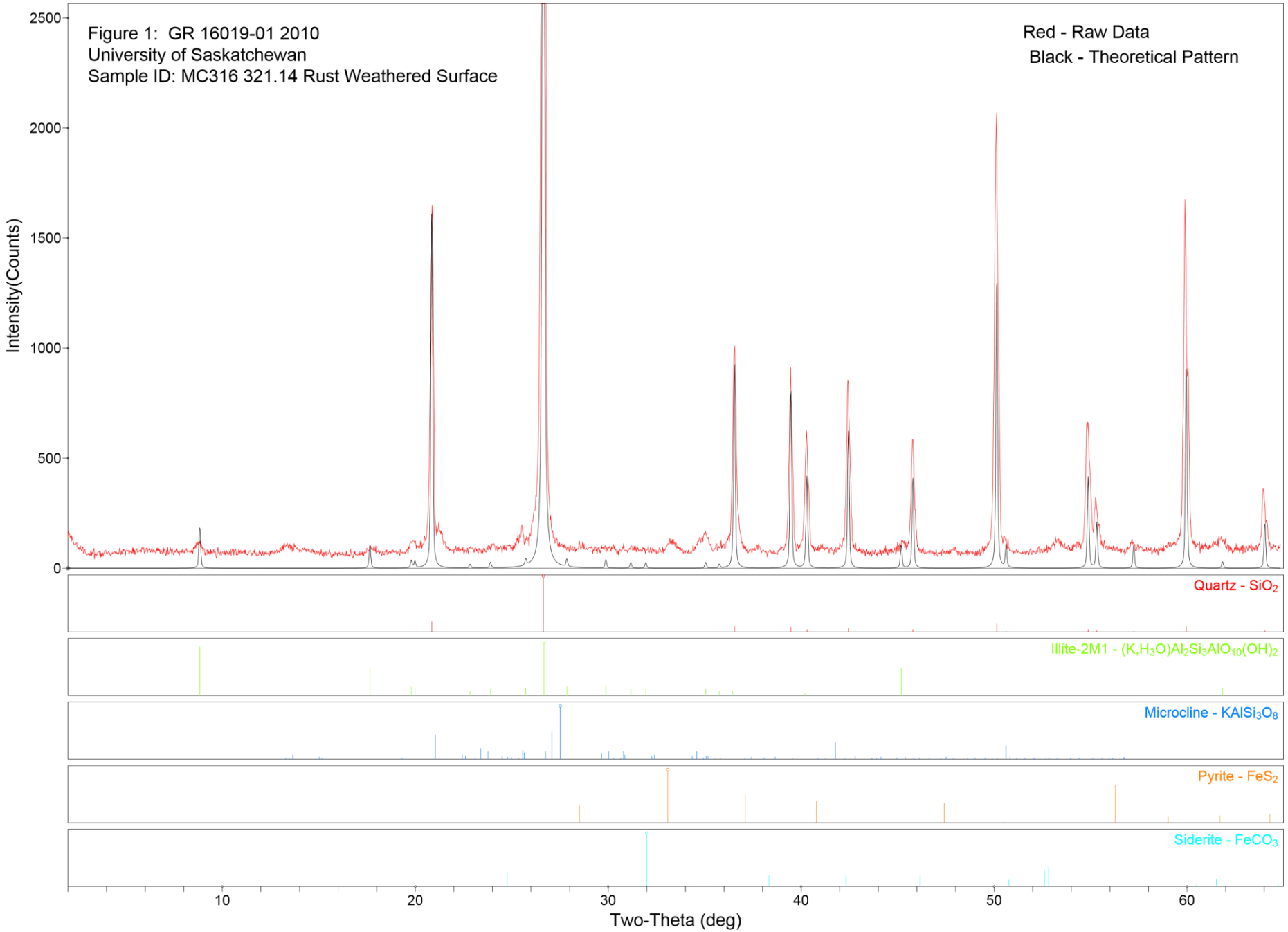
Figure 1: GR 16019-01 2010
University of Saskatchewan
Sample ID: MC316 321.14 Rust Weathered Surface
Red - Raw Data
Black - Theoretical Pattern
Intensity(Counts)
2500
2000
1500
1000
500
0
Quartz - SiO2
Illite-2M1 - (K,H3O)Al2Si3AlO10(OH)2
Microcline - KAlSi3O8
Pyrite - FeS2
Siderite - FeCO3
10
20
30
40
50
60
Two-Theta (deg)

Sample ID: MC316 321.14 Grey Weathered Surface

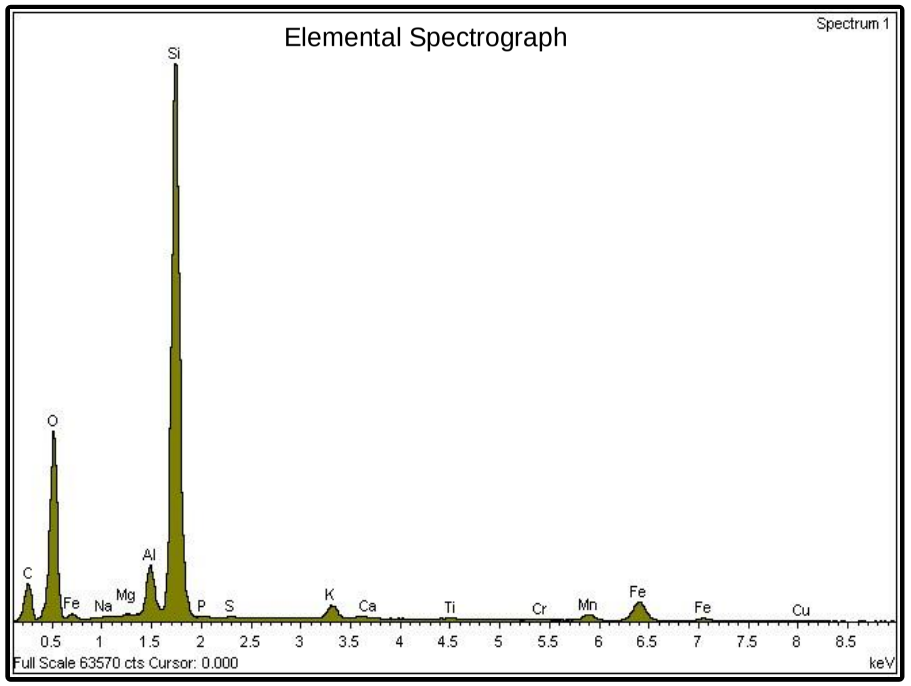

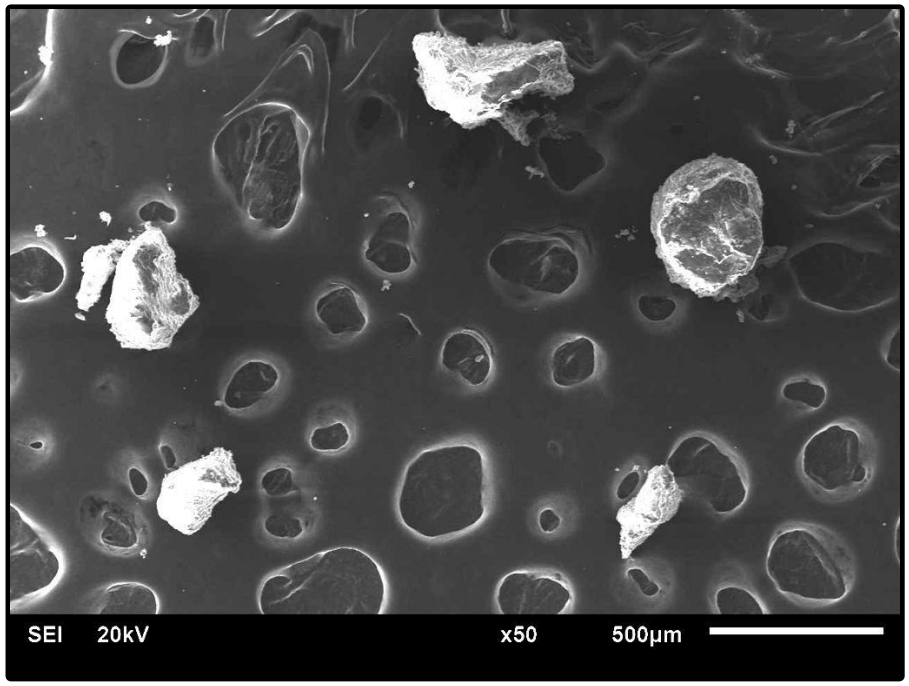

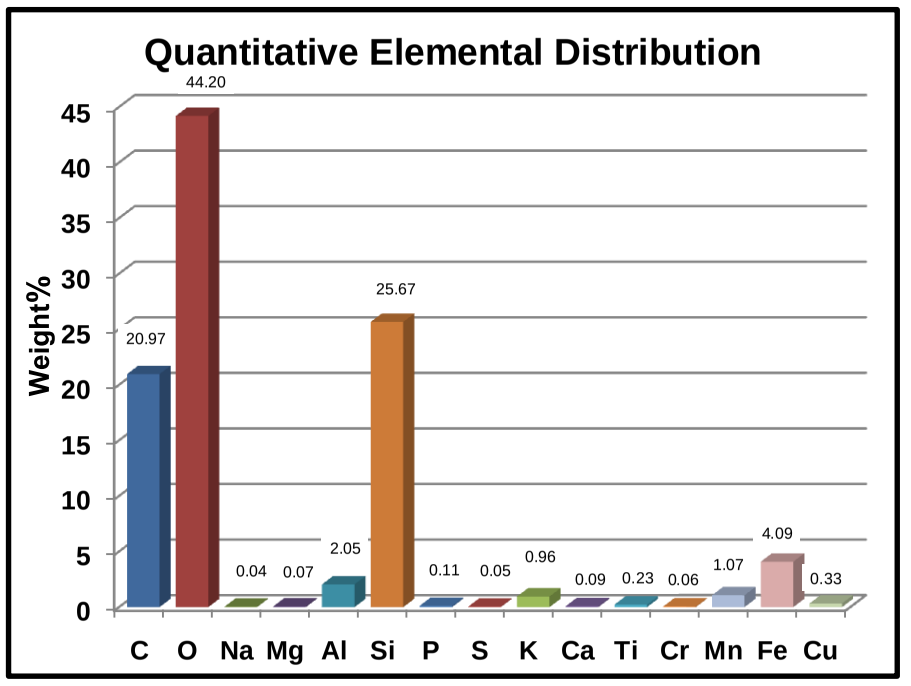

GR-002: MC316 321.14 Grey Weathered Surface

The scanning electron photomicrograph on the facing page (lower left) shows sample GR-002 consists of angular, subangular and subrounded, very fine sand size to medium sand size particles. The upper left photograph illustrates the bulk sample.

Carbon (C), oxygen (O) and silicon (Si) dominate the elemental spectrograph, respectively forming about 21.0%, 44.2% and 25.7% of the sample. Aluminum (Al) and iron (Fe) are moderately abundant, respectively forming about 2.1% and 4.1% of the sample. Trace to minor amounts of sodium (Na), magnesium (Mg), phosphorus (P), sulphur (S), potassium (K), calcium (Ca), titanium (Ti), chromium (Cr), manganese (Mn) and copper (Cu) are present.

The sample generated a moderate quality diffractogram indicating the sample is composed of both crystalline and non-crystalline compounds. X-ray diffraction analysis shows the crystalline components of the sample consist of 100% silicates **(quartz [SiO_2])**.

Elemental analysis also suggests the presence of non-crystalline carbon, aluminum and iron bearing compounds. Trace to minor volumes of sodium, magnesium, aluminum, phosphorus, sulphur, potassium, calcium, titanium, chromium, manganese, iron and copper bearing compounds were detected during elemental analysis.

TABLE 2: EDS and XRD Results
University of Saskatchewan; Sample ID: MC316 321.14 Grey Weathered Surface
GR 16019-02 2010

ELEMENTS:

DOMINANT: C, O, Si

MODERATE: Al, Fe

COMMON:

MINOR-TRACE: Na, Mg, P, S, K, Ca, Ti, Cr, Mn, Cu

COMPOUNDS:

Formula	*Name*	*Percentage*
SiO_2	Quartz	100.0%
		100.0%

COMMENTS:

The sample generated a moderate quality diffractogram indicating the sample is composed of both crystalline and non-crystalline compounds. X-ray diffraction analysis shows the crystalline components of the sample consist of 100% silicates. Elemental analysis also suggests the presence of non-crystalline carbon, aluminum and iron bearing compounds. Trace to minor volumes of sodium, magnesium, aluminum, phosphorus, sulphur, potassium, calcium, titanium, chromium, manganese, iron and copper bearing compounds were detected during elemental analysis.

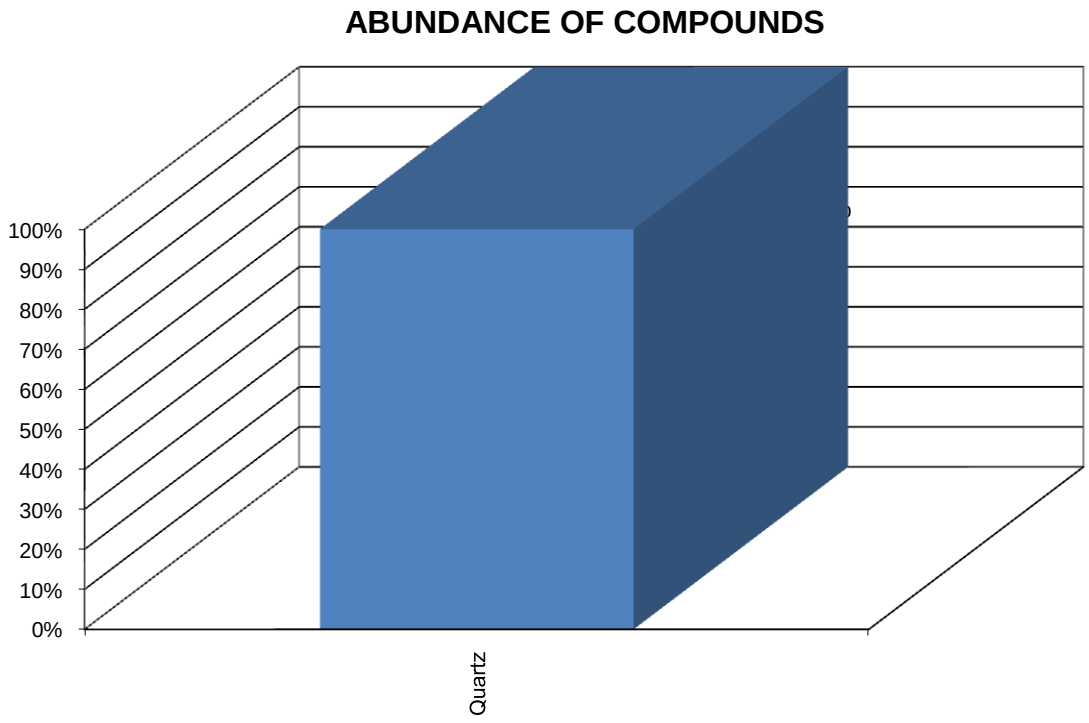

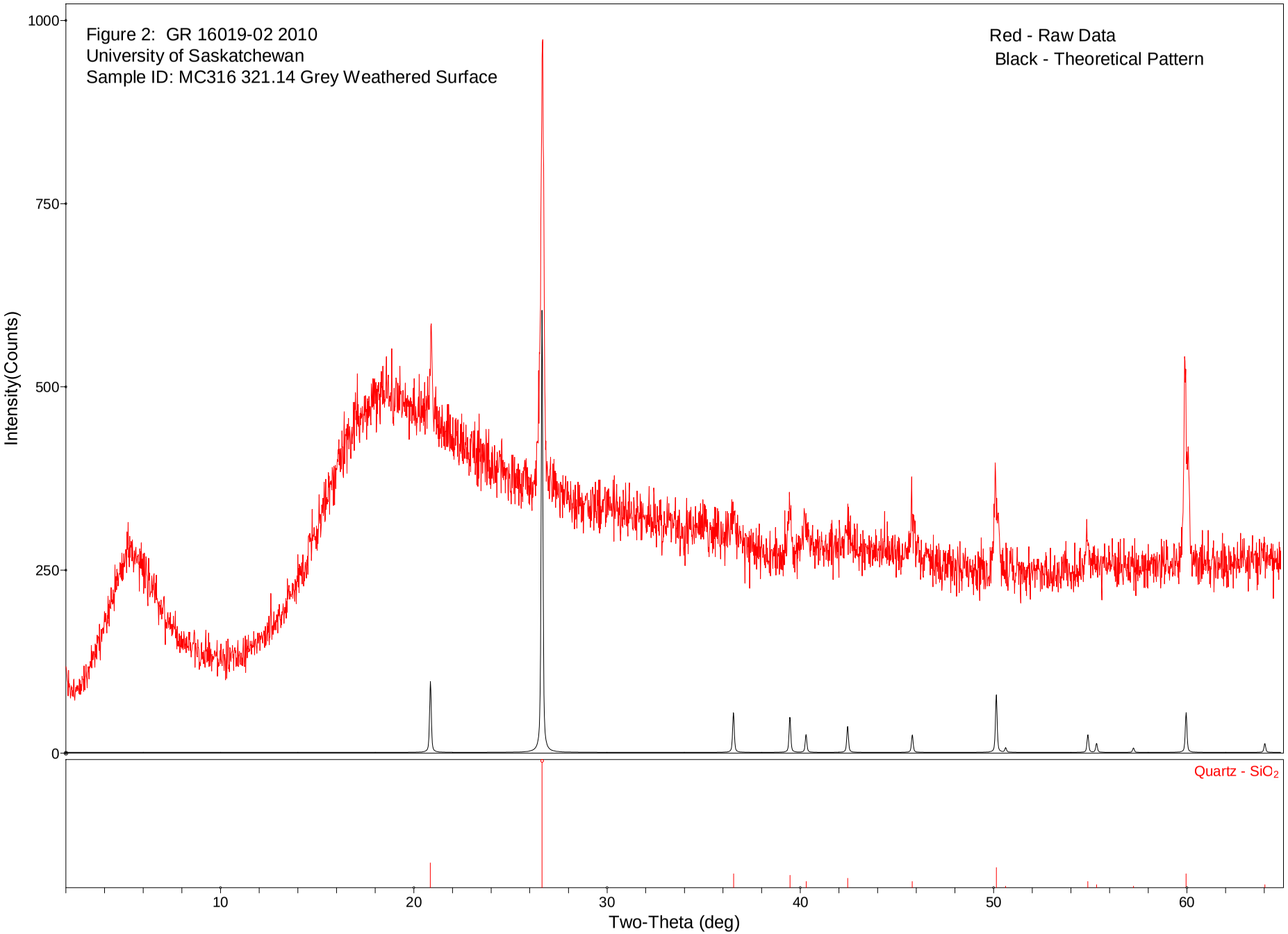
Figure 2: GR 16019-02 2010
University of Saskatchewan
Sample ID: MC316 321.14 Grey Weathered Surface
Red - Raw Data
Black - Theoretical Pattern
Intensity(Counts)
1000
750
500
250
0
Quartz - SiO2
10
20
30
40
50
60
Two-Theta (deg)

Sample ID: MC316 321.14 Matrix

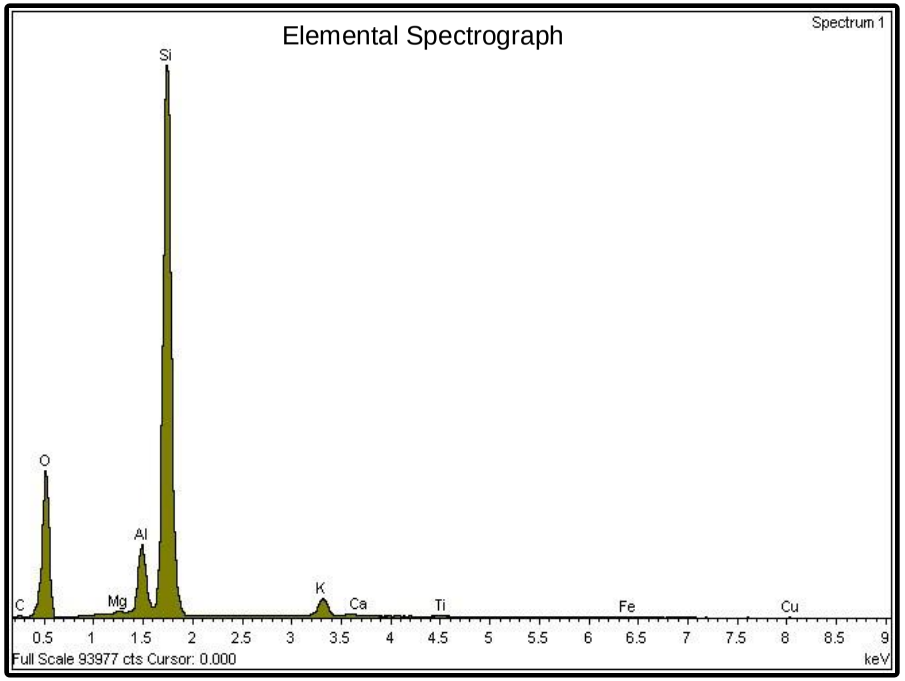

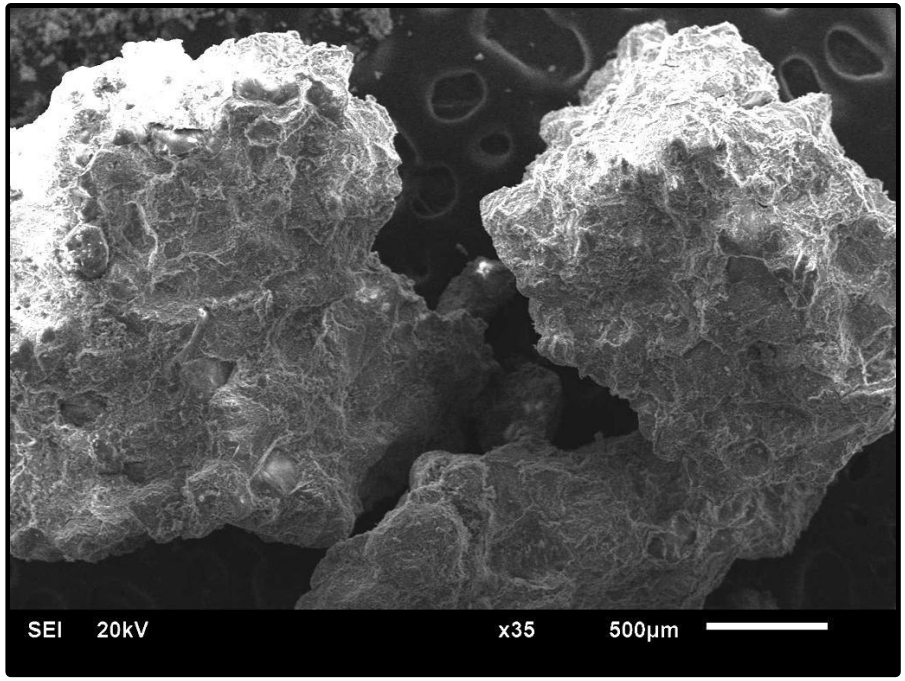

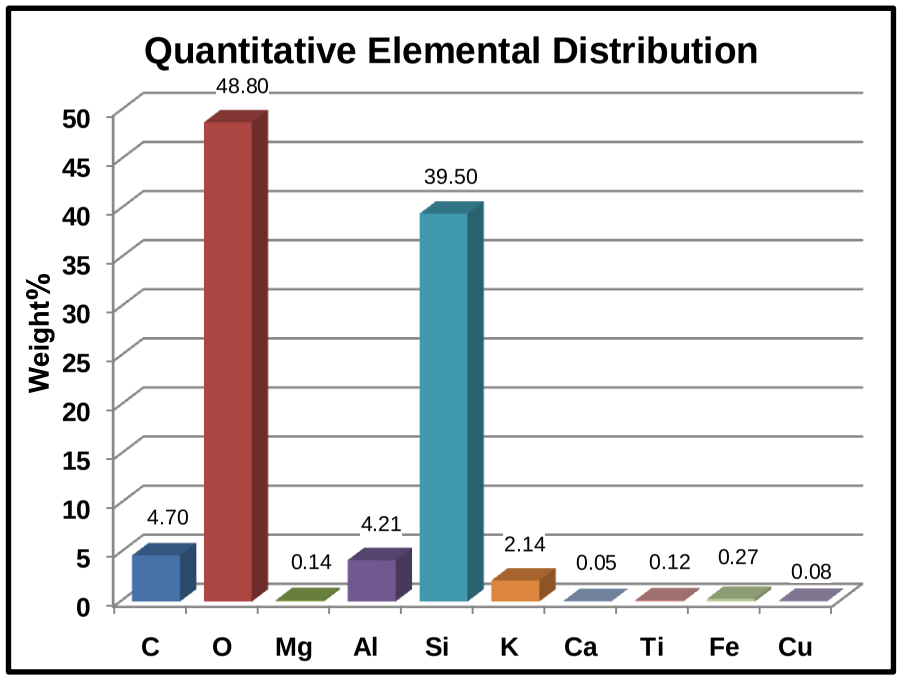

GR-003: MC316 321.14 Matrix

The scanning electron photomicrograph on the facing page (lower left) shows sample GR-003 consists of aggregates of angular, subangular and subrounded, very fine sand size to medium sand size particles. The upper left photograph illustrates the bulk sample.

Oxygen (O) and silicon (Si) dominate the elemental spectrograph, respectively forming about 48.8% and 39.5% of the sample. Carbon (C), aluminum (Al) and potassium (K) are moderately abundant, respectively forming about 4.7%, 4.2% and 2.1% of the sample. Trace to minor amounts of magnesium (Mg), calcium (Ca), titanium (Ti), iron (Fe) and copper (Cu) are present.

The sample generated a good quality diffractogram indicating the sample is mainly composed of crystalline compounds. X-ray diffraction analysis shows the crystalline components of the sample consist of 100% silicates **(quartz [SiO_2]**, **illite-2m1 (nr) [$(K,H_3O)Al_2Si_3AlO_{10}(OH)_2$]** and **microcline [$KAlSi_3O_8$])**.

Elemental analysis also suggests the presence of non-crystalline carbon and aluminum bearing compounds. Trace to minor volumes of carbon, magnesium, calcium, titanium, iron and copper bearing compounds were detected during elemental analysis.

TABLE 3: EDS and XRD Results
University of Saskatchewan; Sample ID: MC316 321.14 Matrix
GR 16019-03 2010

ELEMENTS:

DOMINANT: O, Si

MODERATE: C, Al, K

COMMON:

MINOR-TRACE: Mg, Ca, Ti, Fe, Cu

COMPOUNDS:

Formula	*Name*	*Percentage*
SiO_2	Quartz	95.9%
$(K,H_3O)Al_2Si_3AlO_{10}(OH)_2$	Illite-2M1 (NR)	3.0%
$KAlSi_3O_8$	Microcline	1.1%
		100.0%

COMMENTS:

The sample generated a good quality diffractogram indicating the sample is mainly composed of crystalline compounds. X-ray diffraction analysis shows the crystalline components of the sample consist of 100% silicates. Elemental analysis also suggests the presence of non-crystalline carbon and aluminum bearing compounds. Trace to minor volumes of magnesium, calcium, titanium, iron and copper bearing compounds were detected during elemental analysis.

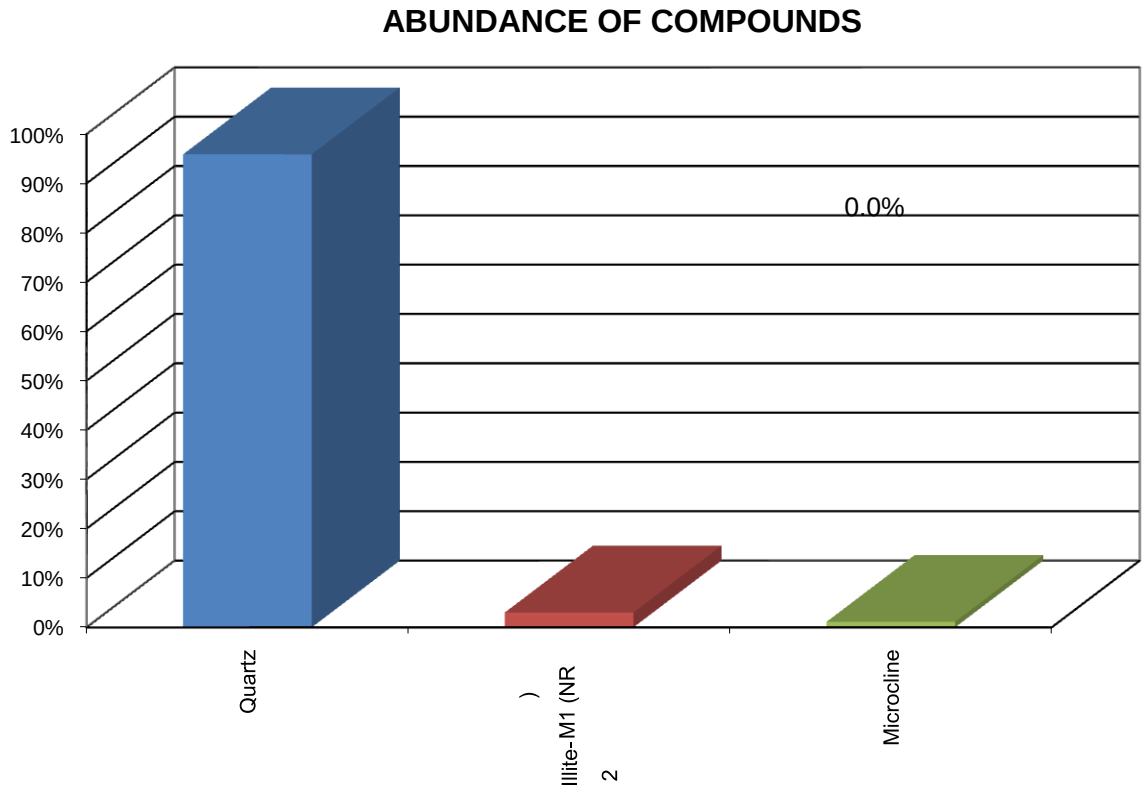

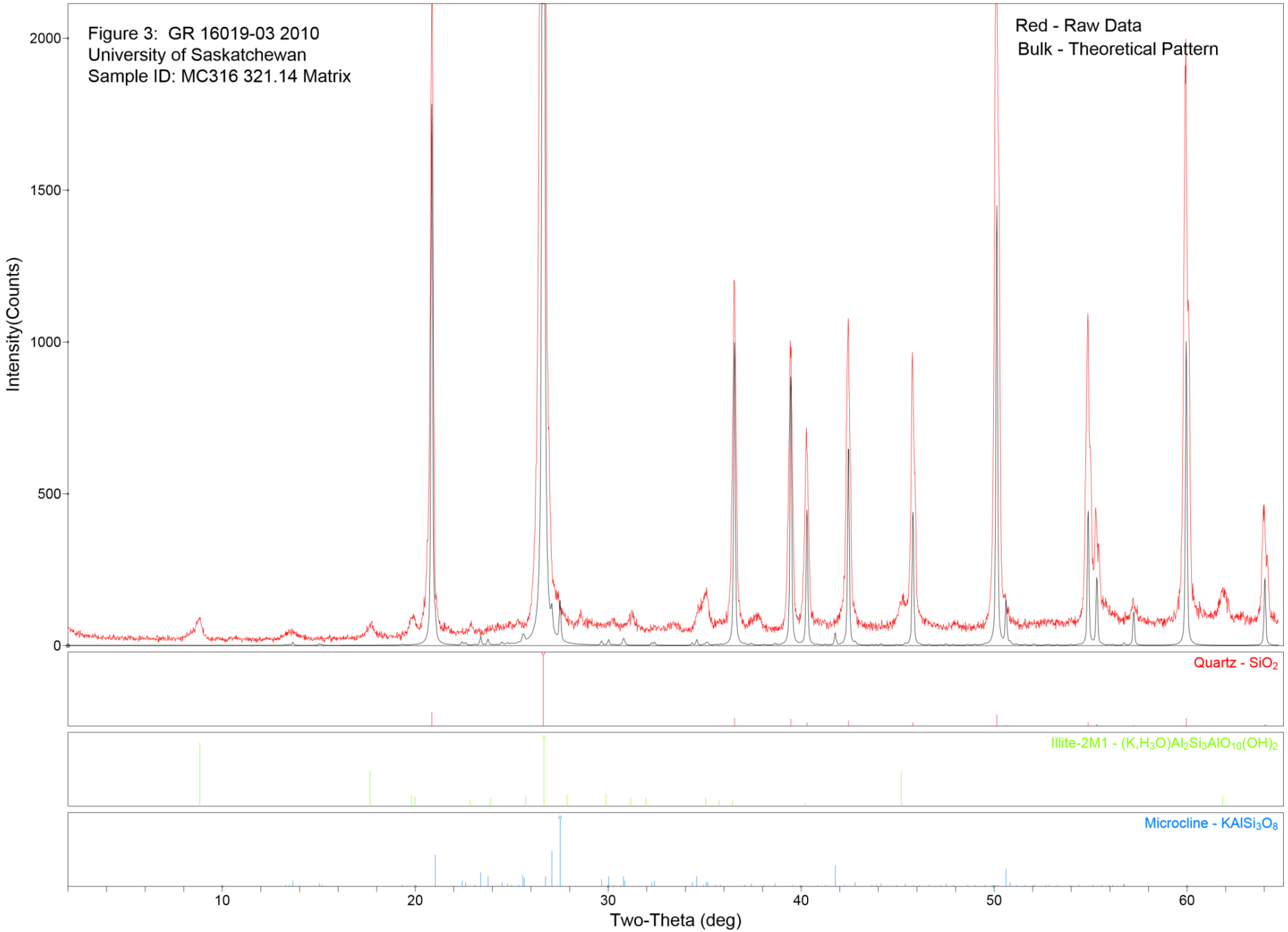
Figure 3: GR 16019-03 2010
University of Saskatchewan
Sample ID: MC316 321.14 Matrix
Red - Raw Data
Bulk - Theoretical Pattern
Intensity(Counts)
2000
1500
1000
500
0
Quartz - SiO2
Illite-2M1 - (K,H3O)Al2Si3AlO10(OH)2
Microcline - KAlSi3O8
10
20
30
40
50
60
Two-Theta (deg)

Sample ID: SP001 288.8 Grey Weathered Surface

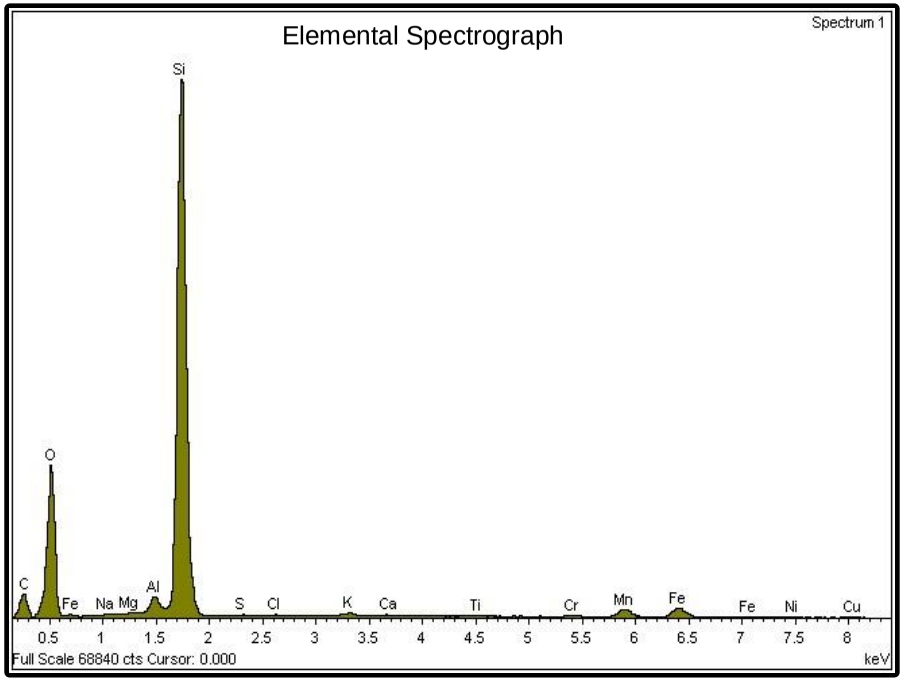

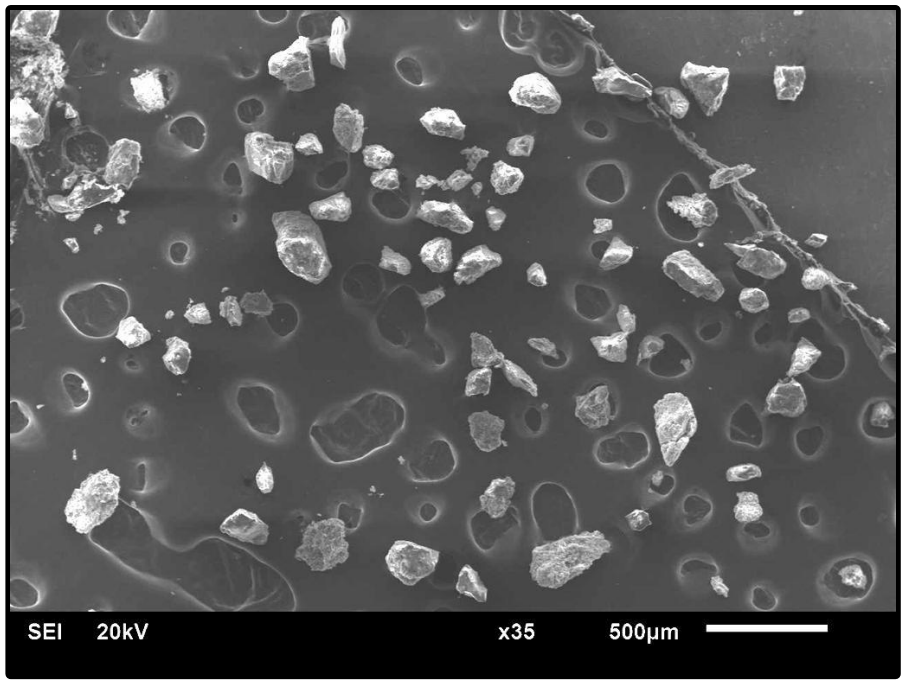

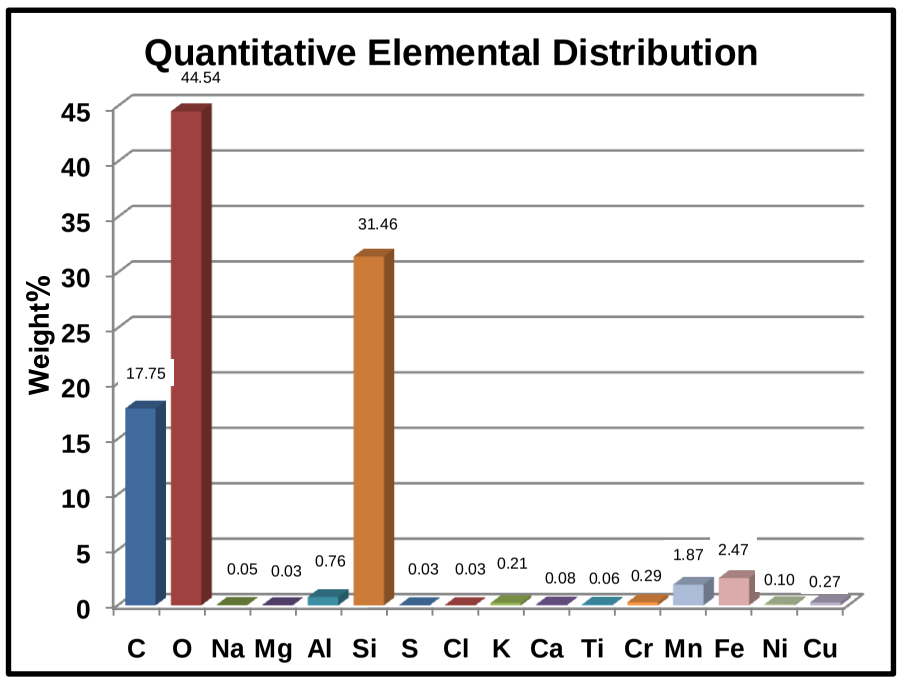

GR-004: SP001 288.8 Grey Weathered Surface

The scanning electron photomicrograph on the facing page (lower left) shows sample GR-004 consists of angular, subangular and subrounded, coarse silt size to medium sand size particles The upper left photograph illustrates the bulk sample.

Oxygen (O) and silicon (Si) dominate the elemental spectrograph, respectively forming about 44.5% and 31.5% of the sample. Carbon (C) is common, forming about 17.8% of the sample. Iron (Fe) is moderately abundant, forming about 2.5% of the sample. Trace to minor amounts of sodium (Na), magnesium (Mg), aluminum (Al), sulphur (S), chlorine (Cl), potassium (K), calcium (Ca), titanium (Ti), chromium (Cr), manganese (Mn), nickel (Ni) and copper (Cu) are present.

The sample generated a moderate quality diffractogram indicating the sample is composed of both crystalline and non-crystalline compounds. X-ray diffraction analysis shows the crystalline components of the sample consist of 100% silicates **(quartz [SiO_2])**.

Elemental analysis also suggests the presence of non-crystalline carbon and iron bearing compounds. Moderate volumes of carbon bearing compounds, as well as trace to minor volumes of sodium, magnesium, aluminum, sulphur, chlorine, potassium, calcium, titanium, chromium, manganese, iron, nickel and copper bearing compounds were detected during elemental analysis.

TABLE 4: EDS and XRD Results
University of Saskatchewan; Sample ID: SP001 288.8 Grey Weathered Surface GR 16019-04 2010

ELEMENTS:

DOMINANT: O, Si

MODERATE: Fe

COMMON: C

MINOR-TRACE: Na, Mg, Al, S, Cl, K, Ca, Ti, Cr, Mn, Ni, Cu

COMPOUNDS:

Formula	*Name*	*Percentage*
SiO_2	**Quartz**	**100.0%**
		100.0%

COMMENTS:

The sample generated a moderate quality diffractogram indicating the sample is composed of both crystalline and non-crystalline compounds. X-ray diffraction analysis shows the crystalline components of the sample consist of 100% silicates. Elemental analysis also suggests the presence of non-crystalline carbon and iron bearing compounds. Trace to minor volumes of sodium, magnesium, aluminum, sulphur, chlorine, potassium, calcium, titanium, chromium, manganese, iron, nickel and copper bearing compounds were detected during elemental analysis.

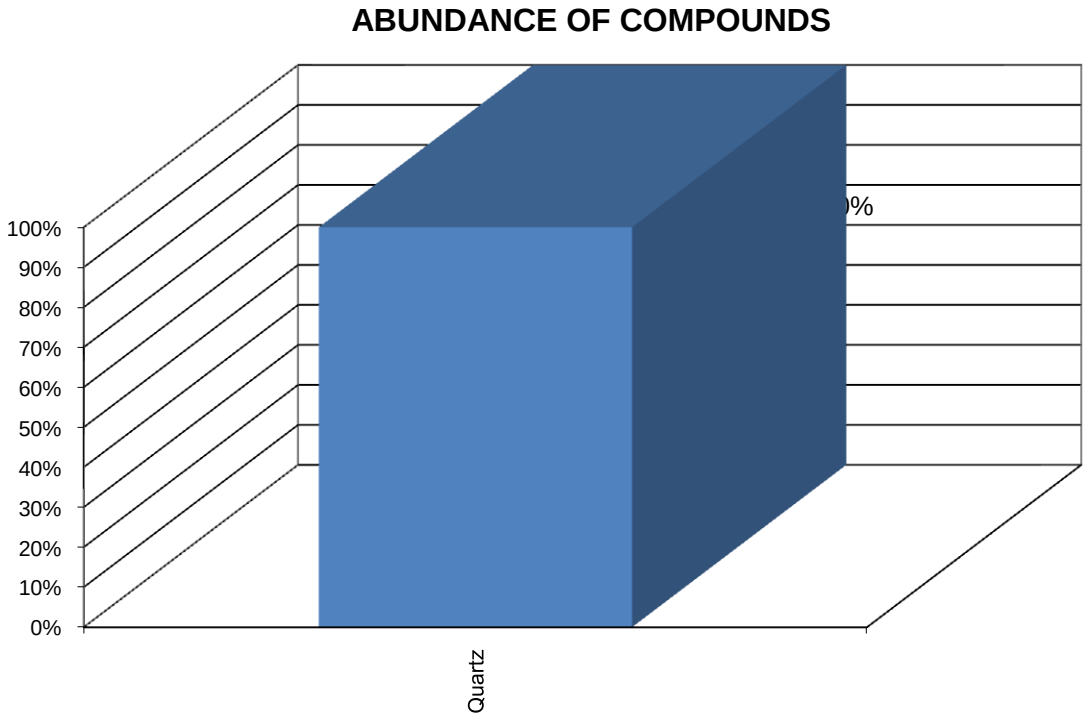

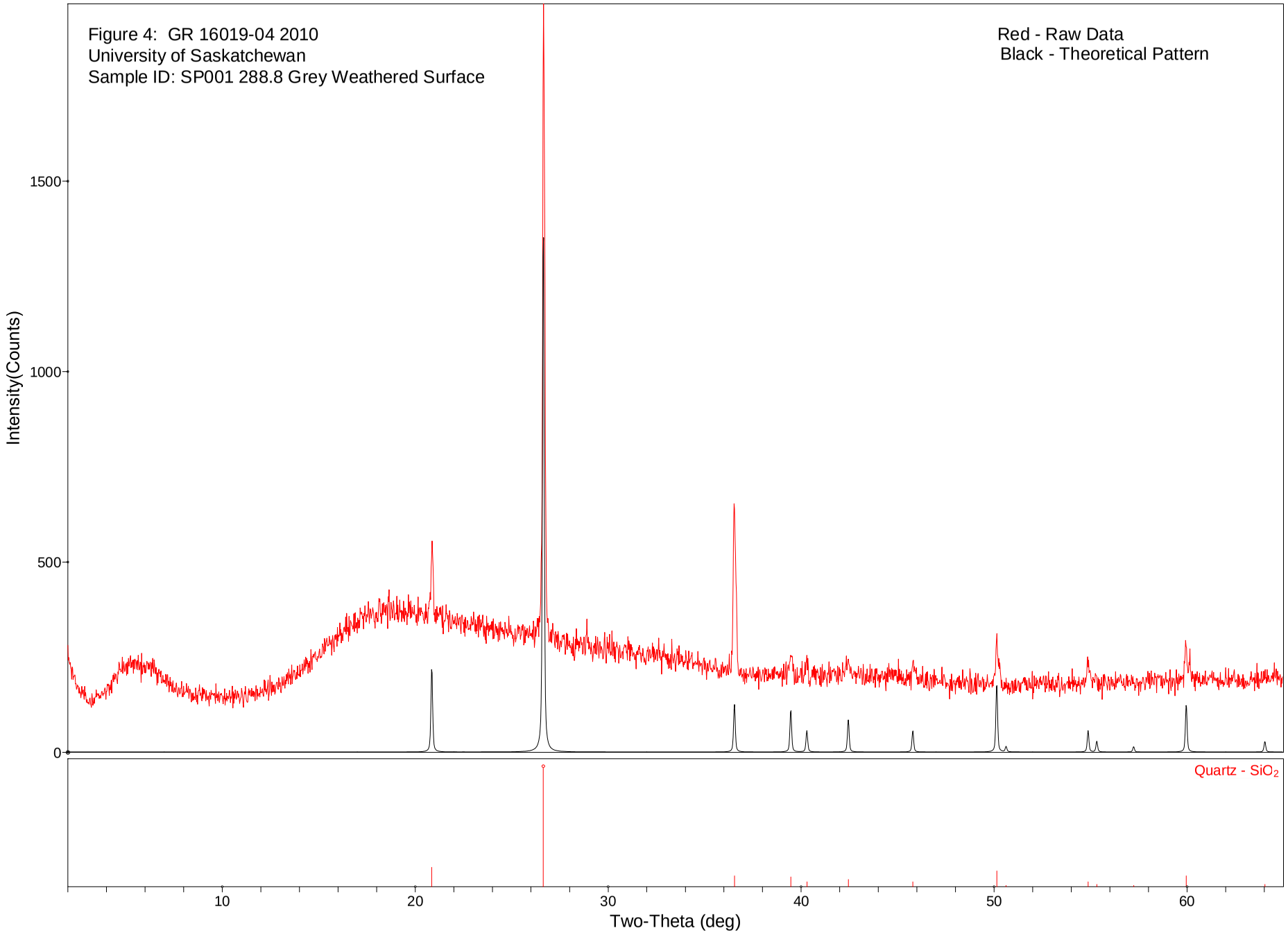
Figure 4: GR 16019-04 2010
University of Saskatchewan
Sample ID: SP001 288.8 Grey Weathered Surface
Red - Raw Data
Black - Theoretical Pattern
Intensity(Counts)
1500
1000
500
0
Quartz - SiO2
10
20
30
40
50
60
Two-Theta (deg)

Sample ID: SP001 288.8 Matrix

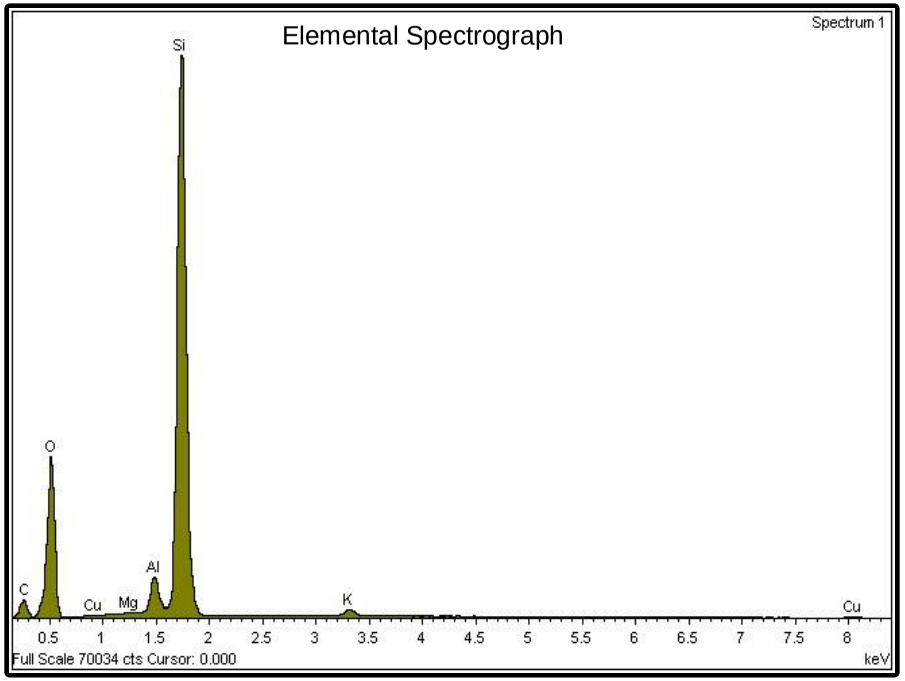

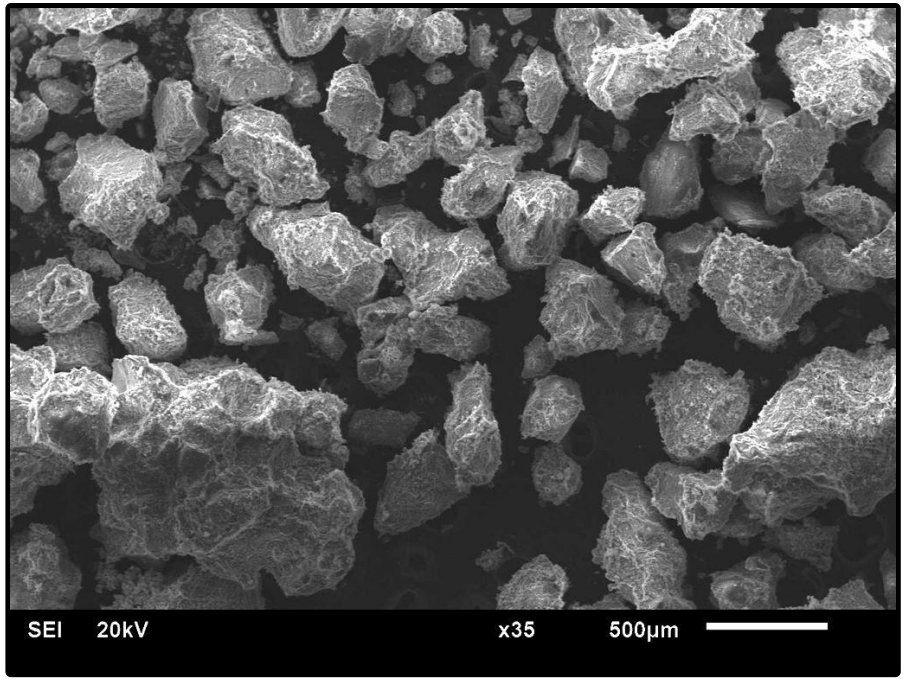

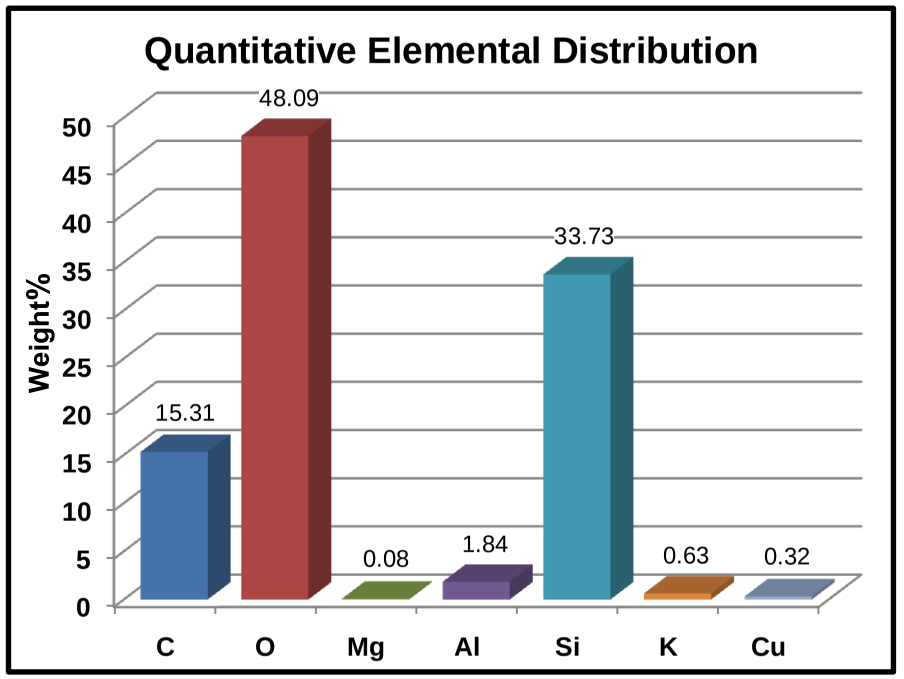

GR-005: SP001 288.8 Matrix

The scanning electron photomicrograph on the facing page (lower left) shows sample GR-005 consists of angular and subangular, coarse silt size to coarse sand size particles. The upper left photograph illustrates the bulk sample.

Oxygen (O) and silicon (Si) dominate the elemental spectrograph, respectively forming about 48.1% and 33.7% of the sample. Carbon (C) is common, forming about 15.3% of the sample. Trace to minor amounts of magnesium (Mg), aluminum (Al), potassium (K) and copper (Cu) are present.

The sample generated a good quality diffractogram indicating the sample is mainly composed of crystalline compounds. X-ray diffraction analysis shows the crystalline components of the sample consist of 100% silicates **(quartz [SiO_2]**, **kaolinite [$Al_2Si_2O_5(OH)_4$]**, **illite-2m1 (nr) [$(K,H_3O)Al_2Si_3AlO_{10}(OH)_2$]** and **microcline [$KAlSi_3O_8$])**.

Elemental analysis also suggests the presence of non-crystalline carbon bearing compounds. Moderate volumes of carbon bearing compounds, as well as trace volumes of magnesium and copper bearing compounds were detected during elemental analysis.

TABLE 5: EDS and XRD Results
University of Saskatchewan; Sample ID: SP001 288.8 Matrix
GR 16019-05 2010

ELEMENTS:

DOMINANT: O, Si
MODERATE:
COMMON: C
MINOR-TRACE: Mg, Al, K, Cu

COMPOUNDS:

Formula	*Name*	*Percentage*
SiO_2	Quartz	96.1%
$Al_2Si_2O_5(OH)_4$	Kaolinite	1.7%
$(K,H_3O)Al_2Si_3AlO_{10}(OH)_2$	Illite-2M1 (NR)	1.7%
$KAlSi_3O_8$	Microcline	0.5%
		100.0%

COMMENTS:

The sample generated a good quality diffractogram indicating the sample is mainly composed of crystalline compounds. X-ray diffraction analysis shows the crystalline components of the sample consist of 100% silicates. Elemental analysis also suggests the presence of non-crystalline carbon bearing compounds. Trace volumes of magnesium and copper bearing compounds were detected during elemental analysis.

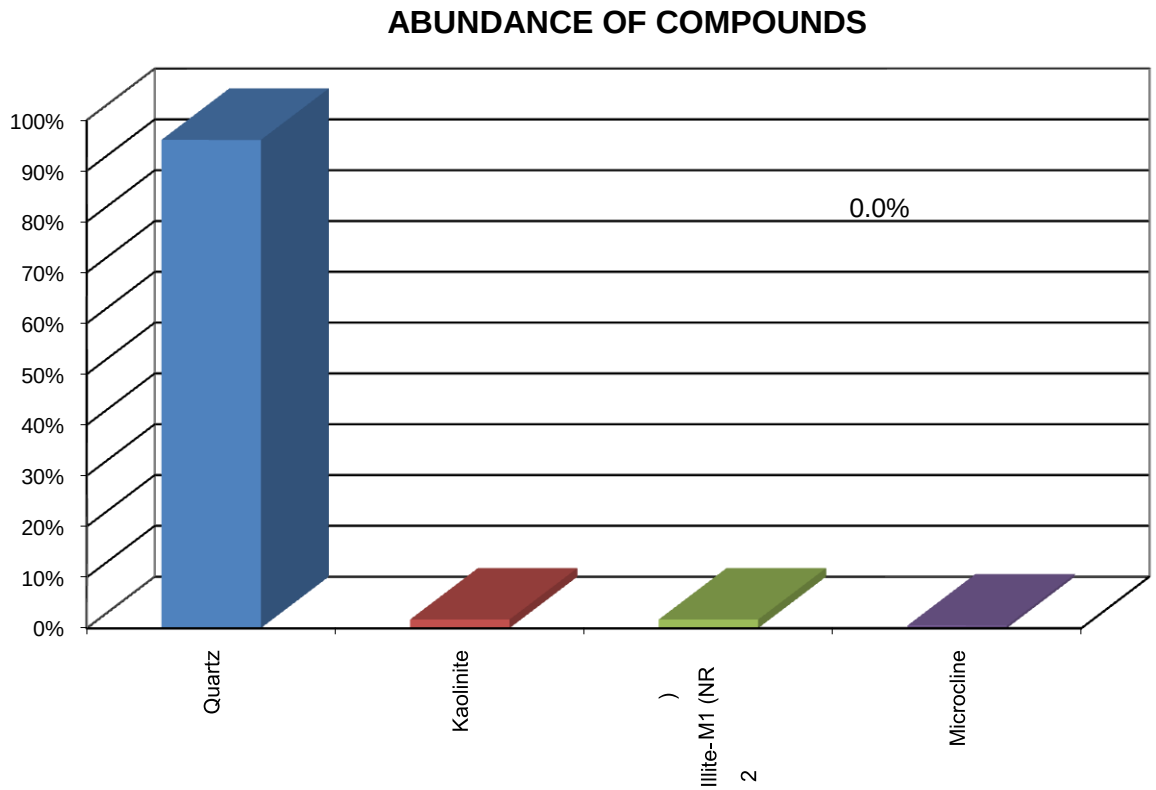

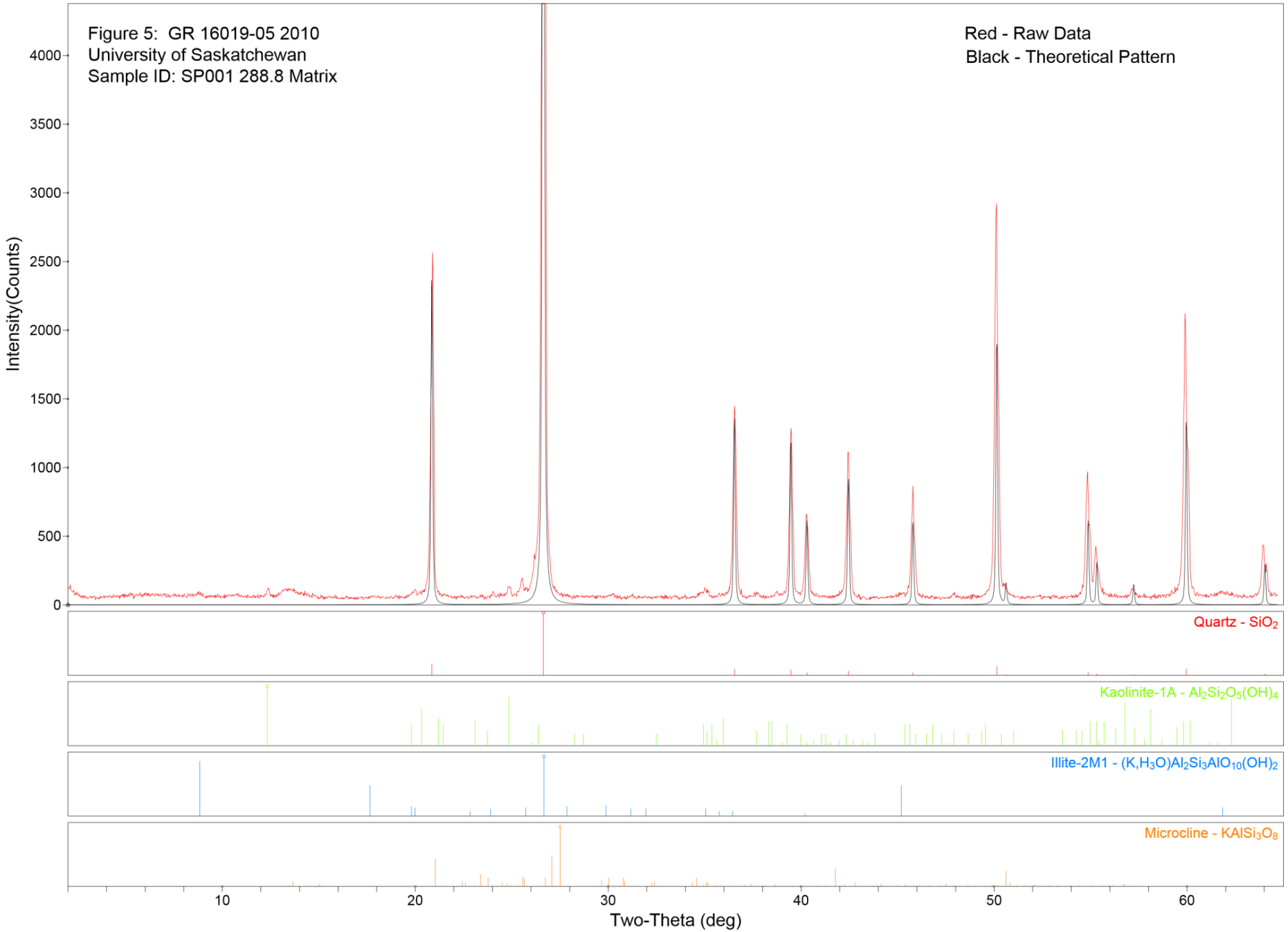
Figure 5: GR 16019-05 2010
University of Saskatchewan
Sample ID: SP001 288.8 Matrix
Red - Raw Data
Black - Theoretical Pattern
Intensity(Counts)
4000
3500
3000
2500
2000
1500
1000
500
0
Quartz - SiO_2
Kaolinite-1A - $Al_2Si_2O_5(OH)_4$
Illite-2M1 - $(K,H_3O)Al_2Si_3AlO_{10}(OH)_2$
Microcline - $KAlSi_3O_8$
10
20
30
40
50
60
Two-Theta (deg)

Elemental Analysis and Thin Section Photography

of

Two Solid Samples

for

University of Saskatchewan

GR 16019 2011

GR Petrology Consultants Inc.
Suite 8, 1323 – 44th Avenue N.E.
Calgary, Alberta T2E 6L5
Tel: 403-291-3420 Fax: 403-250-7212
E-mail: francis.dunlop@grpetrology.com

January 2011

Elemental Analysis and Thin Section Photography of Two Solid Samples
University of Saskatchewan

Summary of Analyses

Two solid samples were submitted for Elemental Analysis by EDS and Thin Section Photography and Description.

Quantitative elemental analysis was performed by an **Oxford INCA** microanalysis system attached to a **JEOL JSM-6610** scanning electron microscope. The INCA system was designed to obtain standardless quantitative elemental analysis from rough samples by SEM. The INCA system has enhanced light element capabilities, and is able to identify beryllium (Be), and quantify boron (B), and carbon (C).

The following Tables and Plates are included in this report:

- Table C: Elemental Analysis by EDS
- Plates 1 to 7: Thin Section and SEM Photographs

The following samples were analyzed:

- GR-003: MC316 321.14 (Weathered Surface and Matrix)
- GR-005: SP001 288.8 (Weathered Surface and Matrix)

CLIENT: University of Saskatchewan

GR PROJECT #: 16019 2010

TABLE C: Elemental Analysis by EDS

		Elemental Composition by Weight %												
GR SAMPLE #	**Sample Description**	**C**	**O**	**Na**	**Mg**	**Al**	**Si**	**P**	**Cl**	**K**	**Ca**	**Ti**	**Mn**	**Fe**
GR-003	MC316 321.14 Weathered Surface	-	48.66	-	-	7.31	19.81	-	-	2.61	0.56	1.33	7.42	12.30
GR-003	MC316 321.14 Weathered Surface	9.41	49.41	-	-	2.53	30.23	-	-	0.67	-	-	-	7.75
GR-003	MC316 321.14 Matrix	-	55.14	-	0.56	15.43	22.27	-	-	6.11	-	-	-	0.50
GR-005	SP001 288.8 Weathered Surface	12.08	55.99	-	-	5.04	10.48	0.48	-	1.10	-	-	13.29	1.54
GR-005	SP001 288.8 Weathered Surface	15.70	58.33	0.08	0.22	3.10	15.55	0.33	0.09	0.59	-	-	4.12	1.88
GR-005	SP001 288.8 Matrix	-	49.50	-	0.33	4.60	43.09	-	-	1.86	-	-	-	0.63

Discussion of EDS Results

Table C shows the results of the elemental analysis. For each sample, EDS readings for two spots on the weathered surface are shown, along with the EDS results for one spot on the internal matrix.

Sample GR-003

Compared to the matrix, the weathered surface is manganese (Mn) and iron (Fe) rich in the first spot shown, and carbon (C) and iron (Fe) rich in the second spot shown. The first spot also contained minor amounts of calcium (Ca) and titanium (Ti). We expect that some of the carbon (C) is organic in origin. Note that calcium (Ca), manganese (Mn) and titanium (Ti) were not detected in the matrix. Plate 3 shows a macro photograph of the SEM stub with the weathered surface shown at N-7 and the matrix shown at E-7 in View A.

Sample GR-005

In both spots analyzed, the weathered surface is carbon (C), manganese (Mn) and iron (Fe) rich when compared to the matrix. The weathered surface also contains trace amounts of sodium (Na), phosphorus (P) and chlorine (Cl). We expect that some of the carbon (C) is organic in origin. Plate 7 shows a macro photograph of the SEM stub with the weathered surface shown at N-5 and the matrix shown at E-9 in View A.

Thin Section Photomicrographs and Descriptions – Plate 1 University of Saskatchewan

Sample No. GR-003: MC316 321.14

A-D Views of poorly sorted quartzarenite or quartzose sublitharenite with pores blocked by detrital illite clay (large purple arrows) and an iron, manganese and titanium rich pore fill (large orange arrows). The dark brown pore fill characteristic of the weathered surface is likely organic rich and thus is not detected by XRD analysis. Cross polarized view D clearly shows monocrystalline quartz grains (solid grey and white) are the principal framework component. Photo A PPL x10; Photo B PPL x100; Photos C+D PPL,XPL x32

Photo A PPL x10; Photo B PPL x100; Photos C+D PPL,XPL x32

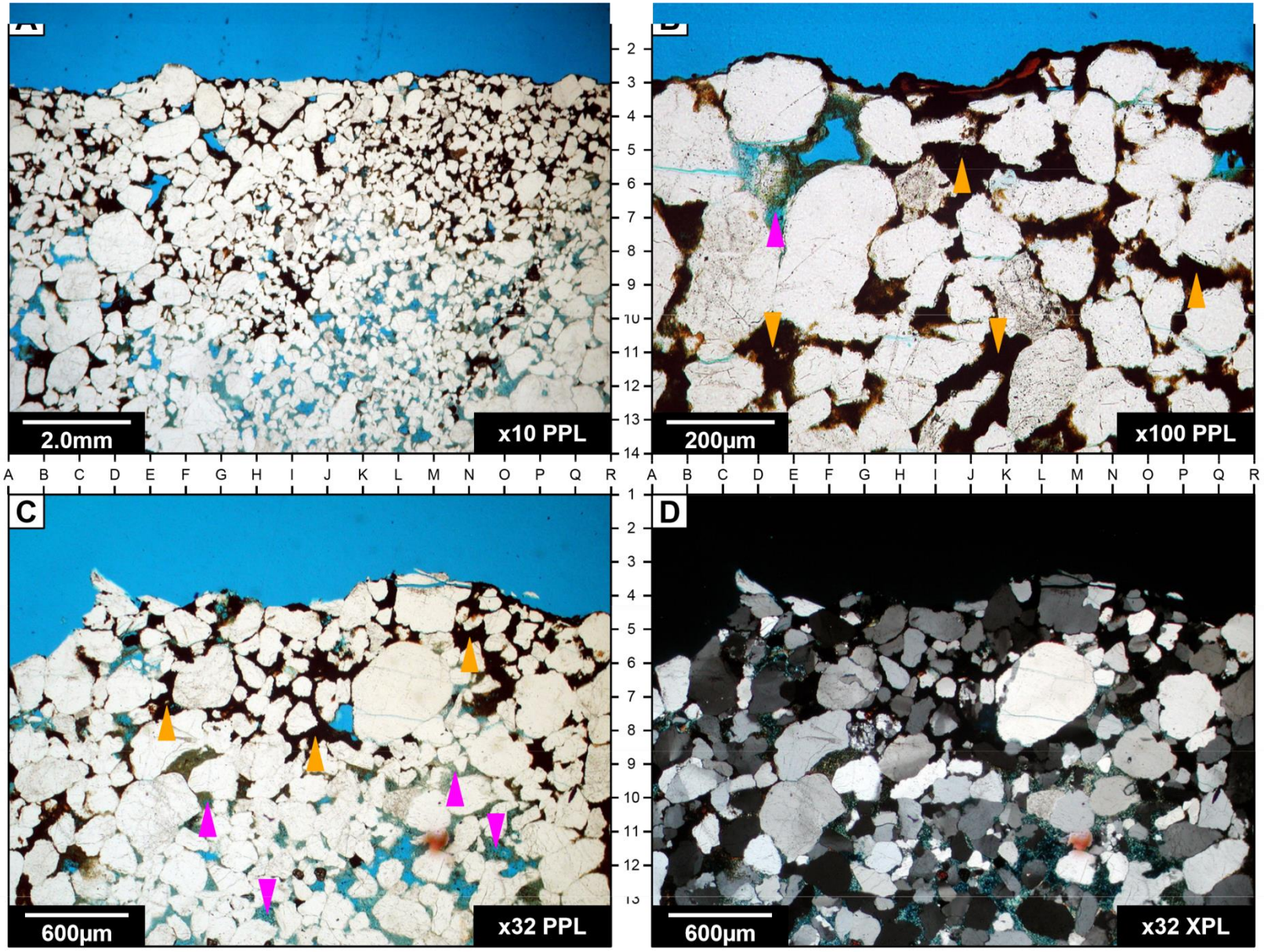

Plate 01

Thin Section Photomicrographs and Descriptions – Plate 2 University of Saskatchewan

Sample No. GR-003: MC316 321.14

A-D Closer views showing brown organic rich pore fill (large purple arrows) associated with the weathered surface. Elemental analysis indicates the pore fill contains higher iron levels compared to the interior of the sample. In addition manganese, calcium, and titanium were only detected in the brown weathered material. XRD analysis suggests the brown weathered material contains some volume of illite, siderite and pyrite. Pore blocking detrital illite clay (large orange arrows) significantly lowers porosity (blue) and inhibited development of quartz cement (medium black arrows). Note zircon heavy minerals (D-12, View C; J-9, P-3, View D). Pore filling pyrite (medium purple arrows) locally blocks porosity.

Photos A-B PPL x100; Photos C-D PPL x200

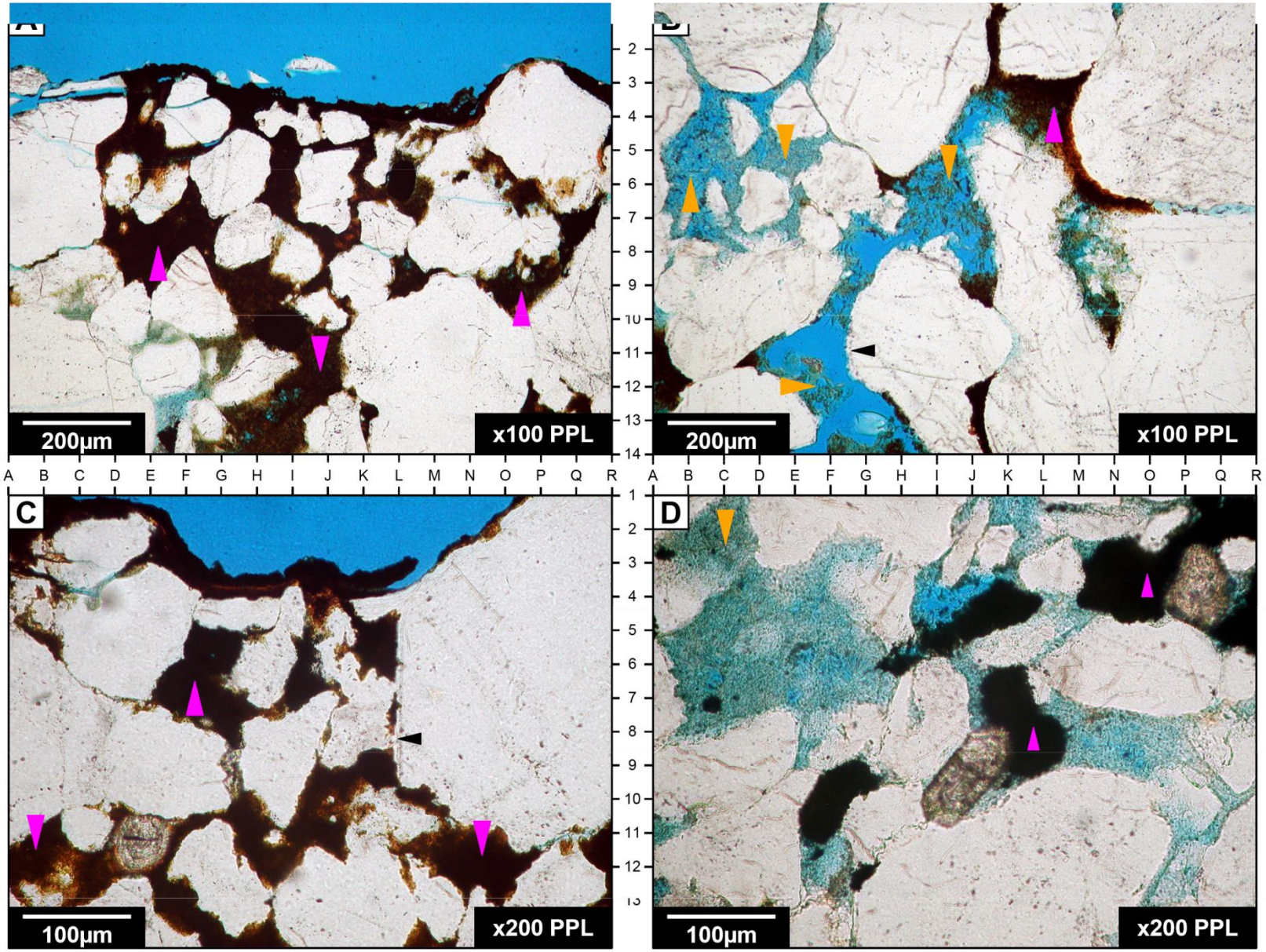
A
200µm
x100 PPL
B
200µm
x100 PPL
C
100µm
x200 PPL
D
100µm
x200 PPL

Plate 02

Scanning Electron Photomicrographs and Descriptions – Plate 3 University of Saskatchewan

Sample No. GR-003: MC316 321.14

A Macro photograph of SEM stub. External brown/black weathered surface is visible on two pieces of the sample at right and center. Two lighter colored pieces from interior of sample are on the left.

B-D Views of weathered surface. Note fibers (Views C and D) which are likely of organic origin.

Photo A x10; Photo B x100; Photo C x400; Photo D x1000

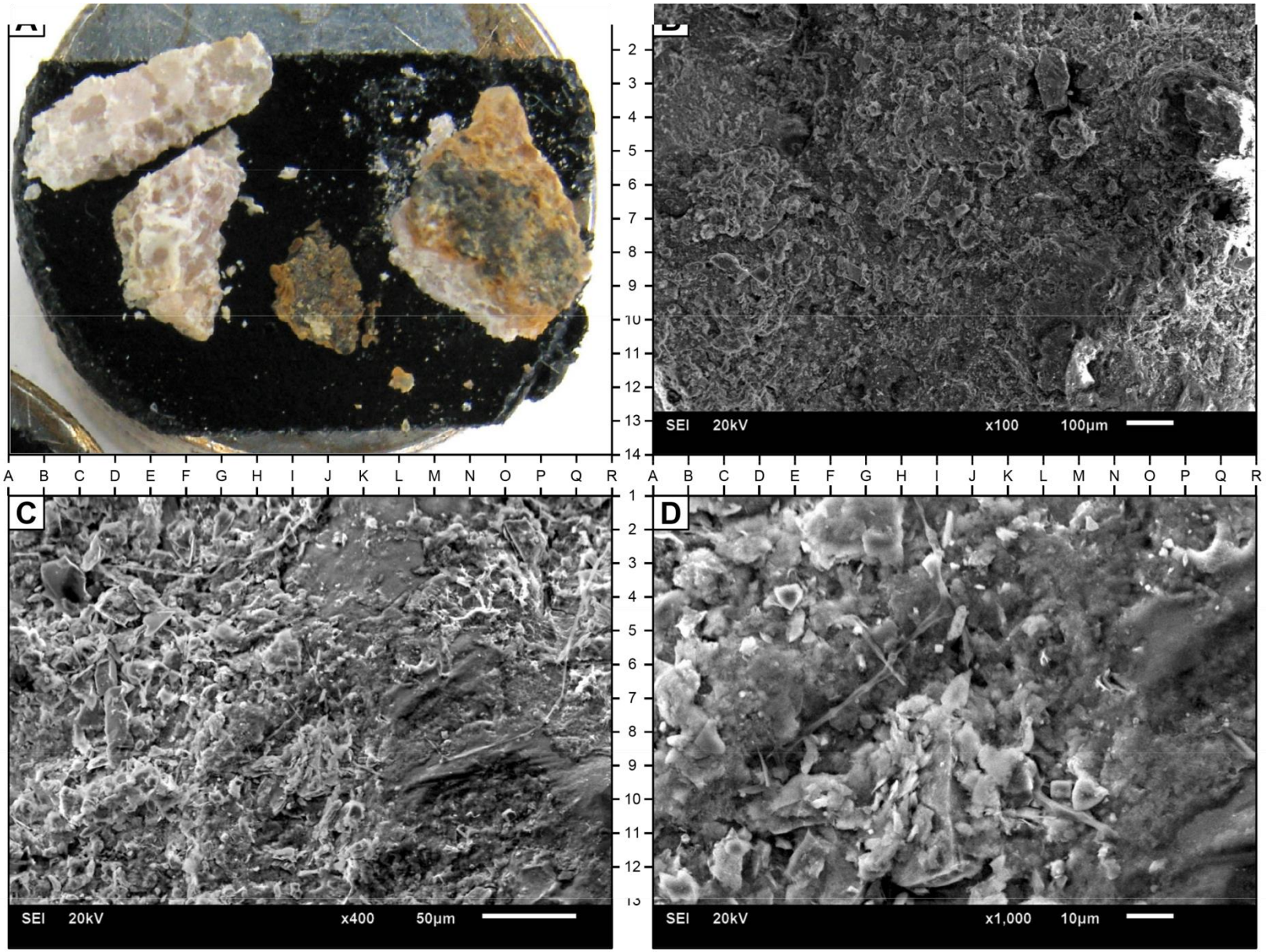
A
B
SEI 20kV x100 100µm
C
SEI 20kV x400 50µm
D
SEI 20kV x1,000 10µm

Plate 03

Thin Section Photom icrographs and Descriptions – Plate 4 University of Saskatchewan

Sample No. GR-005: SP001 288.8

A-D Views of moderately sorted quartzarenite or quartzose sublitharenite with pores blocked by detrital illite clay (large purple arrows) and authigenic kaolinite (large red arrows). Note a thinner manganese rich weathering pore fill (large orange arrows). The dark brown pore fill characteristic of the weathered surface is likely organic rich and thus is not detected by XRD analysis. Cross polarized view D clearly shows monocrystalline quartz grains (solid grey and white) are the principal framework component.

Photo A PPL x10; Photo B PPL x100; Photos C+D PPL,XPL x32

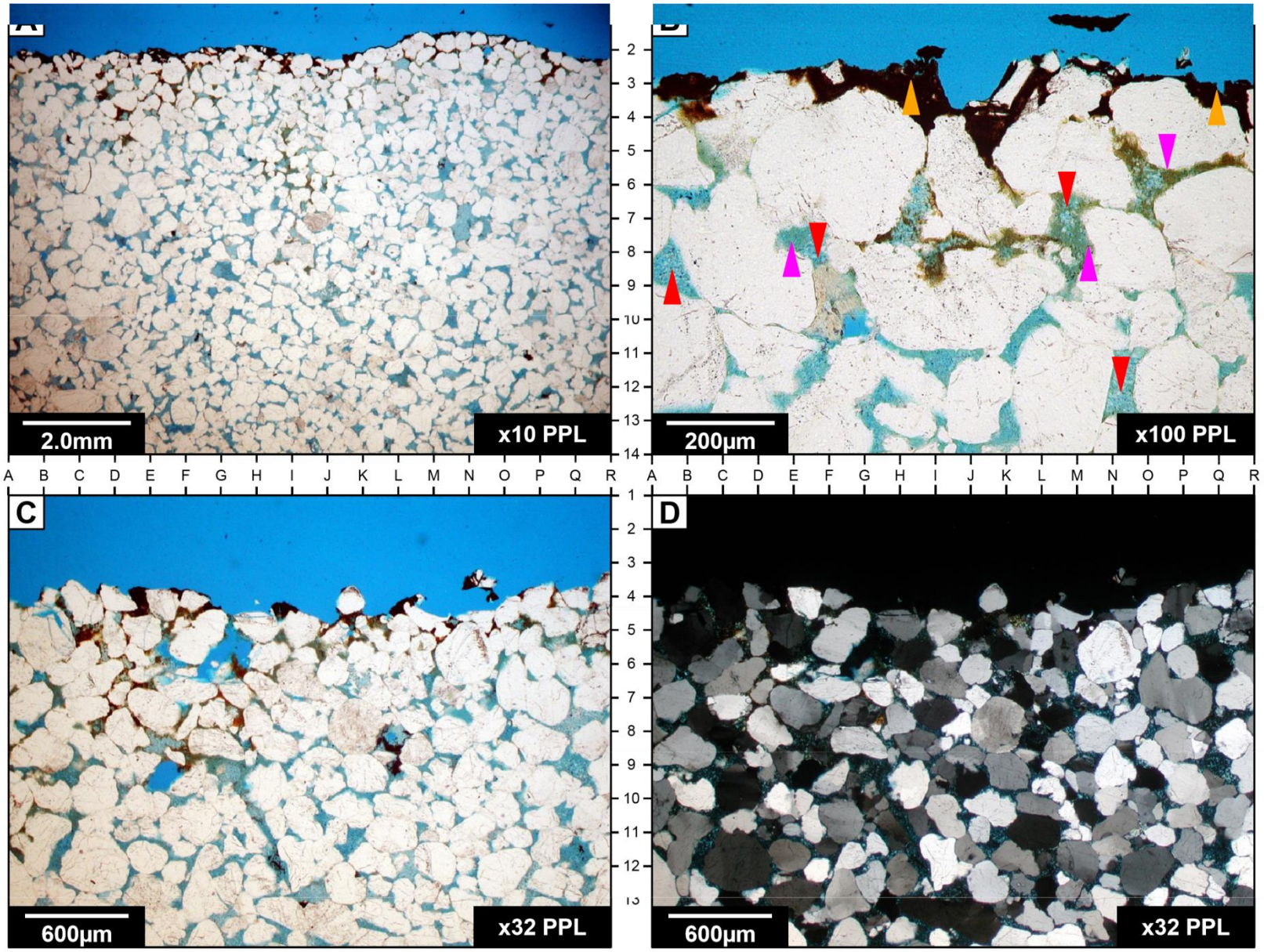
A
2.0mm
x10 PPL
B
200µm
x100 PPL
C
600µm
x32 PPL
D
600µm
x32 PPL
A B C D E F G H I J K L M N O P Q R
1 2 3 4 5 6 7 8 9 10 11 12 13 14

Plate 04

Thin Section Photomicrographs and Descriptions – Plate 5 University of Saskatchewan

Sample No. GR-005: SP001 288.8

A-D Closer views showing brown organic rich pore fill (large orange arrows) associated with the weathered surface. Elemental analysis indicates the pore fill contains high levels of carbon and manganese, and lower levels of sodium, phosphorus and chlorine; none of which were detected in the interior of the sample. Pore blocking detrital illite clay (large purple arrows) and associated well formed authigenic kaolinite booklets (large red arrows) significantly lower porosity (blue) and inhibited development of quartz cement (medium black arrows).

Photos A-B PPL x100; Photos C+D PPL,XPL x100

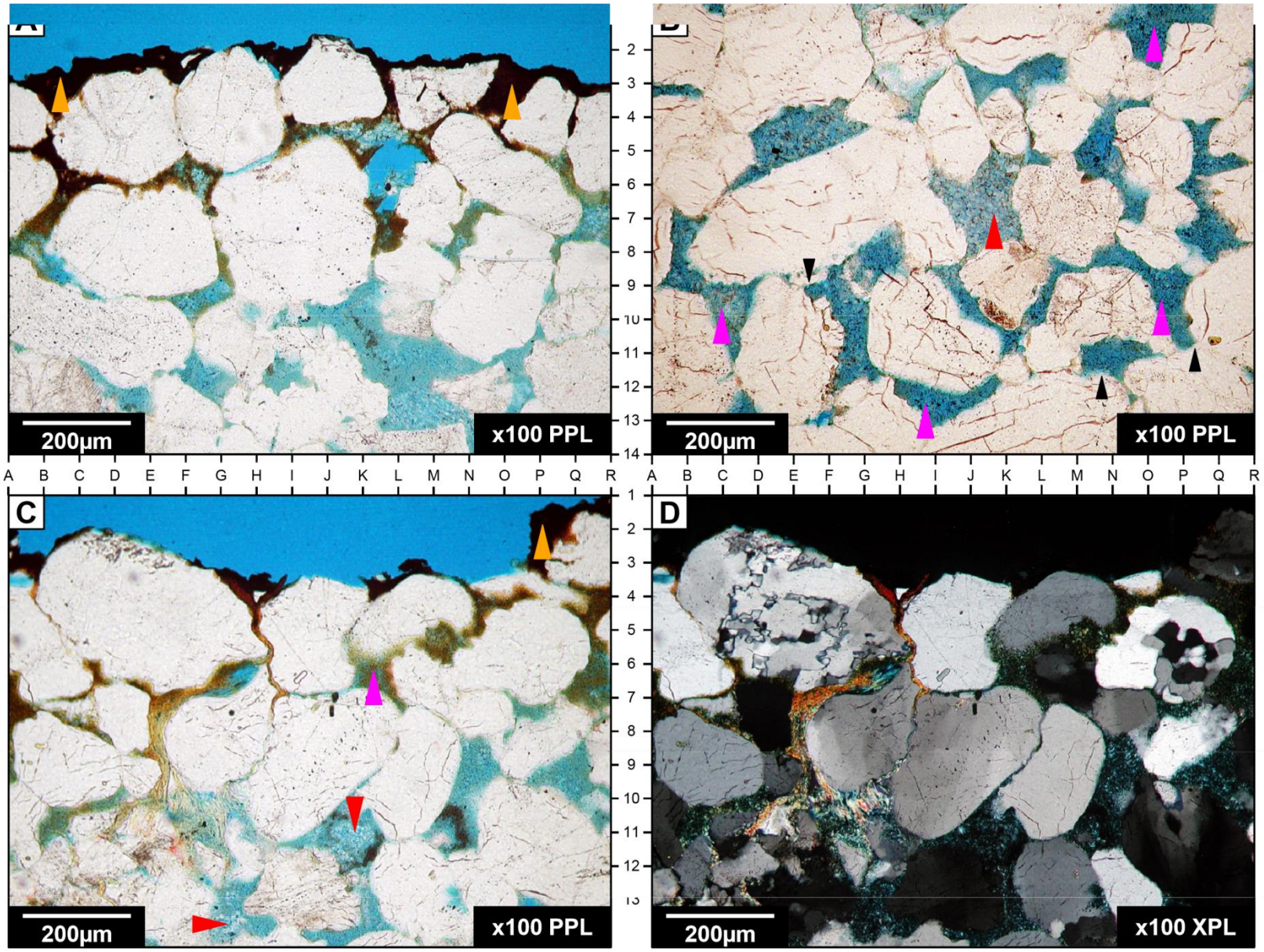
A
200µm
x100 PPL
B
200µm
x100 PPL
C
200µm
x100 PPL
D
200µm
x100 XPL

Plate 05

Thin Section Photomicrographs and Descriptions –

Plate 6 University of Saskatchewan

A-B Closer views of the brown pore fill, illite (large purple arrows) and kaolinite (large red arrows).

Photos A-B PPL x200;

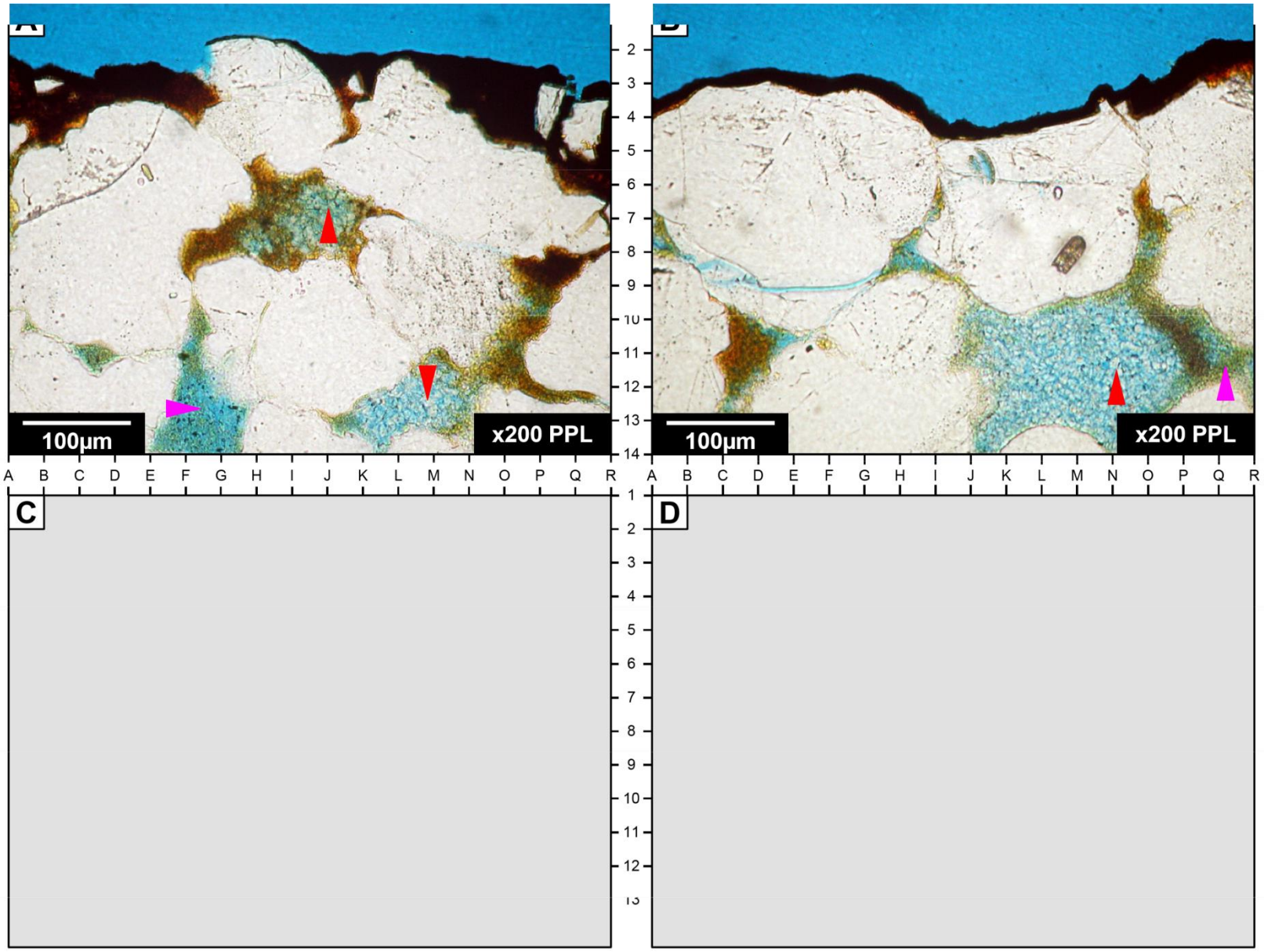
A
100µm
x200 PPL
B
100µm
x200 PPL
C
D
A B C D E F G H I J K L M N O P Q R
1 2 3 4 5 6 7 8 9 10 11 12 13 14

Plate 06

Scanning Electron Photomicrographs and Descriptions - Plate 7
University of Saskatchewan

Sample No. GR-005: SP001 288.8

A Macro photograph of SEM stub. External brown/black weathered surface is visible on piece of the sample at right. Two

pieces from interior of sample are on the left.

B View of weathered surface.

C-D Views of interior of sample. View C mainly shows illite and kaolinite rich pore filling clays (large red arrows) left behind when the sample was broken apart, with monocrystalline quartz (large yellow arrows) visible in a few places. View D mainly shows quartz fragments.

Photo A x10; Photo B x200; Photo C x100; Photo D x1000

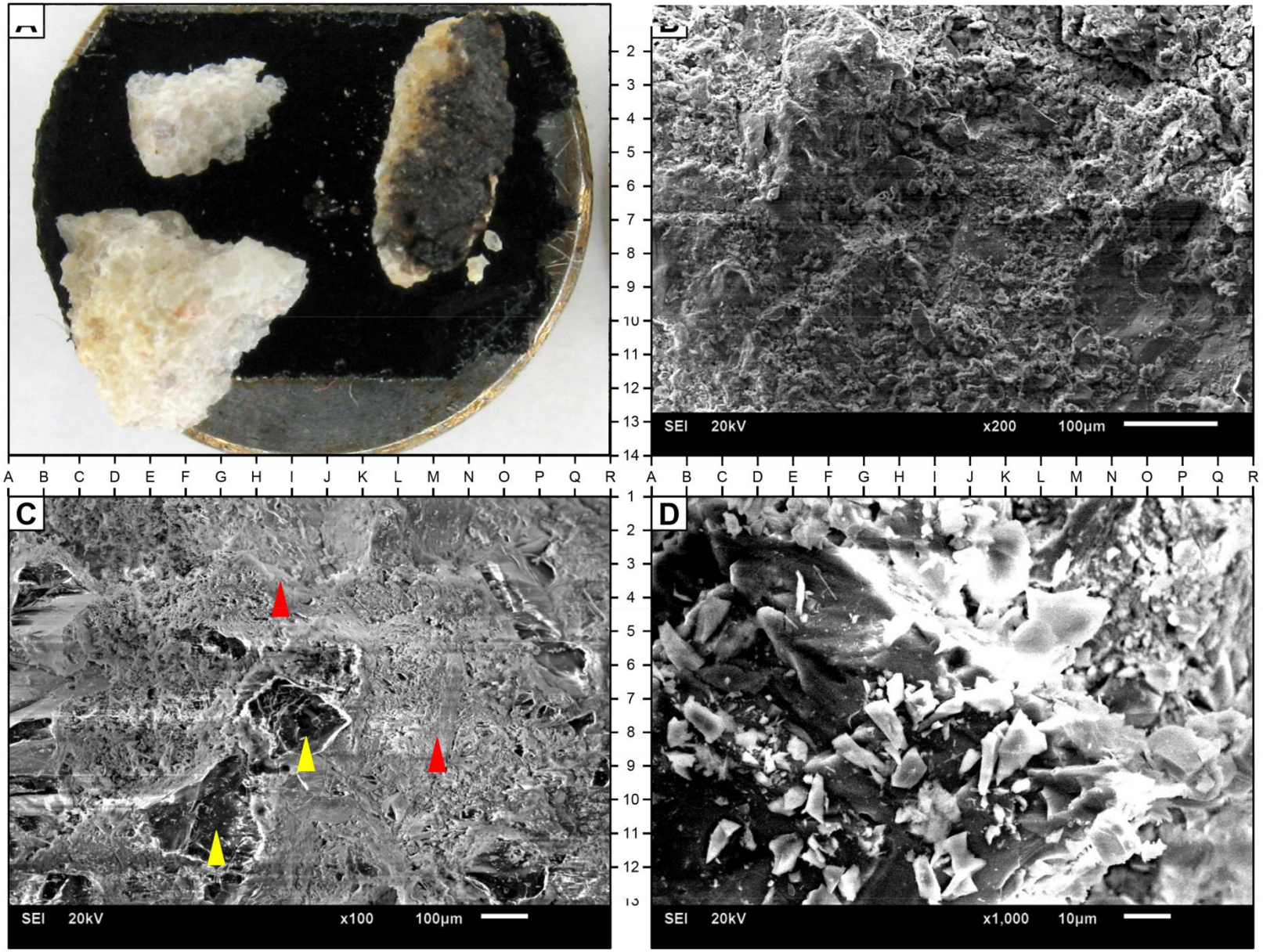
A
B
SEI 20kV x200 100µm
C
SEI 20kV x100 100µm
D
SEI 20kV x1,000 10µm

Plate 07